

DUPLEY UNION LIBRARY
SCHOOL.
ALONG 1000 5002

**VARIATION OF WALL SHEAR STRESS AND
REYNOLDS STRESS OVER A FLAT PLATE
DOWNSTREAM OF A BOUNDARY LAYER
MANIPULATOR**

by

FRANCIS JAMES CAMELIO

B.S., Physics (1971)
M.Ed, Education (1973)
Tufts University

Submitted to the Departments of Ocean Engineering
and Mechanical Engineering in Partial Fulfillment of the
Requirements for the Degrees of

NAVAL ENGINEER

and

MASTER OF SCIENCE IN MECHANICAL ENGINEERING

at the

MASSACHUSETTS INSTITUTE OF TECHNOLOGY

June 1990

© Francis James Camelio, 1990
All rights reserved.

Ain A. Sonin, Chairman
Departmental Graduate Committee
Department of Mechanical Engineering

T247851

1923

C 1923

C.1

VARIATION OF WALL SHEAR STRESS AND REYNOLDS STRESS OVER A FLAT PLATE DOWNSTREAM OF A BOUNDARY LAYER MANIPULATOR

by

FRANCIS JAMES CAMELIO

Submitted to the Departments of Ocean Engineering and Mechanical Engineering
on 11 May 1990 in partial fulfillment of the requirements for the
Degrees of Naval Engineer and Master of Science in Mechanical Engineering

Abstract

An experiment to measure the variation of wall shear stress and Reynolds stress over a flat plate downstream of a honeycomb manipulator was conducted. Two velocity components of the flow were measured with an X-configured hot-wire probe, and wall shear stress was obtained from a surface differential pressure gauge or surface "fence". Unmanipulated boundary layer data was collected at eight different free stream speeds to establish boundary layer characteristics and to calibrate the surface differential pressure gauge by making use of Coles' law of the wall for the mean velocity profile. Manipulated boundary layer data was obtained at three free stream speeds and six manipulator positions. Although manipulator hole size and length remained constant, height was varied to determine the influence of this length scale upon the surface friction coefficient.

Manipulated stream and vertical mean and fluctuating velocity profiles and Reynolds stress profiles were compared to their unmanipulated counterparts to map the influence of the manipulator in the streamwise direction. Immediately downstream of the manipulators the transport of turbulent energy to the wall via the working of Reynolds stresses was sharply reduced. Complete restoration of Reynolds stress profiles to unmanipulated form was not observed out to the farthest downstream measurement position. Local drag reduction up to 40% was verified via comparison of the unmanipulated and manipulated friction coefficients obtained from the wall shear stress measurements. Mid-layer peaking of the Reynolds stress profiles well downstream of the manipulator was accompanied by a near-wall depression of Reynolds stress levels when compared to the unmanipulated case. A decrease in the magnitude of wall shear stress could thereby be attributed to a reduction in turbulent energy transport toward the wall.

Thesis Supervisor: Dr. Patrick Leehey, Professor of Mechanical and Ocean
Engineering

Acknowledgements

I wish to express my thanks to Mr. Yuksel Gur and Mr. Kay Herbert, graduate students in the Department of Mechanical Engineering at the Massachusetts Institute of Technology. Their advice and support were instrumental in defining and developing a sound research plan. Special thanks are also extended to my thesis supervisor, Professor Patrick Leehey, whose patience allowed me to explore in detail varied aspects of hot-wire anemometry which proved quite rewarding. I developed an intense appreciation of the subtleties of the subject and the difficulties one can encounter with elementary experimental arrangements.

I also owe my gratitude to Mr. Stan Fisher (Code 1942) and Dr. Ted Farabee of the David Taylor Research Center, Carderock, Maryland, who financially and professionally supported me and others in projects directly related to the experimentation conducted.

Finally, I am most indebted to the U. S. Navy for funding my education at the Massachusetts Institute of Technology and providing me the opportunity to fulfill potentials previously untapped.

Table of Contents

Abstract	2
Acknowledgements	3
Table of Contents	4
Table of Figures	5
Table of Tables	8
Nomenclature	9
1 Introduction	11
1.1 Background	11
1.2 Objectives	15
2 Equipment Description	16
2.1 Facility and Equipment	16
2.1.1 Wind Tunnel	16
2.1.2 Traverse	18
2.2 Velocity Probes	19
2.3 Pressure Probes	20
2.3.1 Pitot	20
2.3.2 Surface Differential Pressure Gauge	21
2.4 Manipulators	23
2.5 Data Acquisition System	26
3 Experiment Description	28
3.1 X-Probe Calibration	28
3.2 Boundary Layer Measurements	36
3.2.1 Unmanipulated Velocity Profiles	44
3.2.2 Manipulated Velocity Profiles	48
3.3 Stress Measurements	64
3.3.1 Wall Shear Stress	64
3.3.2 Reynolds Stress	66
4 Discussion of Results	71
4.1 Manipulator Influence on Velocity Profiles	71
4.2 Manipulator Influence on Measured Stresses	73
5 Conclusions and Recommendations	85
5.1 Conclusions	85
5.2 Recommendations	86
References	88
Appendix A Supplementary Graphs	91
A.1 Fifteen Meters Per Second Data	91
A.2 Twenty-Three Meters Per Second Data	106
Appendix B Tabular Data	122
Appendix C Computer Programs	123

111
112
113

Table of Figures

Figure 2.1: Wind Tunnel Facility	17
Figure 2.2: Traverse System Schematic	19
Figure 2.3: Surface Differential Pressure Gauge	22
Figure 2.4: Honeycomb Manipulator Schematic	23
Figure 3.1: X-Probe Velocity Geometry	29
Figure 3.2: Stream Velocity Calibration Surface	33
Figure 3.3: Normal Velocity Calibration Surface	34
Figure 3.4: Wind Tunnel Calibration Configuration	35
Figure 3.5: Law of the Wall Fit (Unmanipulated, $U_\infty=19$ m/sec)	38
Figure 3.6(a): Law of the Wall Fit ($x_{BLM}=4$ cm, $U_\infty=19$ m/sec)	41
Figure 3.6(b): Law of the Wall Fit ($x_{BLM}=12$ cm, $U_\infty=19$ m/sec)	41
Figure 3.6 (c): Law of the Wall Fit ($x_{BLM}=25$ cm, $U_\infty=19$ m/sec)	42
Figure 3.6(d): Law of the Wall Fit ($x_{BLM}=65$ cm, $U_\infty=19$ m/sec)	42
Figure 3.6(e): Law of the Wall Fit ($x_{BLM}=100$ cm, $U_\infty=19$ m/sec)	43
Figure 3.6(f): Law of the Wall Fit ($x_{BLM}=150$ cm, $U_\infty=19$ m/sec)	43
Figure 3.7(a): Unmanipulated Mean Velocity Profile ($U_\infty=19$ m/sec)	45
Figure 3.7(b): Unmanipulated $\sqrt{u'^2}$ Profile ($U_\infty=19$ m/sec)	46
Figure 3.7(c): Unmanipulated $\sqrt{v'^2}$ Profile ($U_\infty=19$ m/sec)	48
Figure 3.8(a): Mean Velocity Comparison ($x_{BLM}=4$ cm, $U_\infty=19$ m/sec)	50
Figure 3.8(b): Mean Velocity Comparison ($x_{BLM}=12$ cm, $U_\infty=19$ m/sec)	50
Figure 3.8(c): Mean Velocity Comparison ($x_{BLM}=25$ cm, $U_\infty=19$ m/sec)	51
Figure 3.8(d): Mean Velocity Comparison ($x_{BLM}=65$ cm, $U_\infty=19$ m/sec)	51
Figure 3.8(e): Mean Velocity Comparison ($x_{BLM}=100$ cm, $U_\infty=19$ m/sec)	52
Figure 3.8(f): Mean Velocity Comparison ($x_{BLM}=150$ cm, $U_\infty=19$ m/sec)	52
Figure 3.9(a): Vertical Velocity Profile ($x_{BLM}=4$ cm, $U_\infty=19$ m/sec)	54
Figure 3.9(b): Vertical Velocity Profile ($x_{BLM}=12$ cm, $U_\infty=19$ m/sec)	54
Figure 3.9(c): Vertical Velocity Profile ($x_{BLM}=25$ cm, $U_\infty=19$ m/sec)	55
Figure 3.9(d): Vertical Velocity Profile ($x_{BLM}=65$ cm, $U_\infty=19$ m/sec)	55
Figure 3.9(e): Vertical Velocity Profile ($x_{BLM}=100$ cm, $U_\infty=19$ m/sec)	56
Figure 3.10(a): $\sqrt{u'^2}$ Profile ($x_{BLM}=4$ cm, $U_\infty=19$ m/sec)	57
Figure 3.10(b): $\sqrt{u'^2}$ Profile ($x_{BLM}=12$ cm, $U_\infty=19$ m/sec)	57
Figure 3.10(c): $\sqrt{u'^2}$ Profile ($x_{BLM}=25$ cm, $U_\infty=19$ m/sec)	58
Figure 3.10(d): $\sqrt{u'^2}$ Profile ($x_{BLM}=65$ cm, $U_\infty=19$ m/sec)	58
Figure 3.10(e): $\sqrt{u'^2}$ Profile ($x_{BLM}=100$ cm, $U_\infty=19$ m/sec)	59
Figure 3.10(f): $\sqrt{u'^2}$ Profile ($x_{BLM}=150$ cm, $U_\infty=19$ m/sec)	59
Figure 3.11(a): $\sqrt{v'^2}$ Profile ($x_{BLM}=4$ cm, $U_\infty=19$ m/sec)	61
Figure 3.11(b): $\sqrt{v'^2}$ Profile ($x_{BLM}=12$ cm, $U_\infty=19$ m/sec)	61
Figure 3.11(c): $\sqrt{v'^2}$ Profile ($x_{BLM}=25$ cm, $U_\infty=19$ m/sec)	62
Figure 3.11(d): $\sqrt{v'^2}$ Profile ($x_{BLM}=65$ cm, $U_\infty=19$ m/sec)	62
Figure 3.11(e): $\sqrt{v'^2}$ Profile ($x_{BLM}=100$ cm, $U_\infty=19$ m/sec)	63
Figure 3.11(f): $\sqrt{v'^2}$ Profile ($x_{BLM}=150$ cm, $U_\infty=19$ m/sec)	63

Figure 3.12(a): Surface Fence Calibration (ΔP vs τ_w)	65
Figure 3.12(b): Surface Fence Calibration ($\ln(\Delta P/\tau_w)$ vs $\ln(h^+)$)	65
Figure 3.13(a): Reynolds Stress Profile ($x_{BLM}=4$ cm, $U_\infty=19$ m/sec)	67
Figure 3.13(b): Reynolds Stress Profile ($x_{BLM}=12$ cm, $U_\infty=19$ m/sec)	68
Figure 3.13(c): Reynolds Stress Profile ($x_{BLM}=25$ cm, $U_\infty=19$ m/sec)	68
Figure 3.13(d): Reynolds Stress Profile ($x_{BLM}=65$ cm, $U_\infty=19$ m/sec)	69
Figure 3.13(e): Reynolds Stress Profile ($x_{BLM}=100$ cm, $U_\infty=19$ m/sec)	69
Figure 3.13(f): Reynolds Stress Profile ($x_{BLM}=150$ cm, $U_\infty=19$ m/sec)	70
Figure 4.1: Friction Coefficient Ratio	74
Figure 4.2(a): Stress Energy Transport ($x_{BLM}=4$ cm, $U_\infty=19$ m/sec)	81
Figure 4.2(b): Stress Energy Transport ($x_{BLM}=12$ cm, $U_\infty=19$ m/sec)	82
Figure 4.2(c): Stress Energy Transport ($x_{BLM}=25$ cm, $U_\infty=19$ m/sec)	82
Figure 4.2(d): Stress Energy Transport ($x_{BLM}=65$ cm, $U_\infty=19$ m/sec)	83
Figure 4.2(e): Stress Energy Transport ($x_{BLM}=100$ cm, $U_\infty=19$ m/sec)	83
Figure 4.2(f): Stress Energy Transport ($x_{BLM}=150$ cm, $U_\infty=19$ m/sec)	84
Figure A.1.1: Unmanipulated Mean Velocity Profile ($U_\infty=15$ m/sec)	91
Figure A.1.2: Unmanipulated $\sqrt{u'^2}$ Profile ($U_\infty=15$ m/sec)	92
Figure A.1.3: Unmanipulated $\sqrt{v'^2}$ Profile ($U_\infty=15$ m/sec)	92
Figure A.1.4: Mean Velocity Comparison ($x_{BLM}=4$ cm, $U_\infty=15$ m/sec)	93
Figure A.1.5: Mean Velocity Comparison ($x_{BLM}=12$ cm, $U_\infty=15$ m/sec)	93
Figure A.1.6: Mean Velocity Comparison ($x_{BLM}=25$ cm, $U_\infty=15$ m/sec)	94
Figure A.1.7: Mean Velocity Comparison ($x_{BLM}=65$ cm, $U_\infty=15$ m/sec)	94
Figure A.1.8: Mean Velocity Comparison ($x_{BLM}=100$ cm, $U_\infty=15$ m/sec)	95
Figure A.1.9: Mean Velocity Comparison ($x_{BLM}=150$ cm, $U_\infty=15$ m/sec)	95
Figure A.1.10: Mean Vertical Velocity ($x_{BLM}=4$ cm, $U_\infty=15$ m/sec)	96
Figure A.1.11: Mean Vertical Velocity ($x_{BLM}=12$ cm, $U_\infty=15$ m/sec)	96
Figure A.1.12: Mean Vertical Velocity ($x_{BLM}=25$ cm, $U_\infty=15$ m/sec)	97
Figure A.1.13: $\sqrt{u'^2}$ Profile ($x_{BLM}=4$ cm, $U_\infty=15$ m/sec)	97
Figure A.1.14: $\sqrt{u'^2}$ Profile ($x_{BLM}=12$ cm, $U_\infty=15$ m/sec)	98
Figure A.1.15: $\sqrt{u'^2}$ Profile ($x_{BLM}=25$ cm, $U_\infty=15$ m/sec)	98
Figure A.1.16: $\sqrt{u'^2}$ Profile ($x_{BLM}=65$ cm, $U_\infty=15$ m/sec)	99
Figure A.1.17: $\sqrt{u'^2}$ Profile ($x_{BLM}=100$ cm, $U_\infty=15$ m/sec)	99
Figure A.1.18: $\sqrt{u'^2}$ Profile ($x_{BLM}=150$ cm, $U_\infty=15$ m/sec)	100
Figure A.1.19: $\sqrt{v'^2}$ Profile ($x_{BLM}=4$ cm, $U_\infty=15$ m/sec)	100
Figure A.1.20: $\sqrt{v'^2}$ Profile ($x_{BLM}=12$ cm, $U_\infty=15$ m/sec)	101
Figure A.1.21: $\sqrt{v'^2}$ Profile ($x_{BLM}=25$ cm, $U_\infty=15$ m/sec)	101
Figure A.1.22: $\sqrt{v'^2}$ Profile ($x_{BLM}=65$ cm, $U_\infty=15$ m/sec)	102
Figure A.1.23: $\sqrt{v'^2}$ Profile ($x_{BLM}=100$ cm, $U_\infty=15$ m/sec)	102
Figure A.1.24: $\sqrt{v'^2}$ Profile ($x_{BLM}=150$ cm, $U_\infty=15$ m/sec)	103
Figure A.1.25: Reynolds Stress Profile ($x_{BLM}=4$ cm, $U_\infty=15$ m/sec)	103
Figure A.1.26: Reynolds Stress Profile ($x_{BLM}=12$ cm, $U_\infty=15$ m/sec)	104
Figure A.1.27: Reynolds Stress Profile ($x_{BLM}=25$ cm, $U_\infty=15$ m/sec)	104
Figure A.1.28: Reynolds Stress Profile ($x_{BLM}=65$ cm, $U_\infty=15$ m/sec)	105
Figure A.1.29: Reynolds Stress Profile ($x_{BLM}=100$ cm, $U_\infty=15$ m/sec)	105

Figure A.1.30: Reynolds Stress Profile ($x_{BLM}=150$ cm, $U_{\infty}=15$ m/sec).....	106
Figure A.2.1: Unmanipulated Mean Velocity Profile ($U_{\infty}=23$ m/sec)	106
Figure A.2.2: Unmanipulated $\sqrt{u'^2}$ Profile ($U_{\infty}=23$ m/sec).....	107
Figure A.2.3: Unmanipulated $\sqrt{v'^2}$ Profile ($U_{\infty}=23$ m/sec)	107
Figure A.2.4: Mean Velocity Comparison ($x_{BLM}=4$ cm, $U_{\infty}=23$ m/sec)	108
Figure A.2.5: Mean Velocity Comparison ($x_{BLM}=12$ cm, $U_{\infty}=23$ m/sec)	108
Figure A.2.6: Mean Velocity Comparison ($x_{BLM}=25$ cm, $U_{\infty}=23$ m/sec)	109
Figure A.2.7: Mean Velocity Comparison ($x_{BLM}=65$ cm, $U_{\infty}=23$ m/sec)	109
Figure A.2.8: Mean Velocity Comparison ($x_{BLM}=100$ cm, $U_{\infty}=23$ m/sec)	110
Figure A.2.9: Mean Velocity Comparison ($x_{BLM}=150$ cm, $U_{\infty}=23$ m/sec)	110
Figure A.2.10: Mean Vertical Velocity Profile ($x_{BLM}=4$ cm, $U_{\infty}=23$ m/sec).....	111
Figure A.2.11: Mean Vertical Velocity Profile ($x_{BLM}=12$ cm, $U_{\infty}=23$ m/sec).....	111
Figure A.2.12: Mean Vertical Velocity Profile ($x_{BLM}=25$ cm, $U_{\infty}=23$ m/sec).....	112
Figure A.2.13: $\sqrt{u'^2}$ Profile ($x_{BLM}=4$ cm, $U_{\infty}=23$ m/sec)	112
Figure A.1.16: $\sqrt{u'^2}$ Profile ($x_{BLM}=12$ cm, $U_{\infty}=23$ m/sec)	113
Figure A.2.15: $\sqrt{u'^2}$ Profile ($x_{BLM}=25$ cm, $U_{\infty}=23$ m/sec)	113
Figure A.2.16: $\sqrt{u'^2}$ Profile ($x_{BLM}=65$ cm, $U_{\infty}=23$ m/sec)	114
Figure A.2.17: $\sqrt{u'^2}$ Profile ($x_{BLM}=100$ cm, $U_{\infty}=23$ m/sec)	114
Figure A.2.18: $\sqrt{u'^2}$ Profile ($x_{BLM}=150$ cm, $U_{\infty}=23$ m/sec)	115
Figure A.2.19: $\sqrt{v'^2}$ Profile ($x_{BLM}=150$ cm, $U_{\infty}=23$ m/sec)	115
Figure A.2.20: $\sqrt{v'^2}$ Profile ($x_{BLM}=12$ cm, $U_{\infty}=23$ m/sec)	116
Figure A.2.21: $\sqrt{v'^2}$ Profile ($x_{BLM}=25$ cm, $U_{\infty}=23$ m/sec)	116
Figure A.2.22: $\sqrt{v'^2}$ Profile ($x_{BLM}=65$ cm, $U_{\infty}=23$ m/sec)	117
Figure A.2.23: $\sqrt{v'^2}$ Profile ($x_{BLM}=100$ cm, $U_{\infty}=23$ m/sec)	117
Figure A.2.24: $\sqrt{v'^2}$ Profile ($x_{BLM}=150$ cm, $U_{\infty}=23$ m/sec)	118
Figure A.2.25: Reynolds Stress Profile ($x_{BLM}=4$ cm, $U_{\infty}=23$ m/sec)	118
Figure A.2.26: Reynolds Stress Profile ($x_{BLM}=12$ cm, $U_{\infty}=23$ m/sec).....	119
Figure A.2.27: Reynolds Stress Profile ($x_{BLM}=25$ cm, $U_{\infty}=23$ m/sec).....	119
Figure A.2.28: Reynolds Stress Profile ($x_{BLM}=65$ cm, $U_{\infty}=23$ m/sec).....	120
Figure A.2.29: Reynolds Stress Profile ($x_{BLM}=100$ cm, $U_{\infty}=23$ m/sec).....	120
Figure A.2.30: Reynolds Stress Profile ($x_{BLM}=150$ cm, $U_{\infty}=23$ m/sec).....	121

Table of Tables

Table 2.1: X-Probe Characteristics	20
Table 2.2: Manipulator Positions and Heights	25
Table 3.1: Unmanipulated Boundary Layer Parameters	39
Table 3.2: Manipulated Boundary Layer Parameters ($U_{\infty}=15$ m/sec)	39
Table 3.3: Manipulated Boundary Layer Parameters ($U_{\infty}=19$ m/sec)	40
Table 3.4: Manipulated Boundary Layer Parameters ($U_{\infty}=23$ m/sec)	40

Nomenclature

a, b	constant coefficients in polynomial or other equations
$C_{f,m}, C_{f,um}$	manipulated and unmanipulated wall friction coefficients where $C_f = 2u_\tau^2/U_\infty^2$
D	sensor diameter
E_0	instantaneous voltage across sensor
h^+	fence height in viscous units = $h u_\tau / \nu$
h_{BLM}	height of the Boundary Layer Manipulator
L	sensor length
n	exponent
\bar{p}	mean pressure at a given position
p'	fluctuating pressure at a given position
$\sqrt{\overline{p_w'^2}}$	rms wall pressure fluctuation
$\overline{q^2}$	turbulent kinetic energy = $\overline{u'^2} + \overline{v'^2} + \overline{w'^2}$
$\overline{u'v'}$	time average of the product of u' and v'
u	instantaneous velocity in stream direction at height y above wall ($u = \bar{u} + u'$)
\bar{u}	mean velocity in stream direction at height y above wall
u'	instantaneous fluctuating velocity in the stream direction
$\sqrt{\overline{u'^2}}$ or u'_{rms}	rms value of fluctuating velocity in the stream direction
u^+	non-dimensional stream velocity = u/u_τ
u_τ	friction velocity = $(\tau_w/\rho)^{\frac{1}{2}}$
U_∞ or U_o	velocity in stream direction outside the boundary layer

v	instantaneous velocity normal to the wall at height y above wall ($v = \bar{v} + v'$)
\bar{v}	mean velocity normal to wall and stream velocity
v'	instantaneous fluctuating velocity in the normal direction
$\sqrt{v'^2}$ or v'_{rms}	rms value of fluctuating velocity normal to the wall surface
\bar{w}	mean velocity parallel to the plate and normal to the stream flow
w'	instantaneous fluctuating velocity normal to the plane formed by u' and v'
y^+	non-dimensional height above wall $= \frac{y u_\tau}{\nu}$
x_{BLM}	upstream distance of the Boundary Layer Manipulator from the measurement position
δ	boundary layer thickness, experimentally defined where $\bar{u} = .995 U_\infty$
δ^*	displacement thickness, for incompressible flow $\delta^* = \int_{y=0}^{\infty} \left(1 - \frac{\bar{u}}{U_\infty} \right) dy$
δ^*_{und}	displacement thickness for the undisturbed flow for a given free stream speed at a position downstream of the virtual origin where the Boundary Layer Manipulator is placed
ΔP	differential pressure across the surface fence
ϵ_m, ϵ_t	mean and turbulent viscous dissipation
μ	absolute viscosity of fluid
ν	kinematic viscosity of fluid
ρ	fluid density
τ	total shear stress $= \mu(\partial u / \partial y) - \rho \overline{u'v'}$
$\hat{\tau}$	$\tau/\rho = \nu(\partial \bar{u} / \partial y) - \overline{u'v'}$
τ_w	wall shear stress

1 Introduction

1.1 Background

Both the reduction of skin friction drag and the reduction of wall pressure fluctuations via alteration of the turbulent flow structures within the boundary layer surrounding a body or object are ongoing efforts in the fields of fluid dynamics and acoustics. By reducing drag, improved speed performance and fuel economy are achieved for aero- and hydro-vehicles. By minimizing wall pressure fluctuations, improved passive SONAR performance is achievable. A major focus of the research has been the development and analysis of devices to break up the large eddy structures in the turbulent regime which are believed to be the primary sources of increased drag and wall excitation. These devices are referred to as LEBU's (Large Eddy Break-up Devices) or, more recently, as Boundary Layer Manipulators (herein BLM's). The latter term is preferred since it does not presuppose the physical mechanism involved.

To date inconsistent results have been obtained concerning the effectiveness of BLM's. Compounding the problem are the various geometries of the BLM devices used. Beeler [1] found a 12.5% reduction in $\sqrt{p_w'^2}$ using two rigid ribbon manipulators (thin parallel strips) mounted in tandem in the boundary layer, but measurement was restricted to only one position downstream of the BLM. In a more detailed study Nguyen et al [2] used single and triple ribbons to measure skin friction reductions at various locations downstream of these BLM's with a peak reduction of 35%. A departure from and then re-establishment of Coles' logarithmic law of the wall [3] as measurements were extended downstream of the manipulators was also documented. Hefner et al [4] used a sawtooth serrated device to obtain a peak skin friction reduction of 24%, and also compared the boundary layer profiles for $\frac{\bar{u}}{U_\infty}$ and $\frac{\sqrt{u'^2}}{U_\infty}$ for the manipulated and unmanipulated cases at different stations downstream of the BLM. Honeycomb BLM's

were utilized by Moller and Leehey [5] to make point measurements of mean wall shear and wall pressure spectra at various stations downstream of the manipulator. Roth and Leehey [6] varied honeycomb height and size to describe their influence on the boundary layer profiles for \bar{u} and $\sqrt{u'^2}$ and to measure τ_w in the streamwise direction.

All of the preceding investigations were conducted in wind tunnel facilities with measurements conducted over a flat plate or wall. Flow speeds ranged from approximately 2 - 35 meters per second. As the data accumulates, researchers will focus their attentions on determining what types and sizes of BLM's are appropriate to accomplish a particular objective, whether for overall drag reduction on a vehicle or local wall pressure fluctuation reduction for SONAR applications. One critical parameter has received little attention, the Reynolds stress ($-\rho\overline{u'v'}$ for incompressible flow). By measuring Reynolds stress profiles at various streamwise locations downstream of a BLM and comparing these to the unmanipulated flow, a better understanding of the mechanisms involved in altering the turbulent flow structures should emerge, particularly in the transport of turbulent energy within the boundary layer. This appears the next logical step in understanding the factors determining manipulated turbulent flow structures. Westphal has reported alterations of the Reynolds stress profile at various stations downstream of single and tandem strip or plate manipulators [7]. Westphal found large reductions in Reynolds stresses immediately downstream of these manipulators, followed by a substantial increase in these stresses in the mid-layer farther downstream. Westphal's findings provide a basis of comparison for the measurements undertaken and are discussed in more detail later.

Mathematical representations of energy transport within a turbulent boundary layer have been forwarded in order to explain measured characteristics of the boundary layer. In particular, the influence of shearing stresses in the sub-layers has been examined. Townsend has proposed energy conservation relationships for boundary layers in channel

flow and over flat plates which include the energy flow resulting from the working of Reynolds and viscous stresses within the inner and outer layers [8]. In Townsend's representation, the gradient normal to the wall surface, of the product of the local mean flow and the total shear stress in the outer layer provides an energy flow into the near-wall or viscous sub-layer. Equation (1.1) provides symbolic representation of this term based on a coordinate system where x is in the stream direction, y is normal to the wall surface ($y = 0$), and z is parallel to the plate surface (cross channel).

$$\left\{ \begin{array}{l} \text{rate of energy transfer} \\ \text{per unit mass} \end{array} \right\} = -\frac{\partial(\bar{\tau}u)}{\partial y} \quad (1.1)$$

In wind tunnel experiments, Klebanoff found that approximately 85% of the total energy dissipation occurs in the near-wall region within a y^+ not exceeding 30 [9]. The dissipation has both viscous and turbulent components. Klebanoff concluded, albeit with an incomplete set of measurements, that turbulent energy production and dissipation peaked in the near-wall layer and that pressure forces effected an inward flow of energy toward the wall [9]. In Townsend's model these pressure forces arise due to the action of the shearing stresses ($\hat{\tau}$) represented in Equation (1.1), which are dominated by the Reynolds stress outside the viscous sub-layer.

The presence of a manipulator in the turbulent boundary layer will influence energy transport mechanisms, depending on the size and geometry of the BLM. By measuring the Reynolds stress profile in the manipulated layer, it should be possible to determine what type of influence a given manipulator has in altering the energy transport to the wall. If the manipulator reduces the turbulent energy received at the wall, then the root-mean-square wall pressure or wall shear stress should also decrease. Such an effect will certainly contribute to improvement in SONAR self-noise for any transducers mounted on the wall immediately downstream of the manipulator(s). Whether an overall drag reduction is realized depends primarily on the magnitude of the self-drag of the

manipulator. The combined optimization of both self-drag and self-noise reduction may not be achievable. An obvious long-term goal in the study of manipulator influence on altering energy transport processes in the boundary layer is to determine which type of manipulator best accomplishes this end. Since no Reynolds stress profile measurements downstream of a honeycomb manipulator have been documented, this type was selected in the experiments undertaken. Measurement of the x and y velocity components at specific and numerous locations within a turbulent boundary layer and measurement of wall shear stress with a surface differential pressure gauge or similar device will provide the necessary data to establish the influence of the manipulator on energy transport to the wall.

Hot-wire anemometry is the most frequently used measurement method of turbulent boundary layer velocity profiles. Small single (or U-configuration) and X-configuration sensors are common in wind tunnel applications with unidirectional mean flow. The X-probe is able to resolve two velocity components of the flow at the position of the sensors. Numerous calibration techniques have been devised for both U- and X-probes for use over a narrow temperature band and over the range of velocities anticipated. To ensure the highest accuracy, many alternative calibration schemes were investigated. X-probe calibration schemes can be grouped into two major categories, calibration based upon heat transfer principles and flow geometry and calibration based upon geometric considerations only. Both approaches rely upon voltage data from the probe sensors to reflect the instantaneous local flow conditions. Boundary layer velocity data were obtained using an X-probe calibrated by a geometric procedure refined extensively to ensure the highest accuracy of measurement.

Wall shear stress was measured by a surface differential pressure gauge or surface fence and followed comprehensive techniques developed by Gur and Leehey of the Acoustics and Vibration Laboratory of the Massachusetts Institute of Technology. The

fence was calibrated at the fence position by obtaining mean velocity profiles in the unmanipulated flow with the same X-probe used to obtain the manipulated profile data. By numerically fitting the profiles to Coles' "law of the wall" data [3], the value of u_τ and, hence, τ_w for specific flow conditions was determined. The ΔP across the fence then becomes the measurable quantity from which τ_w is extracted.

1.2 Objectives

Objectives of the present research fall into two main categories, those involving the measurement process and those involving the measured parameters. Regarding the measurement process, the objectives are to:

- (1) investigate experimentally various calibration procedures in X-probe hot-wire anemometry
- (2) refine the calibration process to obtain the highest measurement accuracy with the greatest computational efficiency
- (3) adapt and/or devise hardware and software components to support the data acquisition required by the refined calibration procedure.

Regarding the parameters to measure, wall shear stress and Reynolds stress, the objectives are to:

- (1) measure the variation of wall shear stress downstream of a honeycomb boundary layer manipulator, of fixed length and hole size, at different free stream velocities
- (2) concurrently with wall shear stress measurements, measure the variation in Reynolds stress profiles downstream of the manipulators
- (3) compare measured parameters with results of previous investigators and interpret the findings
- (4) evaluate manipulator influences on Reynolds and wall shear stresses and assess the correspondence between the influences at each measurement location.

2 Equipment Description

2.1 Facility and Equipment

2.1.1 Wind Tunnel

All data were collected in the low-turbulence, low-noise wind tunnel in the MIT Acoustics and Vibration Laboratory illustrated in Figure 2.1. Documentation on the design and construction of the wind tunnel facility may be found in Hanson [10]. A General Electric Model DC-300 blower motor draws air into the tunnel test section through inlet honeycomb matrices and filter screens. A General Electric adjustable speed drive in combination with a Red Lion Controls Model DT3D controller regulates motor speed to within ± 0.2 revolutions per minute (RPM) with digital display accurate to 0.1 RPM.

The test sections are inside the blockhouse and consist of a closed duct and semi-open jet configuration with no side walls. The closed section extends approximately nine feet from the inlet end of the blockhouse while the semi-open section is 4.25 feet long. The zero point for the traversing system is situated 3.3 feet from the inlet end of the blockhouse and ranges over 90% of the semi-open section. The internal cross section of the duct is square, fifteen inches on a side (38 cm x 38 cm). The duct portion has smooth, masonite side walls with several access windows mounted along its length. Rectangular plexiglass test plates are mounted on support rails to form the lower boundary in the semi-open section. The upper boundary is wooden and adapted to support the probe traversing system described below. The plexiglass plates were joined together edge-to-edge with gaps filled by putty. The putty seams were then sanded with 600 grit paper to form a continuous smooth surface. Boundary layer measurements were made above this surface.

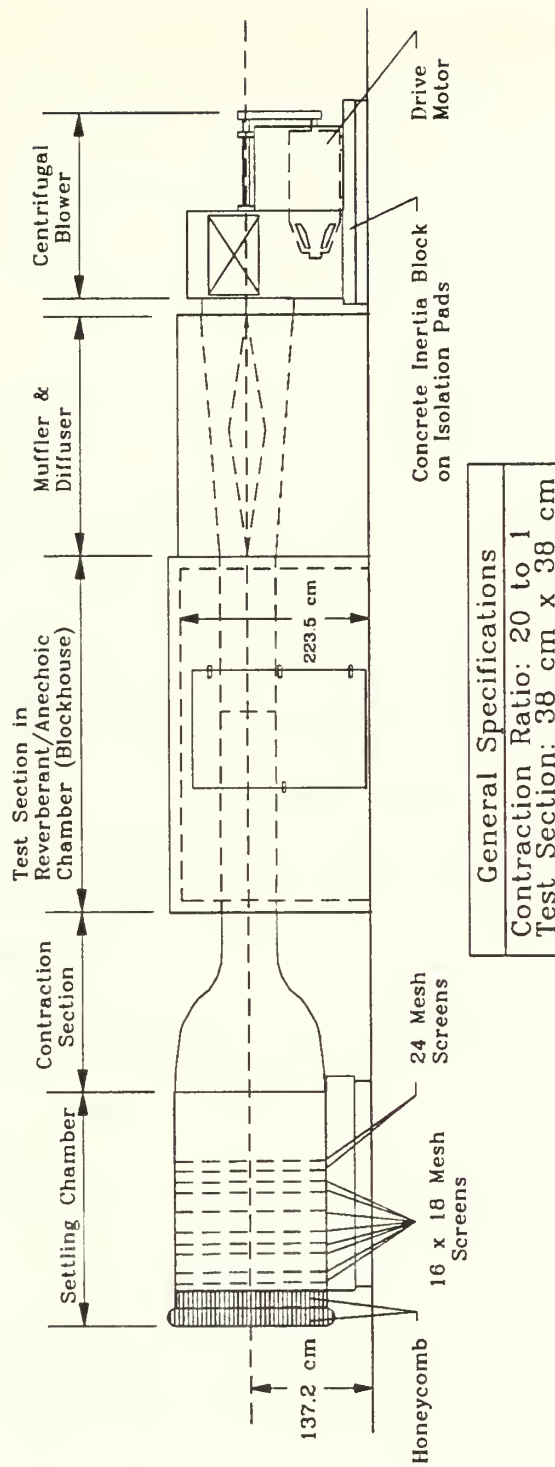


Figure 2.1 Wind Tunnel Facility

In order to ensure a stable boundary layer at the location of the surface fence at all free stream speeds, a seven centimeter (streamwise) #36 grit sandpaper trip was attached to the lower wall near the entrance to the tunnel test section. The trip spanned the entire width of the test section. Manipulators were placed well downstream of the trip.

2.1.2 Traverse

Positioning of X-probes in the boundary layer or in the stream is accomplished by a traversing system specifically designed for the wind tunnel by the former MIT Instrumentation Laboratory (Cambridge, Massachusetts). Two separate motor sub-systems control the position of the probe vertically above the test plate and horizontally along the plate in the stream direction. For horizontal control a motor drives a cable system in forward or reverse to apply force to the traverse cart. The cart's wheels ride on tracks mounted to the upper boundary of the test sections. Sensitivity in the stream direction is 0.05 inches.

A second motor mounted on the cart drives a rotating disk which forces a threaded rod vertically upward or downward with 0.0005 inch sensitivity. Attached to the rod is a foil-shaped, hollow aluminum arm which penetrates into the tunnel test section through a padded slot in the upper boundary of the test section. A dual sensor probe support rod (TSI Model 1155) is mounted inside the aluminum fairing at foil maximum diameter and protrudes at the lower end of the fairing for easy probe mounting. Dual coaxial electrical leads run through the probe support from two BNC connectors to a dual sensor female connector at the probe end. Figure 2.2 illustrates the traverse cart and mounted probe situated in the tunnel test section.

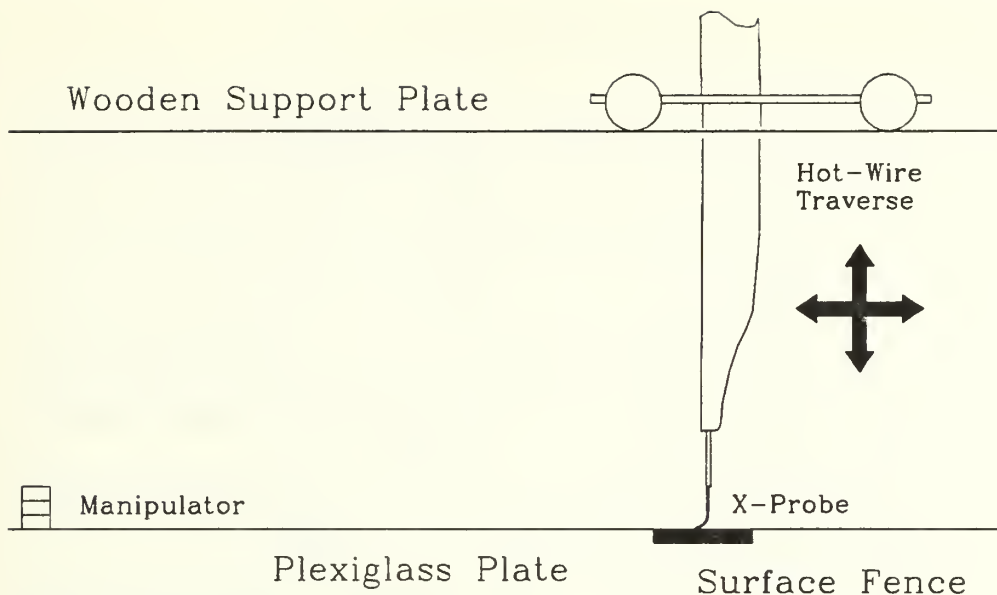


Figure 2.2 Traverse System Schematic

2.2 Velocity Probes

The X-probe used in the experiments was a TSI model 1243-T1.5 with platinum-coated tungsten hot wire sensors. The dual sensor cylindrical probe is specially designed for boundary layer measurements since the probe body and sensor support needles form a "J" shape. The design provides minimum disturbance to the flow near solid boundaries. Probe and sensor characteristics are summarized in Table 2.1 [11].

The sensor wires have enlarged stems at both ends for soldering to the probe support needles. When placed in the flow, one sensor slopes at 45° to and in the flow direction while the second sensor is aligned perpendicular to the first such that it too slopes at 45° to and in the flow direction in the opposite sense. The two sensors lie in parallel planes 1.0 millimeter (0.04 inches) apart, and when placed in the flow, their centers are the same height above a horizontal reference plane. Since the sensors are spatially separate, use of an X-probe configured in the described manner assumes that the flow structure at a given height above the lower wall surface does not vary in the spanwise direction.



Table 2.1 X-Probe Characteristics

Parameter	Value
Diameter (D) of Sensing Area, μm (in)	4 (0.00015)
Length (L) of Sensing Area, mm (in)	1.25 (0.050)
Aspect Ratio (L/D)	312.5
Distance Between Supports, mm (in)	1.5 (0.06)
Velocity Range, m/sec (ft/sec)	0.15-200 (0.5-600)
Maximum Ambient Temperature ($^{\circ}\text{C}$)	150
Maximum Operating Temperature ($^{\circ}\text{C}$)	300
Recommended Operating Temperature ($^{\circ}\text{C}$)	250
Resistance Temperature Coefficient($\Omega/^{\circ}\text{C}$)	0.0042
Upper Frequency Response @ 100 m/sec, kHz (Constant Temperature Mode)	600
Nominal Ambient Resistance, (Ω)	6
Nominal Operating Resistance, (Ω)	10.8

2.3 Pressure Probes

2.3.1 Pitot

A right-angle Pitot tube, inserted into the flow near the center of the tunnel test section, provided a pressure signal from which streamwise velocity was calculated. The X-probe was calibrated using the velocities obtained from the Pitot. The Pitot was connected to a Validyne DP15-TL pressure transducer which provided a proportional electrical signal to a Validyne CD23 Pressure Transducer. Further discussion of the Pitot's role in the measurement process appears in Sections 2.5 and 3.1 below.

2.3.2 Surface Differential Pressure Gauge

Wall shear stress measurements were made with a surface differential pressure gauge known as a surface fence. The fence is a ridge transverse to the flow protruding into the flow approximately 0.002 inches. This height resulted in an h^+ ranging from approximately 1.8 at the lowest speed used in manipulated measurements to a value of 2.54 at the highest speed. These values of h^+ permitted the use of a direct calibration approach as outlined below. The low fence height resulted in negligible disturbance of the mean flow since the fence remained within the buffer region of the boundary layer. Also, fence aspect ratio (≈ 250), length to height, is sufficient to ensure negligible fence tip effects. The fence illustrated in Figure 2.4 was flush-mounted into the plexiglass plate in a fixed position one foot upstream of the semi-open tunnel test section. Flow over the fence results in a pressure drop between the upstream and downstream sides. Two taps on either side of the fence transmit the pressures to a Validyne CD23 Pressure Transducer. The proportional signal from the Validyne enters a MASSCOMP A/D converter channel. Software transforms the input signal into a pressure drop in Pascals.

The pressure chamber gaps on either side of the fence are 0.002 inches wide by 0.12 inches in length. The gap length in viscous units ranged from 108 at the lowest manipulated measurement speed (15 m/sec) to 150 at the highest (23 m/sec). Likewise, the fence length of 0.5 inches, in viscous units ranged from 450 to 630. Other relevant dimensions are provided in Figure 2.3.

The wall shear stress at the surface fence can be determined from the pressure drop across the fence [12]. Calibration of the fence was accomplished by obtaining unmanipulated mean velocity profiles with the X-probe over a range of stream velocities and numerically fitting each to Coles' law of the wall relationship to obtain the friction velocity. The wall shear stress for each profile follows directly ($\tau_w = \rho u_\tau^2$). Leehey and

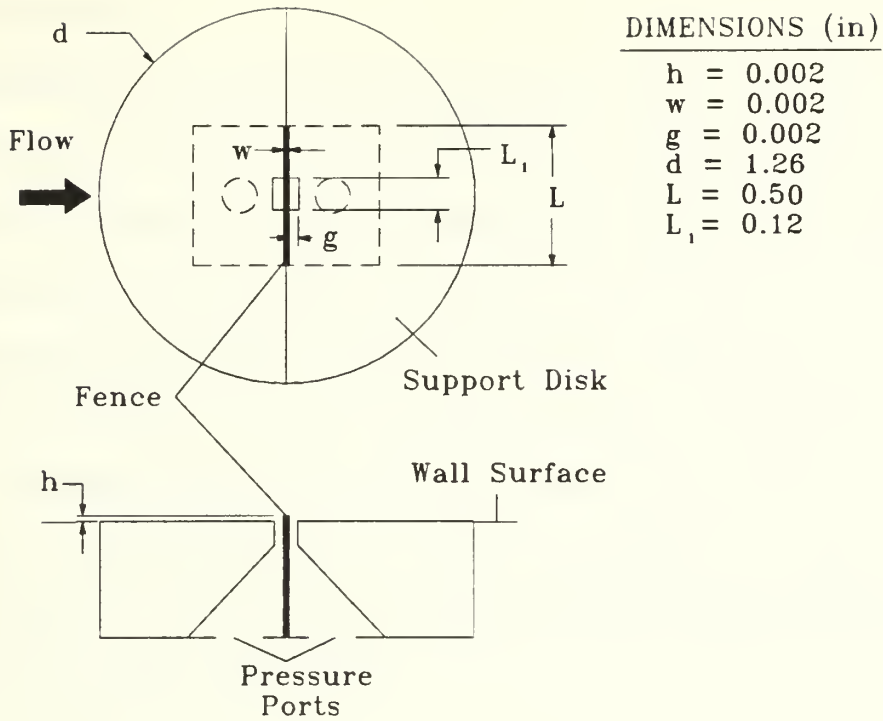


Figure 2.3 Surface Differential Pressure Gauge

Gur used this approach to obtain a functional relationship between differential pressure across the fence and wall shear stress given by

$$\Delta P = a \tau_w^n \quad (h^+ > 1) \quad (2.1)$$

where the exponent n is approximately 1.5. With the fence calibrated, wall shear stress under manipulated flow conditions was measured. Gur and Leehey make use of an alternative non-dimensional expression for the response of the surface fence.

$$\frac{\Delta P}{\tau_w} = f(h^+) \quad (2.2)$$

For the surface fence data collected during the boundary layer measurements, Equation (2.2) was also verified to be consistent with (2.1) and with the findings of Gur and Leehey.

2.4 Manipulators

The manipulators chosen were the honeycomb variety with a length of 0.625 inches and hole size of 0.125 inches. In viscous unit the hole size (d^+) ranged from 113 to 158. The hole size and length were based on the findings of Roth and Leehey who found these dimensions to reduce wall shear stress significantly to a distance of at least $300 \delta^*_{und}$ downstream of the manipulator [6]. Since the differences in manipulator heights considered for the experiment did not vary widely, no alteration of the length scale was justified. The length selected sufficiently refined the flow structure such that the manipulator's influence extended well downstream. Two views of a manipulator are provided in Figure 2.3. The manipulators were constructed of aluminum with a web thickness of approximately 0.003 inches.

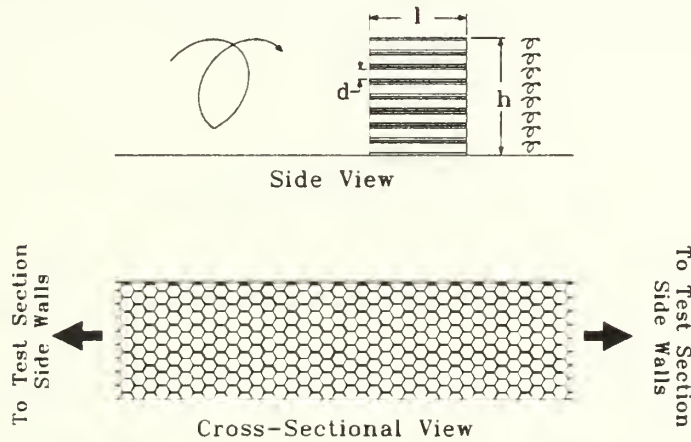


Figure 2.4 Honeycomb Manipulator Schematic

To maintain unidirectional mean flow, the manipulator extended the full width of the tunnel section and was positioned such that the side walls of the honeycomb passages were parallel to the mean flow. The manipulators were fixed to the lower tunnel wall using a thin layer of silicone rubber adhesive. A manipulator of a specified height was positioned upstream of the surface fence. Surface fence and X-probe data were collected at three different speeds ($U_\infty = 15, 19, \text{ and } 23 \text{ m/sec}$). The manipulator was then

removed, and the surface cleaned smooth. An identically configured manipulator of different height (one height was repeated) was then attached at a different position upstream of the fence so that " $h = \delta$ ", and the measurement procedure repeated. The distance between the manipulator and the surface fence (or the stream position of the profile measurement) is represented by the symbol x_{BLM} . In this study x_{BLM} had values of 4, 12, 25, 65, 100, and 150 centimeters.

Manipulator height was selected to approximate the undisturbed boundary layer thickness based on its position relative to a virtual origin. Indications from the work of Roth and Leehey are that the manipulator effectiveness is optimized under this condition [6]. For flow over a flat plate, the relationship governing the variation of turbulent displacement thickness δ^* with distance x downstream from a virtual origin is determined experimentally as

$$\delta^*(x) = .046x \left(\frac{U_{\infty} x}{\nu} \right)^{-\frac{1}{5}}, \quad (2.3)$$

by approximating the displacement thickness as one-eighth the boundary layer thickness [13]. By calculating the displacement thickness of the unmanipulated boundary layers at a given free stream speed, the virtual origin of the flow was determined. The virtual origins of the tripped, unmanipulated boundary layers at 15, 19, and 23 meters per second were respectively 3.52, 3.95, and 4.67 meters upstream of the measurement location (the fence). The center free stream speed of 19 meters per second was the reference speed for the determination of δ where each BLM was located. By determining the position of a given manipulator relative to the virtual origin, Equation (2.3) provided δ ($= 8\delta^*$).

Manipulator height and positions are summarized in Table 2.2.

Table 2.2 Manipulator Positions and Heights

x_{BLM} (cm)	h_{BLM} (cm)	Number of Holes
4	3.5	11
12	5.1	16
25	5.1	16
65	4.1	13
100	3.2	10
150	3.8	12

The trend of increasing manipulator height as the measurement position from the manipulator increases, as dictated by Equation (2.3), was intentionally altered at the nearest and farthest measurement positions. The intent was to augment the range of the ratio of manipulator height to incident boundary layer thickness δ^*_{und} in order to assess the relationship between this ratio and wall shear stress (or friction coefficient). A more comprehensive approach would set manipulator height optimally to the boundary layer thickness for the given free stream speed and distance from the virtual origin. These measurements would be followed by two more sets of measurements, one with a constant height manipulator which keeps the BLM in the lower 50% of the boundary layer at all measurement positions, another with a constant height BLM always exceeding the boundary layer thickness at the measurement point. In this way a broad range in h_{BLM}/δ^*_{und} can be obtained.

The intent in using a honeycomb manipulator with a height approximating δ at the manipulator location is to reduce the magnitude of the fluctuating velocity components throughout a major portion of the boundary layer thickness. Single or tandem strip manipulators should be less effective in accomplishing this end. The honeycomb network will readily remove the large eddy flow structures also. The wake of the

manipulator will initially contain small scale vortical structures at different levels in the boundary layer having rotations in opposite directions in the x - y plane (one direction only shown in Figure 2.4) [5]. Superposition of these small structures immediately downstream of the manipulator should effect a reduction in mean and fluctuating velocities and impede the transport of turbulent energy toward the wall. Farther downstream of the manipulator the small scale structures will merge and restore a larger scale structure to the boundary layer flow.

2.5 Data Acquisition System

A MASSCOMP Model 5400 32-bit computer is the core of the data acquisition system. The computer system contains the Model AD12FA Analog-to-Digital (A/D) twelve bit converter with a one megahertz throughput. The AD12FA is a versatile unit consisting of 16 channels with an input voltage range from -10 to +10 volts. Two twelve bit D/A converters provide output over the same range. Gain is programmable across the channels separately.

The pressure signal from the Pitot is translated into a proportional electrical signal by a Validyne variable reluctance differential pressure transducer (Model DP15-TL) in conjunction with a Validyne Model CD23 Digital Transducer Indicator. The CD23 produces a voltage signal equal to one-tenth the absolute air pressure in millimeters of water. A voltage divider further reduces CD23 output voltage by one-half to accommodate the MASSCOMP AD12FA input voltage range. The Validyne components are regularly calibrated to a Betz water manometer.

Since the X-probe is operated as a constant temperature anemometer, each sensor forms a resistance element of a Wheatstone Bridge. Two Dantec Model 56C01/17 Constant Temperature Anemometers are separately balanced to each sensor so that each is operated at the desired overheat ratio (OHR). To ensure maximum probe sensitivity an



OHR of 1.9 was selected to determine bridge settings. This overheat value corresponds to an operating temperature near the recommended. Output signals from the bridges nominally range between 1.0-4.0 volts depending upon local speed and the type and size of the sensor.

Sensor frequency response was evaluated by performing a Square Wave Test with flow incident upon the probe at the stream speed for each measurement. A square wave generator internal to the Dantec anemometers provided the test signals with response output displayed on an oscilloscope. Measured in this way, each sensor's response was 50 kHz.

3 Experiment Description

3.1 X-Probe Calibration

The first X-probe calibration procedures applied King's Law of Cooling to determine sensor electrical response [14,15]. A detailed account of such an approach was published by Schubauer and Klebanoff in work performed for the National Advisory Committee for Aeronautics (NACA) [16]. To obtain high accuracy with a cooling law calibration approach, precise knowledge of each sensor's alignment to the flow is required. By pitching the probe relative to the flow for different calibration speeds, the alignment of each sensor to the flow at zero pitch angle can be determined [17,18]. Since other calibration approaches exist which pitch the probe during the calibration procedure but do not require precise knowledge of sensor alignment, a cooling law approach to calibration offered no advantages. The overriding consideration in rejecting a cooling law calibration approach in the present application was the inherent assumption in the procedure that \bar{v} is negligible. The assumption is valid for unmanipulated unidirectional mean flow but not for manipulated flows, especially near the manipulator.

Recently, X-probe calibration techniques have been devised which eliminate assumptions regarding sensor cooling laws and specific angular alignment between the sensor support needles. The procedure involves pitching the probe relative to the flow at each calibration speed and recording the speed, angle, and sensor voltages. The geometry for the procedure is illustrated in Figure 3.1. The probe axis bisects the projected intersection of the two sensors such that the free stream velocity would normally parallel the axis. During calibration α is the pitch angle of the probe axis relative to the free stream. During boundary layer measurements Q represents the relative velocity with respect to the probe axis at any instant of time from which u and v can be calculated.



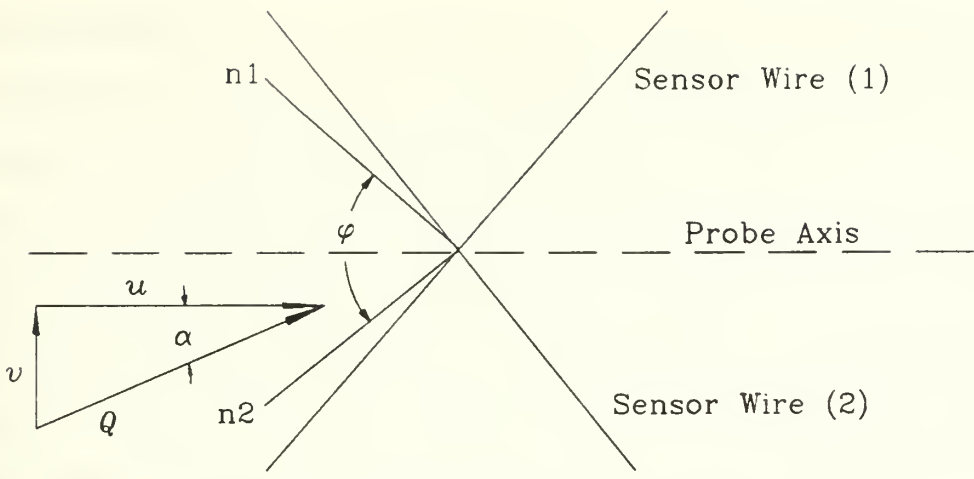


Figure 3.1 X-Probe Velocity Geometry

The underlying concept behind the calibration approach is that a unique voltage pair exists across the sensors for a specific pair of velocity components u and v . For the concept to apply, the velocity along each sensor must be spatially constant, flow must lie in the plane formed by the two sensors (actually, a theoretical plane onto which both sensors are projected), and the flow vector Q lies between the angle formed by normals to the sensors, $n1$ and $n2$ (see angle ϕ , Figure 3.1) or by the intersection angle of the sensors themselves, whichever is smaller [19]. Different numerical schemes may be adopted to structure the calibration data for use in subsequent boundary layer measurements.

When Willmarth and Bogar used the velocity-angle-voltage (VAV) calibration approach, they computed velocity components u and v from the calibration values of Q and α and matched these to corresponding voltage pairs [19]. A calibration table or grid was developed separately for u and v and stored for later use. During measurements in the boundary layer instantaneous voltages from the sensors would in principle fall within a "voltage rectangle" in the grid, from which the values of u and v are obtained by interpolation. Near the wall ($y^+ \leq 65$) voltage fluctuations frequently extended beyond the grid limits resulting in serious errors in values for $\sqrt{u_w'^2}$, $\sqrt{v_w'^2}$, and $\overline{u'v'}$ compared with data obtained from X-probes calibrated according to cooling laws [9]. Willmarth

and Bogar speculate on the causes and significance of this problem and conclude that small scale turbulent flow structures produce different flow conditions at each sensor since the sensors are spatially separate [19]. Thus, although the calibration voltage grid encompasses the voltage range anticipated for the intended measurements, velocities along and at each sensor may induce a voltage response uncharacteristic of the calibration grid. The effect may be compounded by velocity components in the third dimension. Such problems are inherent in the assumptions and physical characteristics of the probes used in hot-wire anemometry and would invalidate both cooling law and VAV calibration approaches. Since other factors such as sensor size affect probe response under turbulent conditions, all must be considered before evaluating the appropriateness of a given calibration scheme. For example, Willmarth and Bogar used sensors much smaller than those commercially available or those used by previous researchers such as Klebanoff, a length and spacing of 100 μm and diameter of 0.5 μm (see Table 2.1 for comparison). Lueptow used equivalently small probes and the VAV calibration method and likewise documented "out-of-grid" voltages near the wall [20]. However, in comparing their Reynolds stress measurements near the wall to those found by Klebanoff and others, Willmarth's and Bogar's values were much greater while those of Lueptow were much less.

The difficulties encountered by Willmarth and Bogar and Lueptow near the wall were likewise encountered in the present work. The poor near-wall data obtained with dual sensors can be attributed to sensor spatial separation, flow interference due to sensor supports, and heat transfer to the cooler wall. Radiation losses appear to dominate the heat transfer process [14]. By placing an X-probe at the surface in a no flow condition and stepping away vertically in one-thousandth inch increments, a definite voltage or temperature gradient was observed when using both a standard TSI probe and a TSI miniature dual sensor probe (2.5 μm diameter, 0.5 mm active length). The temperature

gradient became flat when the lower supports were approximately 0.025 inches from the wall or when the probe axis was approximately .045 inches from the wall. Since radiative heat transfer is insensitive to flow effects, the gradient will exist under flow conditions and introduce voltage errors into the measurements. The errors in v were determined as high as 20% when the voltage error was only 3%. This is due both to the magnitude of v ($|v| \leq 1.5 \text{ m/sec}$) and the slope of the v -calibration surface for near zero velocities (see Figure 3.3 below). These errors would particularly influence the values of $\sqrt{v'^2}$ and $\overline{u'v'}$. No suitable correction scheme could be devised to circumvent poor probe performance in the near wall region. Thus, the near wall values of Reynolds stress could not be used to infer and/or confirm the value of friction velocity (or wall shear stress) for the different flow conditions encountered. The constant stress layer approximation given by Equation (3.1), where the slope of the mean velocity profile becomes negligibly small in comparison to the Reynolds stress term, failed to be of use [21].

$$\tau_w = -\rho \overline{u'v'} + \mu \frac{\partial \overline{u}}{\partial y} \approx -\rho \overline{u'v'} \quad (3.1)$$

Even the calculational aspects of the calibration process were examined in an attempt to improve accuracy in the near wall region. The numerical schemes documented in the literature vary widely in complexity and computational efficiency. Willmarth and Bogar calculated partial derivatives of velocities with respect to voltages at nodes of the calibration voltage grid in order to interpolate voltages for conversion to velocities [19]. Johnson and Eckelmann preferred a two-dimensional Taylor series expansion of voltages to obtain first and second order partial derivatives; a total of twelve calibration voltages and partial derivatives were required for each point of the calibration grid [22]. Lueptow et al constructed velocity look-up tables suitable for two dimensional linear interpolation but only after conducting polynomial and/or spline fits relating resultant velocities Q and angles α to voltage pairs in a finely divided voltage grid [23].

Despite the evolution of the aforementioned numerical techniques, a more direct approach was adopted. From the calibration data of u , v , E_{0_1} , and E_{0_2} a linear least squares fit was performed to determine separately the coefficients for a two variable polynomial in E_{0_1} and E_{0_2} , one polynomial in u , the other in v . Oster and Wygnanski used third-degree, ten coefficient two-dimensional polynomials [24]. The approach used herein expanded upon the polynomial strategy by raising the two-dimensional polynomial to degree four and including all twenty-five exponent pair combinations of E_{0_1} and E_{0_2} . The resulting expressions for u and v appear in equations (3.2) and (3.3).

$$u = \sum_{j=0}^4 \sum_{i=0}^4 a_{ij} E_{0_1}^i E_{0_2}^j \quad (3.2)$$

$$v = \sum_{j=0}^4 \sum_{i=0}^4 b_{ij} E_{0_1}^i E_{0_2}^j \quad (3.3)$$

The twenty-five coefficients determined for each velocity component were incorporated into a conversion routine to calculate instantaneous velocity components u and v from voltages obtained from the sensors during boundary layer measurements. By applying this procedure separate calibration surfaces for u and v were constructed. Actual calibration surfaces with the functional form of Equations (3.2) and (3.3) appear in Figures 3.2 and 3.3, respectively. The instantaneous voltages encountered during boundary layer measurements lie within the calibration voltage range of each sensor; thus, the two surfaces obtained from the least squares fit provide all possible velocity components measured as the X-probe traverses the boundary layer. The u and v velocity components are calculated directly from the appropriate functions vice interpolated from a look-up table. Both the functional and Leuptow look-up table methods were evaluated prior to boundary layer measurements to ascertain the accuracy of each. The functions specified in Equations (3.2) and (3.3) were equivalently accurate to the look-up table method when comparing calculated or interpolated velocities to original calibration



velocities for a given voltage pair. In terms of computation time during data acquisition, the conversion functions proved twice as fast as the look-up table approach. Computational speed was a major consideration since small distance steps were planned and implemented in measuring the boundary layer profiles to obtain a detailed picture of small scale disturbances.

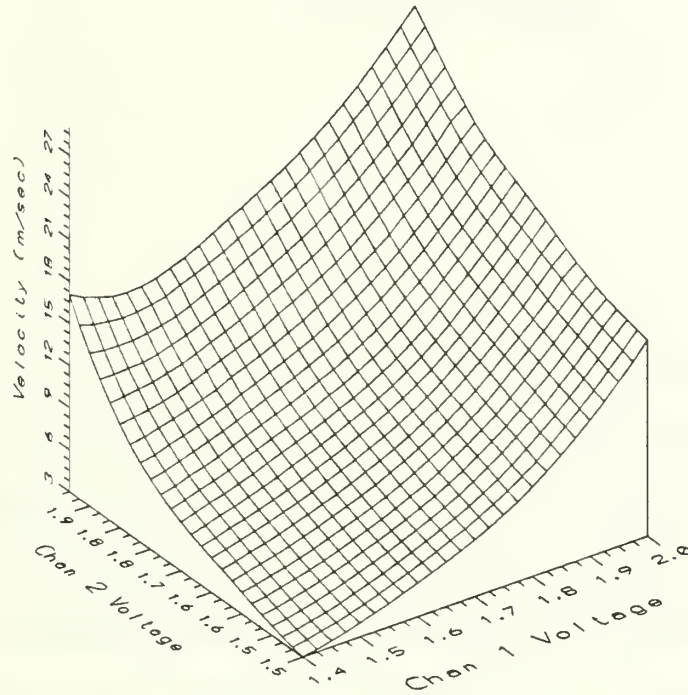


Figure 3.2 Stream Velocity Calibration Surface

In practice the calibration procedure requires that either the tunnel speed be kept fixed while the probe is pitched at various angles to the flow or that the probe be exposed to the full range of calibration speeds at a given angle, which is repeatedly re-set to completion. The facilities required that the latter procedure be followed. Calibration angle was manually re-set by positioning the traverse cart onto a step support positioned for equal positive and negative calibration angles. Figure 3.4 depicts the physical arrangement utilized to determine the calibrations surfaces. Seven probe pitch angles (0° , $\pm 9^\circ$, $\pm 18^\circ$, $\pm 36^\circ$) were set by using the step device illustrated. With a given angle set, the

The first part of the paper discusses the importance of the study of the history of the English language. It is argued that the study of the history of the English language is essential for a full understanding of the language and its development. The paper then goes on to discuss the various factors that have influenced the development of the English language, including the influence of other languages, the influence of social and cultural changes, and the influence of technological advances.

The second part of the paper discusses the importance of the study of the history of the English language. It is argued that the study of the history of the English language is essential for a full understanding of the language and its development. The paper then goes on to discuss the various factors that have influenced the development of the English language, including the influence of other languages, the influence of social and cultural changes, and the influence of technological advances.

The third part of the paper discusses the importance of the study of the history of the English language. It is argued that the study of the history of the English language is essential for a full understanding of the language and its development. The paper then goes on to discuss the various factors that have influenced the development of the English language, including the influence of other languages, the influence of social and cultural changes, and the influence of technological advances.

The fourth part of the paper discusses the importance of the study of the history of the English language. It is argued that the study of the history of the English language is essential for a full understanding of the language and its development. The paper then goes on to discuss the various factors that have influenced the development of the English language, including the influence of other languages, the influence of social and cultural changes, and the influence of technological advances.

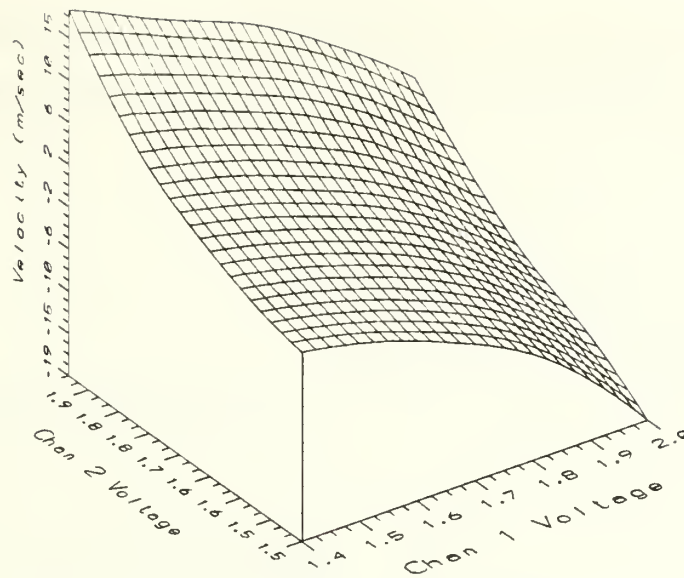


Figure 3.3 Normal Velocity Calibration Surface

wind tunnel velocity was varied from zero (to establish reference Pitot pressure) to a value a minimum of 10% above the maximum free stream velocity used for boundary layer measurements. Sufficient time was allowed for the flow to stabilize before the voltages across each sensor were measured. The procedure was repeated for each angle ensuring that the temperature, measured at the wind tunnel settling chamber inlet (see Figure 2.1), remained within a $\pm 3^{\circ}\text{F}$ band. By adjusting the traverse position, the probe remained within the central core region of the flow away from the tunnel test section walls. The final calibration measurement was taken at the 0° position with the traverse locked in position for boundary layer measurements. Voltages for stream speeds less than 1.5 meters per second were discarded before determining the calibration surfaces since these were found to be influenced by mutual heat transfer between the sensors. Boundary layer measurements near the wall were subsequently limited to flow conditions corresponding to a local mean velocity in which the minimum *instantaneous* velocity is 1.5 meters per second. Since the probe axis of the TSI X-probe used in this study cannot be positioned closer than 0.375 millimeters of the wall, near-wall measurements are valid

when the combination of free stream speed and streamwise position of the probe relative to the virtual origin of the boundary layer result in no instantaneous local speeds below 1.5 meters per second.

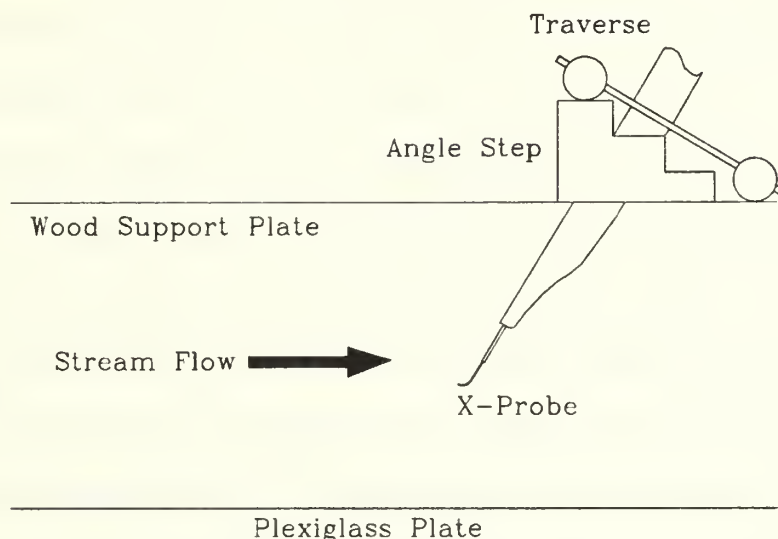


Figure 3.4 Wind Tunnel Calibration Configuration

After discarding the calibration data corresponding to velocities along the probe axis less than 1.5 meters per second, two sets of eighty-four voltage-voltage-velocity triplets remained for determination of the calibration surfaces. Although Johnson and Eckelmann recommend fitting such surfaces only for the calibration velocities corresponding to a speed range to which the probe is subjected during experimental conditions [22], the coefficients determined were fit for a speed range of 2-35 meters per second. Justifications for this approach are many. First, the minimum mean local speed experienced by the probe near the wall was approximately six meters per second. Second, in attempting linear least squares fits over restricted speed ranges with third and fourth order two dimensional polynomials (sums running to 3 and 4 in Equations (3.7) and (3.8)), the variance between measured speeds and speeds calculated from the derived functions remained essentially constant. Third and most importantly, the magnitude of the relative error between measured and calculated values of u and v for the speed range

encountered in the boundary layers (5-23 meters per second) was typically 1% or less, with some higher deviations of 2%-4%, primarily in v , at a few select points, particularly at high calibration pitch angles where the influence of the sensor supports begin to disturb the flow experienced by the probe. The fourth order two-dimensional polynomial functions had slightly lower variances and relative errors than the third order functions and were used in the calibration procedure. Restricting the fit to a narrower speed range, however, had no influence on the relative error on the whole in the speed range of interest. An individual relative error between a measured and calculated velocity may increase from 0.8% to 1.1% when comparing two possible calibration ranges, while another may decrease from -0.4% to -0.2%. Thus, with no advantage in selecting a specific calibration range based on the speed range anticipated during boundary layer measurements, one calibration surface each for u and v applied to all boundary layer measurements. Differences in u between measured and calculated values, using coefficients from the least squares fit, resulted in an error standard deviation equal to 0.044 meters per second. The error standard deviation in v was 0.051 meters per second. Although the largest magnitude velocities during calibration occur in the stream direction, due to the large pitch angles of the probe, large values of v (up to 23 meters per second) are also observed.

3.2 Boundary Layer Measurements

Once the X-probe was calibrated, boundary layer measurements proceeded. The probe sensors were positioned just forward of the fence ridge with the probe lowered to the surface. The first step was to obtain velocity profiles for the unmanipulated turbulent boundary layer at the speeds of interest. Additional unmanipulated profiles were obtained at speeds above 23 meters per second and below 15 meters per second to accomplish a proper calibration of the surface fence. The data acquisition program used

the X-probe calibration coefficients to provide an output of the following quantities at each measurement position in the boundary layer: position y , mean stream velocity \bar{u} , mean normal velocity \bar{v} , root mean square fluctuating stream velocity $\sqrt{\overline{u'^2}}$, root mean square fluctuating normal velocity $\sqrt{\overline{v'^2}}$, and Reynolds stress $\overline{u'v'}$. A total of 150,000 voltage pairs were sampled at 8000 Hertz for a total sampling time of 18.75 seconds at each of some 150 positions to a distance of approximately eight centimeters from the wall. The initial position of the probe was established by lowering it with the traverse such that the lower sensor supports were just in contact with the wall surface. The traverse was then stepped away from the wall 0.001 inches and the traverse vertical position indicator zeroed. The estimated distance of the probe axis from the wall was determined by extracting a "y-offset" based on a Coles fitting routine to be discussed forthwith.

Mean stream velocity at each measurement position above the wall surface and the corresponding position relative to the arbitrary zero for each unmanipulated profile formed a data set for determining the friction velocity and probe offset distance from the wall. Experimental data was fit to actual data obtained by Coles for an equilibrium boundary layer [3]. An iterative least squares fitting routine solved simultaneously for friction velocity and offset distance. Coles' data conforms to the law of the wall as expressed by Equation (3.4) where A is 5.75 and B is 5.10 [3].

$$u^+ = A \log_{10}(y^+) + B \quad (3.4)$$

The fit was accomplished over a y^+ ranging from 20 to 200. Figure 3.5 illustrates the law of the wall fit of experimental data for a free stream speed of 19 meters per second for an unmanipulated boundary layer; other speeds are found in Appendix A. With u_τ and offset determined for each profile, a calibration curve for the surface fence was determined (see Section 3.2.3) and boundary layer parameters were accurately determined.

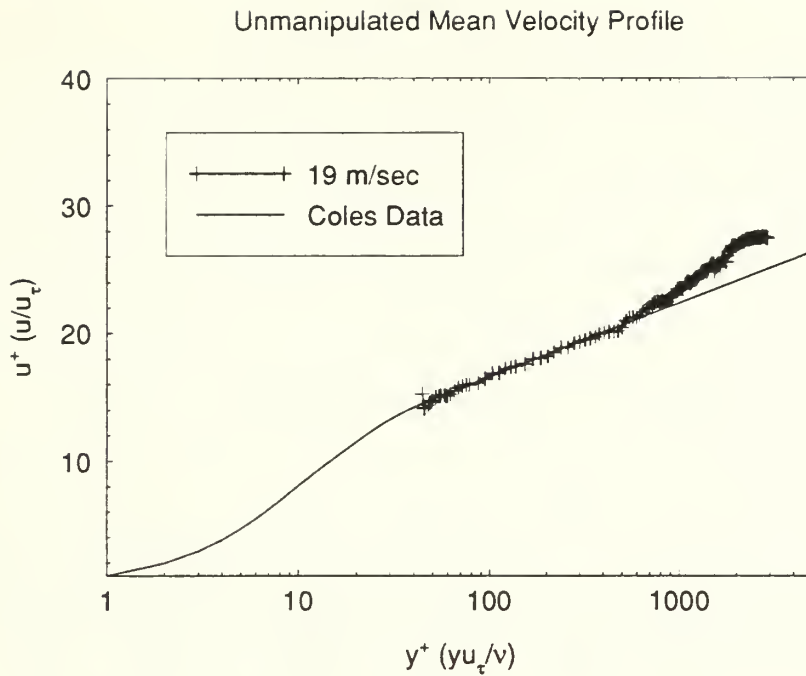


Figure 3.5 Law of the Wall Fit (Unmanipulated, $U_{\infty}=19$ m/sec)

Manipulated profile data was obtained at three different speeds with a BLM in six different positions. All data acquisition parameters and probe positioning routines were identical to those for the unmanipulated profiles. Surface fence differential pressure was converted into wall shear stress and friction velocity by employing the fence calibration curve. In order to determine boundary layer parameters accurately, the sensor offset distance from the wall was determined by using a modified version of the law of the wall fitting routine. With u_{τ} known for each stream speed a value for the y-offset was entered into the analysis program until the slope of mean velocity profile in the range $20 \leq y^{+} \leq 200$ equaled that for the law of the wall profile. The value of y-offset thus determined was added to each raw data value of y, in appropriate units, to establish relationships for calculating boundary layer parameters and producing accurate profile plots. Tables 3.1 through 3.4 summarize the major boundary layer parameters obtained for the three free stream speeds used with manipulators. The symbol H represents the

shape factor, the ratio between the displacement thickness and momentum thickness of the boundary layer, and is presented for completeness only. Figures 3.6 (a) through (f) show the manipulated boundary layer law of the wall fit for a free stream speed of 19 meters per second with the manipulator at each of its six distances from the measurement position. The unusual form of the mean velocity profiles, particularly when the measurements are near the BLM, are discussed in following sub-section.

Table 3.1 Unmanipulated Boundary Layer Parameters

U_{∞} (m/sec)	u_{τ} (m/sec) (Coles)	τ_w (Pa)	δ^* (10^{-3} m)	Re_{δ^*}	C_f (10^{-3})	H
15	0.55	0.366	8.08	7700	2.87	1.43
19	0.67	0.533	8.69	10408	2.63	1.44
23	0.77	0.710	9.35	13478	2.41	1.43

Table 3.2 Manipulated Boundary Layer Parameters ($U_{\infty}=15$ m/sec)

x_{BLM} (cm)	h_{BLM} (cm)	δ^*_{und} (10^{-3} m)	u_{τ} (m/sec) (fence)	τ_w (Pa)	δ^* (10^{-2} m)	Re_{δ^*}	C_f (10^{-3})	H
4	3.5	7.99	0.44	0.233	1.64	15596	1.82	1.60
12	5.1	7.86	0.41	0.205	1.75	16484	1.62	1.53
25	5.1	7.60	0.46	0.259	1.67	15901	2.03	1.54
65	4.1	6.80	0.47	0.269	1.59	15707	1.96	1.62
100	3.2	6.18	0.51	0.309	1.28	12148	2.45	1.52
150	3.8	5.13	0.49	0.292	1.59	15654	2.15	1.56

Table 3.3 Manipulated Boundary Layer Parameters ($U_{\infty}=19$ m/sec)

x_{BLM} (cm)	h_{BLM} (cm)	δ^*_{und} (10^{-3} m)	u_{τ} (m/sec) (fence)	τ_w (Pa)	δ^* (10^{-2} m)	Re_{δ^*}	C_f (10^{-3})	H
4	3.5	8.36	0.54	0.342	1.52	18288	1.65	1.61
12	5.1	8.21	0.52	0.324	1.65	20073	1.54	1.52
25	5.1	7.97	0.56	0.377	1.57	19263	1.78	1.49
65	4.1	7.23	0.60	0.429	1.39	17611	1.92	1.57
100	3.2	6.67	0.62	0.456	1.19	14327	2.19	1.51
150	3.8	5.72	0.60	0.423	1.55	19130	1.96	1.55

Table 3.4 Manipulated Boundary Layer Parameters ($U_{\infty}=23$ m/sec)

x_{BLM} (cm)	h_{BLM} (cm)	δ^*_{und} (10^{-3} m)	u_{τ} (m/sec) (fence)	τ_w (Pa)	δ^* (10^{-2} m)	Re_{δ^*}	C_f (10^{-3})	H
4	3.5	9.17	0.64	0.487	1.50	22367	1.53	1.58
12	5.1	9.03	0.63	0.466	1.67	25222	1.45	1.52
25	5.1	8.84	0.67	0.537	1.56	23225	1.74	1.50
65	4.1	8.20	0.69	0.559	1.38	20535	1.79	1.57
100	3.2	7.64	0.73	0.628	1.15	16808	2.08	1.51
150	3.8	6.79	0.70	0.583	1.42	20860	1.90	1.52

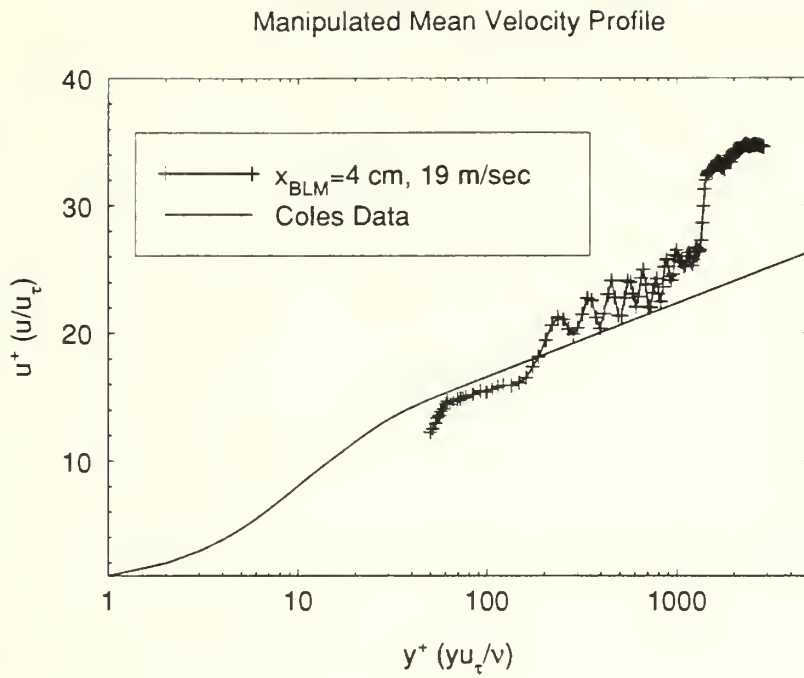


Figure 3.6(a) Law of the Wall Fit ($h_{BLM}=3.5 \text{ cm}$, $U_\infty=19 \text{ m/sec}$)

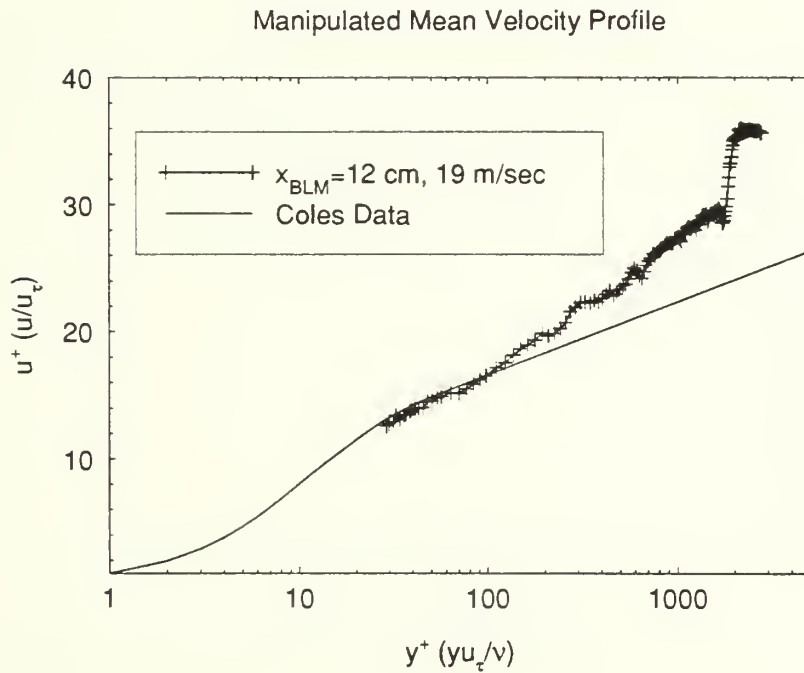


Figure 3.6(b) Law of the Wall Fit ($h_{BLM}=5.1 \text{ cm}$, $U_\infty=19 \text{ m/sec}$)

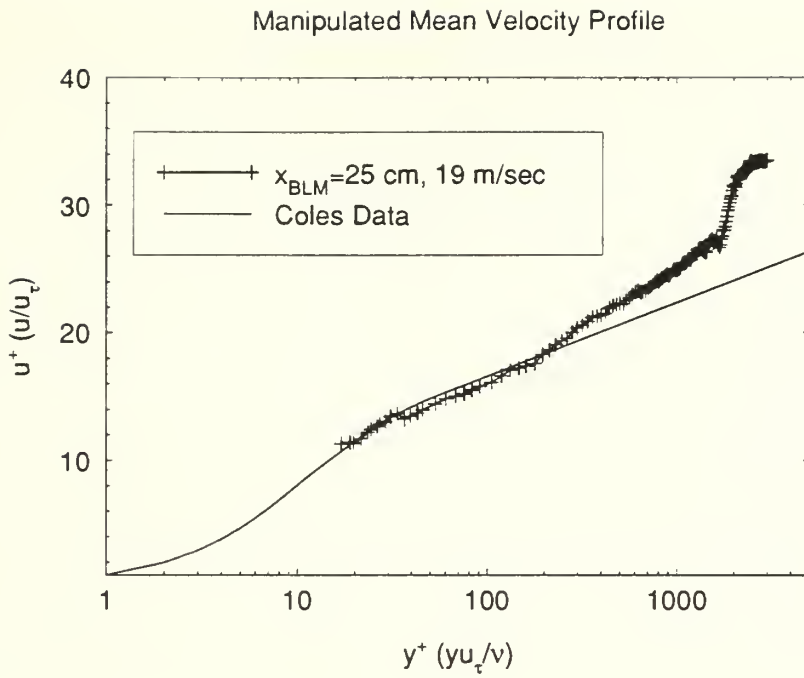


Figure 3.6(c) Law of the Wall Fit ($h_{BLM}=5.1 \text{ cm}$, $U_\infty=19 \text{ m/sec}$)

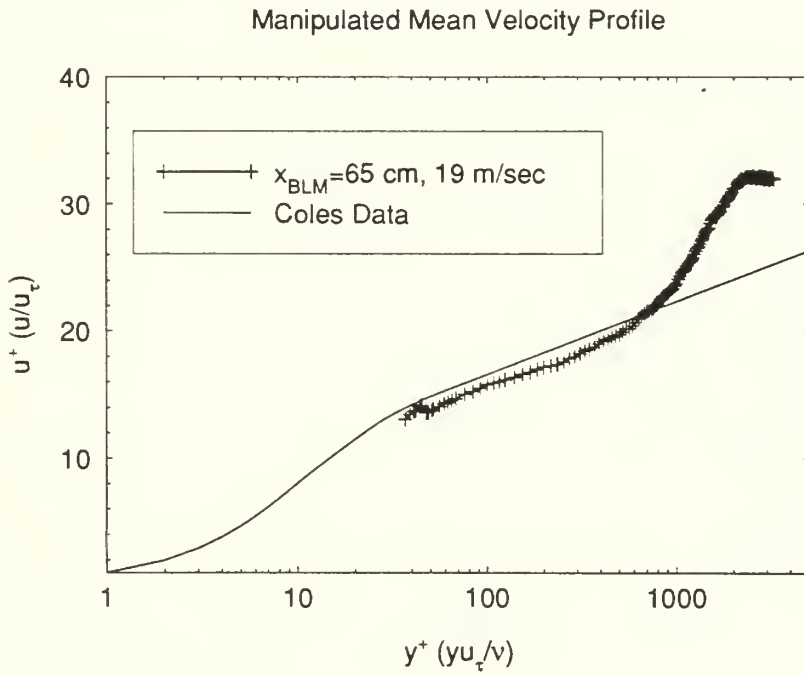


Figure 3.6(d) Law of the Wall Fit ($h_{BLM}=4.1 \text{ cm}$, $U_\infty=19 \text{ m/sec}$)

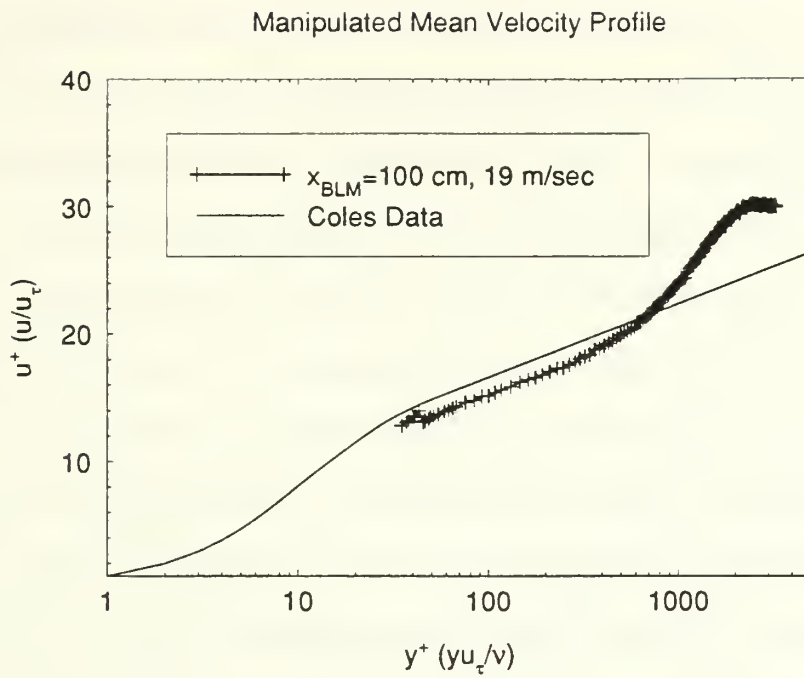


Figure 3.6(e) Law of the Wall Fit ($h_{BLM}=3.2 \text{ cm}$, $U_\infty=19 \text{ m/sec}$)

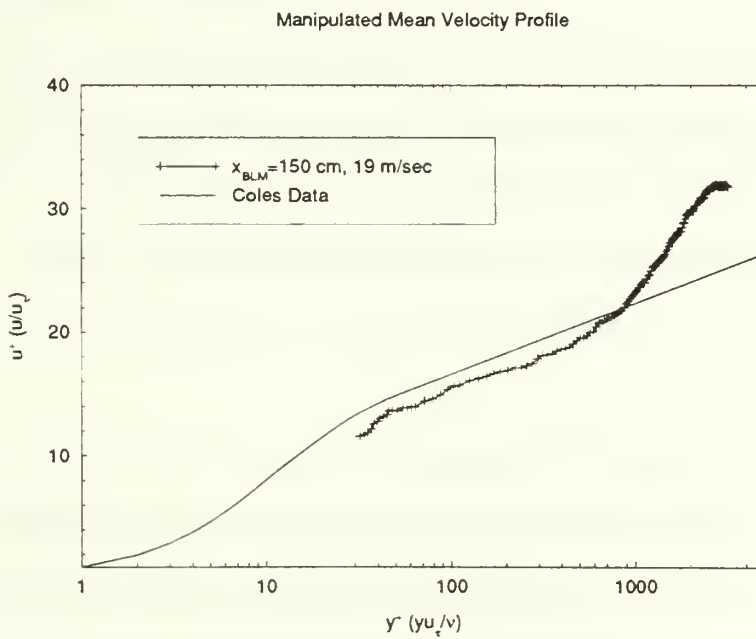


Figure 3.6(f) Law of the Wall Fit ($h_{BLM}=3.8 \text{ cm}$, $U_\infty=19 \text{ m/sec}$)

As seen in Figures 3.6 (a)-(f), Coles' law of the wall does not apply to manipulated boundary layers. When the slope matching is accomplished to determine the value of the y-offset, the mean velocity profile for a manipulated boundary layer parallels the Coles plot for an unmanipulated boundary layer for values of y^+ ranging from 20 to 200 and above; however, the manipulated profile has a values of u^+ either less than or approximately equal to those for the unmanipulated profile. This contradicts the findings of Roth and Leehey where the manipulated values of u^+ everywhere exceeded those of the unmanipulated boundary layer [6]. To determine the validity of the present findings, a consistency check of mean stream velocity ratios between the manipulated and unmanipulated cases was performed for a given y^+ based on the relative magnitudes of friction velocity in each case. No discrepancy was detected nor could any physical argument be found to justify one finding in preference to another.

3.2.1 Unmanipulated Velocity Profiles

Since boundary layer measurements were taken over a relatively narrow speed range, graphical representation of data is limited to measurements in the boundary layer with a free stream speed of 19 meters per second. Results of measurements with free stream speeds at 15 and 23 meters per second closely match those of 19 meters per second. For completeness Appendix A contains relevant plots of data at these other free stream speeds.

The unmanipulated mean velocity profiles obtained for the current measurements adhere in form and proportion to the extensively documented equilibrium turbulent boundary layer profiles measured over flat plates under similar conditions. Figure 3.7 is one such profile with a boundary layer thickness of approximately six centimeters at the point of measurement. The free stream speed of 19 meters per second is a rounded figure based on the averaging of all free stream speeds for both the manipulated and

unmanipulated cases taken with the tunnel fan speed set to a specific RPM (500 $RPM \Leftrightarrow 18.6 \text{ m/sec}$). The same approximation applies to the free stream speeds of 15 and 23 meters per second.

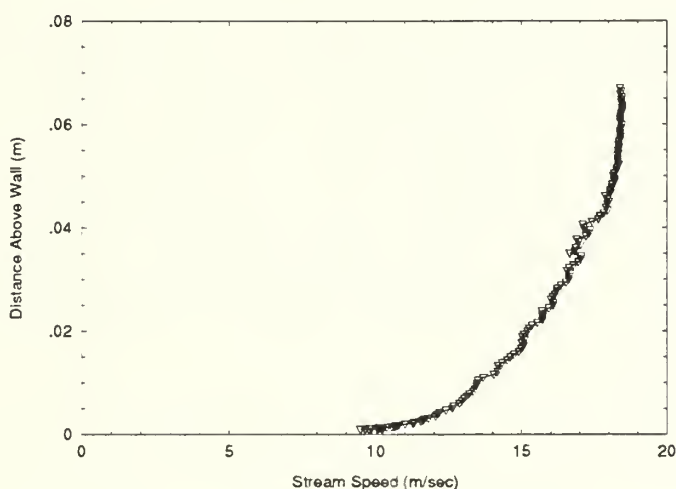


Figure 3.7(a) Unmanipulated Mean Velocity Profile ($U_\infty=19 \text{ m/sec}$)

To specify turbulent flow structure, knowledge of the root-mean-square (rms) fluctuating velocity components is required. For equilibrium turbulent boundary layers above flat plates the profile data obtained by Klebanoff has been recognized as the standard for comparison [16]. Klebanoff obtained his data with single and double sensor hot-wire probes appropriately oriented to the unidirectional mean flow to obtain the rms fluctuating velocities. In comparing the rms streamwise fluctuating velocity profile obtained for unmanipulated flow to that of Klebanoff (Figure 3.7(b)), a close correspondence exists throughout the boundary layer except near the wall. This discrepancy is due to the different measuring devices employed. Near wall hot-wire measurement of the streamwise fluctuating velocity component can only be effectively accomplished with a single sensor probe as used by Klebanoff. An X-probe of the type and size used for the measurements cannot be brought close enough to the wall to resolve

the near-wall peak in $\sqrt{u'^2}$. Additionally, the physical separation of X-probe sensors and heat transfer effects between the wall and sensors introduce voltage errors which corrupt velocity measurements in the near-wall regime. For the free stream speed of 19 meters per second all X-probe data is considered valid when y/δ attains a value of approximately 0.03. As seen in Figure 3.7(b), the correspondence between $\sqrt{u'^2}$ obtained with the X-probe and that obtained by Klebanoff's single sensor probe begins essentially at this point. Thus, the unmanipulated turbulent boundary layer established in the wind tunnel conforms parametrically to the turbulent boundary layers used in many experiments designed to determine turbulent boundary layer characteristics.

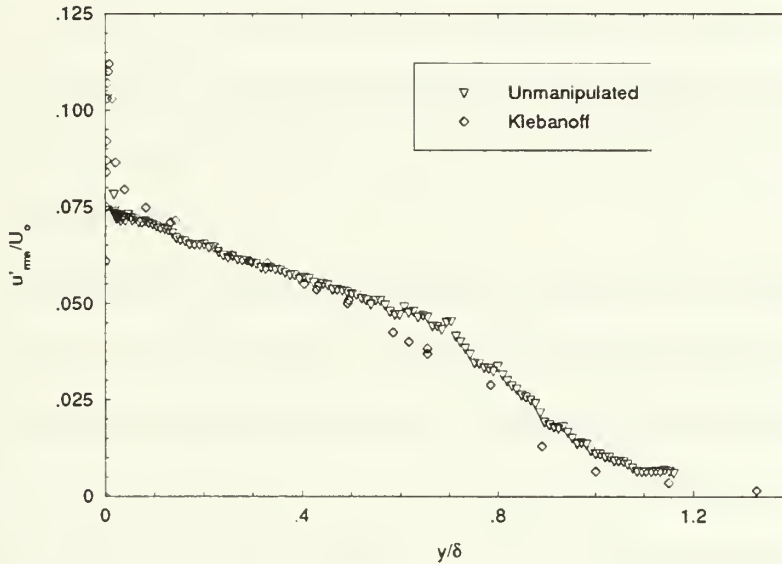


Figure 3.7(b) $\frac{\sqrt{u'^2}}{U_\infty}$ vs $\frac{y}{\delta}$ (Unmanipulated, $U_\infty=19$ m/sec)

Similarly, the profile for $\sqrt{v'^2}$ compares favorably with historical data (Figure 3.7(c)). Of interest, however, is the large near-wall discrepancy in the values of $\sqrt{v'^2}$.

Although not relevant to the specific objectives set forth, the near-wall deviation between the current measurement of $\sqrt{v'^2}$ and the historical data is discussed to reinforce issues raised previously regarding heat transfer effects with hot-wire sensors near a wall. The TSI X-probe indicates a peaking of $\sqrt{v'^2}$ similar to that for $\sqrt{u'^2}$ obtained by Klebanoff and others. Use of a TSI X-probe with smaller sensors resulted in identical profiles for $\sqrt{v'^2}$ as those obtained with the TSI probe having larger sensors, as in Figure 3.7(c). The near wall measurements have already been deemed invalid below a y/δ of 0.03, but, unlike the data comparison for $\sqrt{u'^2}$, a dual sensor hot-wire configuration must be used to resolve $\sqrt{v'^2}$. Klebanoff's data was also obtained with X-probes and was subject to similar sources of error. Reasons for the near wall discrepancy in $\sqrt{v'^2}$ from that of Klebanoff include differences in wall material (plexiglass versus aluminum plate) and in type of sensor supports (TSI's curved bronze prongs versus Klebanoff's fine jeweler's broaches). These would produce different local heat transfer effects which ultimately are reflected as velocity errors.

Voltage measurements of the X-probe sensors, as the probe was stepped away from the plexiglass wall in a no-flow condition, indicated an exponential-like drop in voltage from the wall surface to a distance where the lower sensor supports were 0.030 inches above the wall surface; the voltages of each sensor stabilized beyond this distance and differed from the wall value by approximately 0.07 volts. Such a procedure was not conducted above an aluminum surface but should be accomplished for comparison and to determine the validity of earlier measurements. The small voltage changes observed in the no-flow condition as the wall is approached have the greatest influence on the value of the instantaneous vertical velocity component, *if the effect persists under flow conditions*. If radiative heat transfer is the dominant mechanism responsible for the voltage changes observed, then voltage errors are introduced into the flow measurements

out to a distance from the wall of 0.030 inches. Radiation from a hot-wire probe to a nearby surface has been found a significant heat transfer mechanism [30]. This phenomenon could explain the sharp rise in $\sqrt{v'^2}$ near the wall.

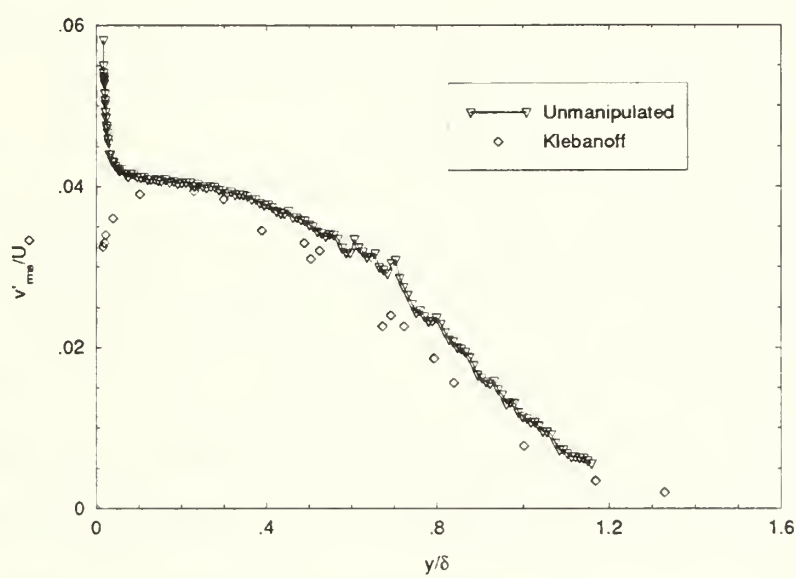


Figure 3.7(c) $\frac{\sqrt{v'^2}}{U_\infty}$ vs $\frac{y}{\delta}$ (Unmanipulated, $U_\infty=19$ m/sec)

In summary, the unmanipulated velocity profiles obtained in the wind tunnel at free stream speeds of 15, 19, and 23 meters per second indicate the existence of an equilibrium turbulent boundary layer parametrically equivalent to the turbulent boundary layer found above a flat plate over a similar range of Reynolds numbers based on length along the plate in the stream direction.

3.2.2 Manipulated Velocity Profiles

Interesting phenomena are observed in comparing the manipulated profiles to the unmanipulated profile as both height and upstream position of the BLM are varied. Figure 3.8(a) shows a well-defined mean stream flow structure exiting the downstream

end of the BLM. The 10-11 holes from the bottom to top of the manipulator are clearly discernable as the profile undergoes rapid oscillations due to the honeycomb hole structure. The profile is noticeably suppressed in magnitude up to a distance from the wall approximately that of the manipulator height. The same trends persist farther downstream from the BLM as shown in Figure 3.8(b) except that the flow structure has recovered to a more normal form, albeit still suppressed. Also, the 5.1 centimeter manipulator height is revealed by the form of the profile. Progressing still farther downstream (i.e. manipulator is positioned farther upstream from the measurement position), the profile acquires a different form, first indicated in Figure 3.8(d) where x_{BLM} equals 65 centimeters. Stream speed appears to increase linearly with height above the wall from a position very close to the wall to the height corresponding to the approximate boundary layer thickness where $\bar{u} \approx U_{\infty}$. At even greater distances downstream from the BLM, as in Figures 3.8(e) and 3.8(f), the approximately linear profile form endures.

A noticeable deviation in U_{∞} between the manipulated and unmanipulated measurements occurs when x_{BLM} is 65 centimeters. Since the manipulator both increases the drag of the test section and decreases local wall friction by its presence, the net drag change of the test section was estimated to be negligibly small. The estimate was based on the work of Hanson who determined that the test section only contributed 16% to the overall drag of the wind tunnel [10]. Thus, wind tunnel blower motor RPM was selected as an appropriate means of establishing the mean free stream velocity in the test section since the blower would not experience any appreciable loading due to the presence of the manipulator. The discrepancy in mean free stream velocity, then, is not attributed to any influence of the BLM but rather to acquiring data with the X-probe when the largest acceptable temperature difference ($\pm 3^{\circ}\text{F}$) between calibration and measurement occurred.

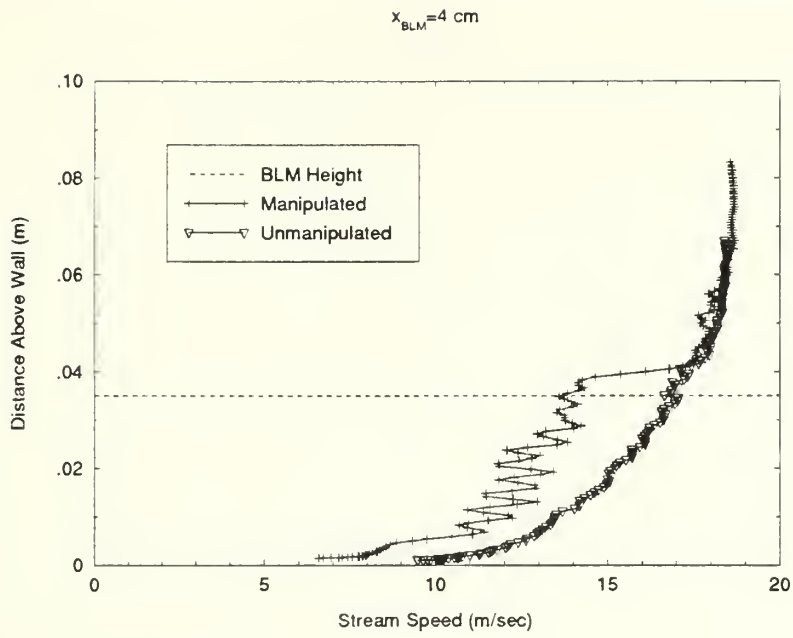


Figure 3.8(a) Velocity Profile Comparison ($U_\infty=19 \text{ m/sec}$)

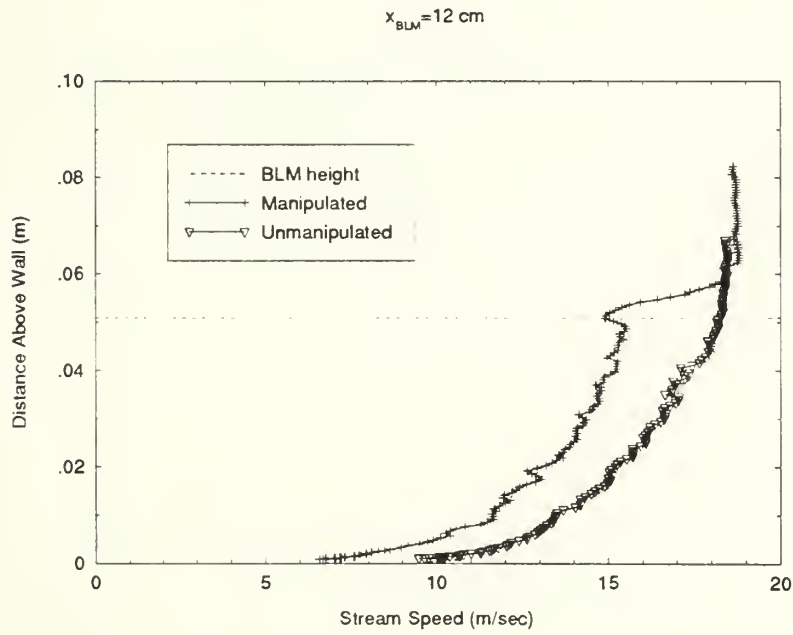


Figure 3.8(b) Velocity Profile Comparison ($U_\infty=19 \text{ m/sec}$)

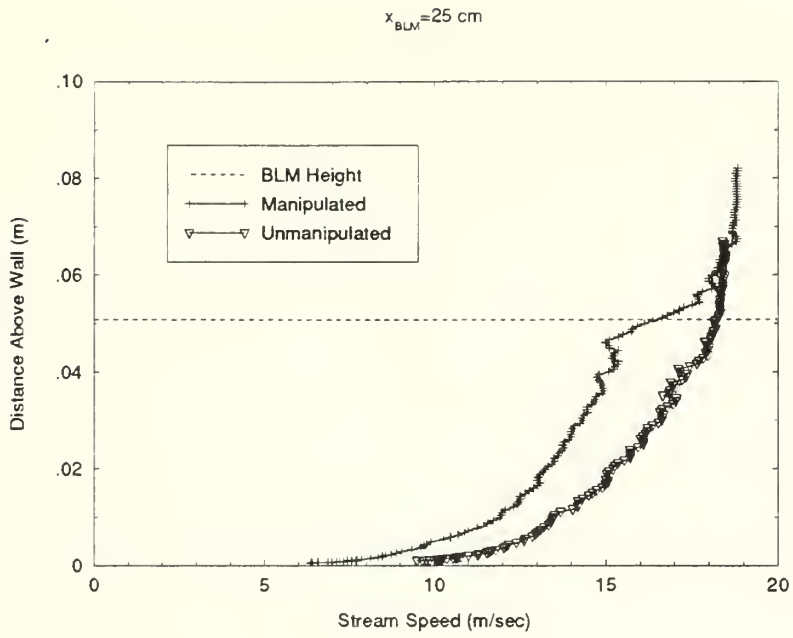


Figure 3.8(c) Velocity Profile Comparison ($U_{\infty}=19\text{ m/sec}$)

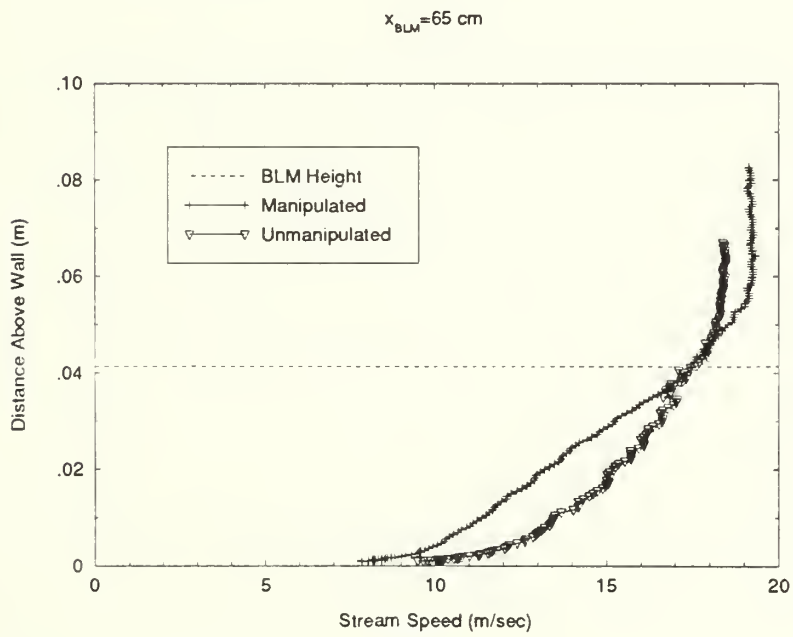


Figure 3.8(d) Velocity Profile Comparison ($U_{\infty}=19\text{ m/sec}$)

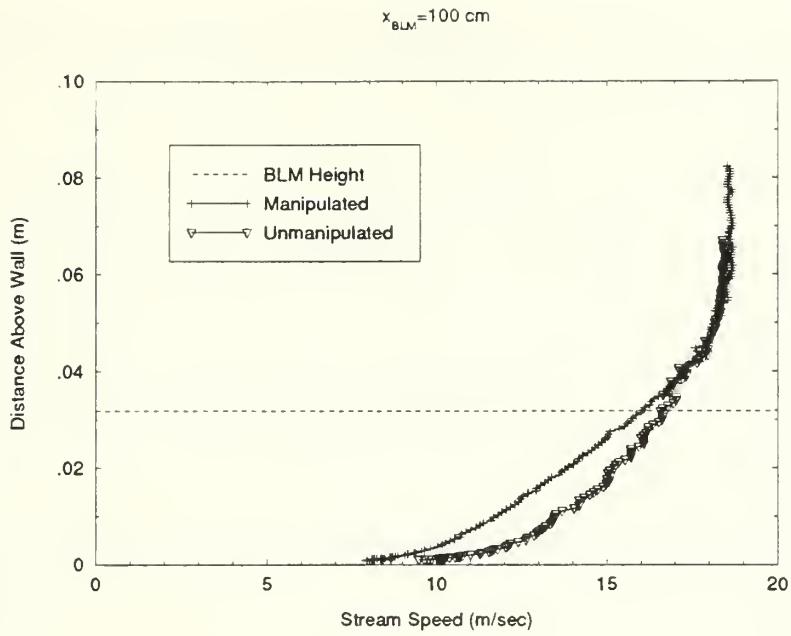


Figure 3.8(e) Velocity Profile Comparison ($U_{\infty} = 19 \text{ m/sec}$)

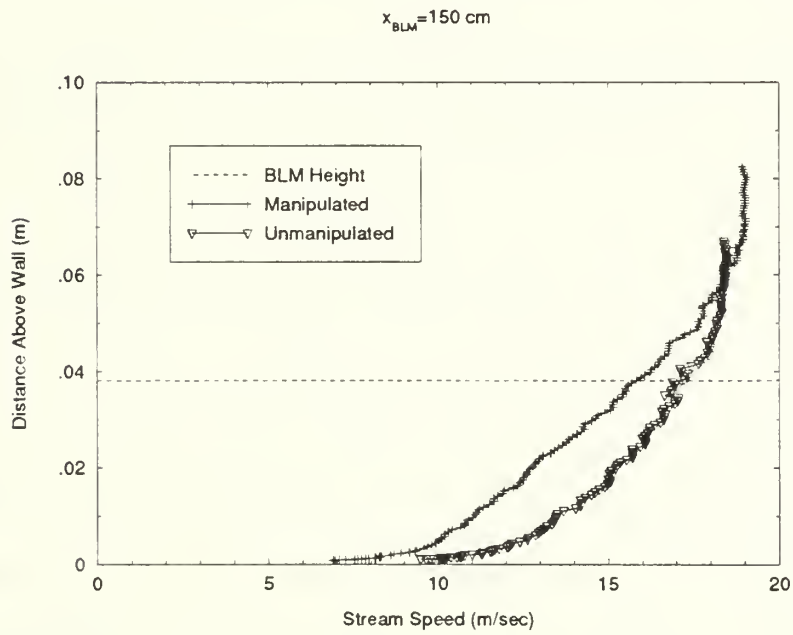


Figure 3.8(f) Velocity Profile Comparison ($U_{\infty} = 19 \text{ m/sec}$)

A significant yet unexpected finding during the boundary layer measurements was the influence of the manipulator on the mean vertical velocity. Fortunately, the calibration technique selected for the X-probe permitted the determination of this parameter. In an unmanipulated boundary layer $\bar{v} \ll \bar{u}$, and measurement of \bar{v} with an X-probe calibrated with the velocity-angle-voltage procedure readily confirms this fact. In fact, misalignment of the probe in an unmanipulated flow can be detected by a value of \bar{v} exceeding approximately 1% of the free stream speed. Fluid loading on the probe sensors and supports will introduce a small bias into the measurement resulting in slightly positive values of \bar{v} .

A typical vertical velocity profile for an *unmanipulated* layer appears in Figure 3.9(e), which is in fact a measurement for the manipulated profile 150 centimeters downstream of the manipulator where the flow has essentially recovered equilibrium. Positive velocity indicates velocity away from and normal to the wall. The profile is essentially restored to its unmanipulated form, a straight line where $\bar{v} \approx 0$. (The near-wall measurements are to be ignored for reasons outlined previously). Moving progressively towards the manipulator, the vertical velocity field becomes increasingly disturbed as indicated in Figures 3.9 (d), (c), (b), and (a). Immediately downstream of the manipulator the mean vertical velocity field oscillates. Shown well by Figure 3.9(a) also is a small positive mean vertical flow near the outer edge of the boundary layer seemingly originating near the top of the 3.5 centimeter manipulator. A similar but less pronounced profile pattern occurs above the 5.1 centimeter manipulator further downstream (Figure 3.9(b)). A large streamwise mean velocity component must be added to this vertical component to depict the resultant mean velocity flow structure.

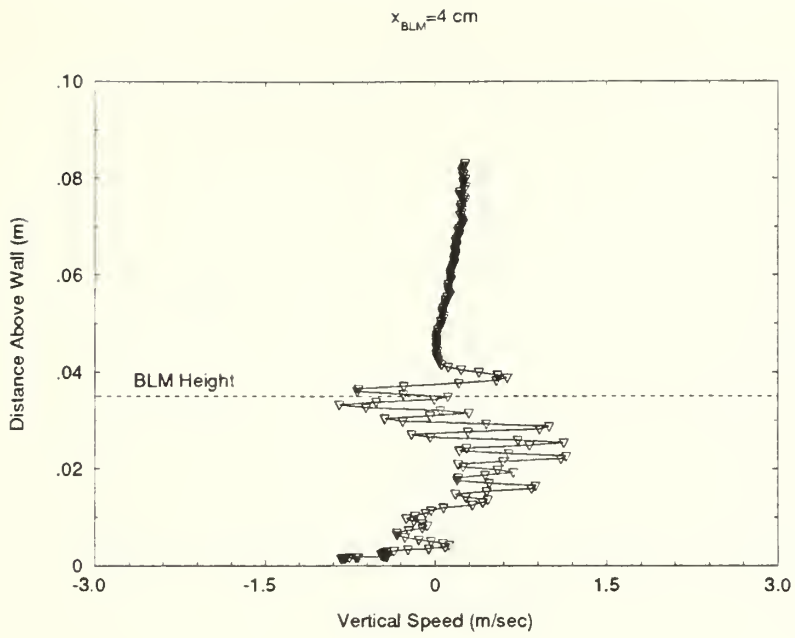


Figure 3.9(a) Vertical Velocity Profile ($U_{\infty} = 19 \text{ m/sec}$)

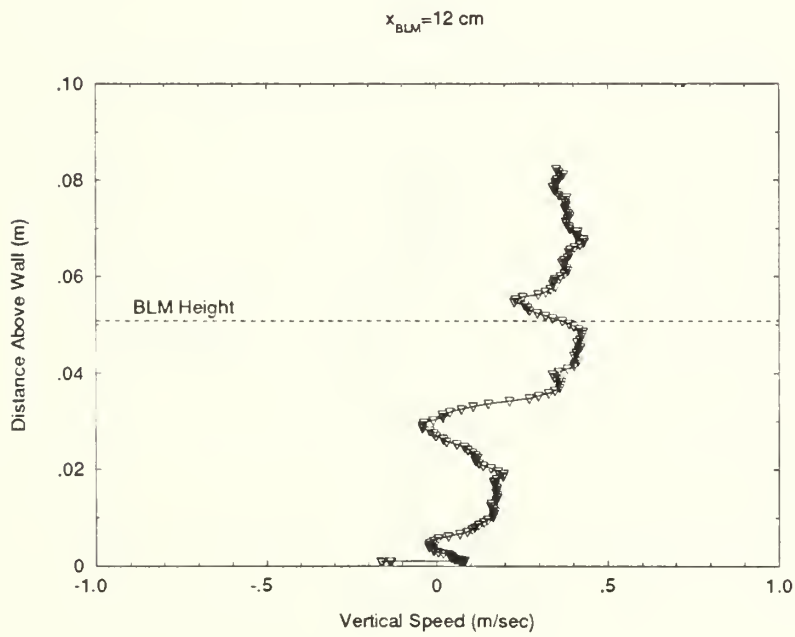


Figure 3.9(b) Vertical Velocity Profile ($U_{\infty} = 19 \text{ m/sec}$)

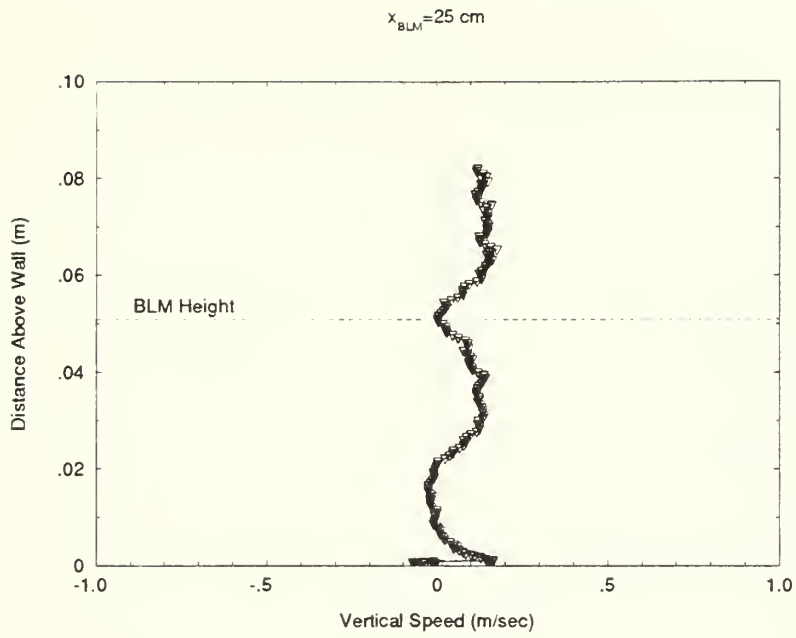


Figure 3.9(c) Vertical Velocity Profile ($U_{\infty}=19\text{ m/sec}$)

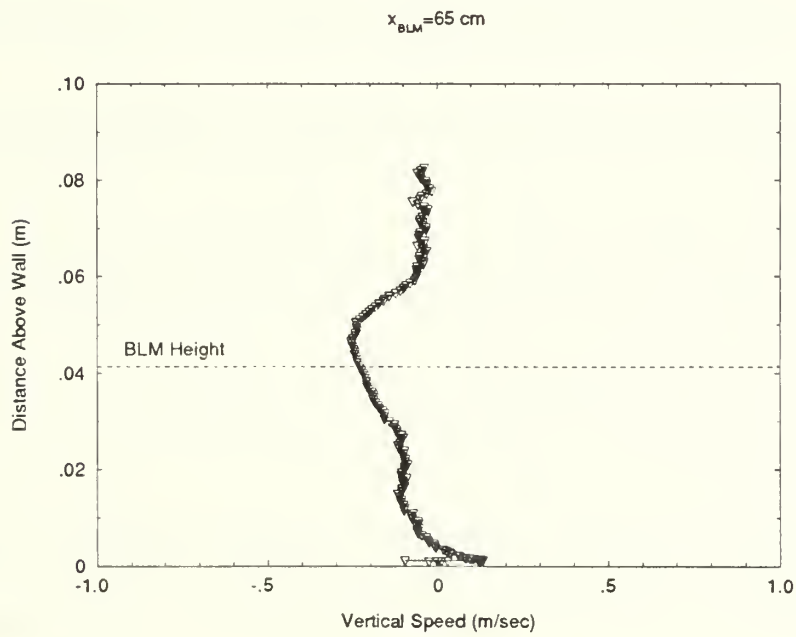


Figure 3.9(d) Vertical Velocity Profile ($U_{\infty}=19\text{ m/sec}$)

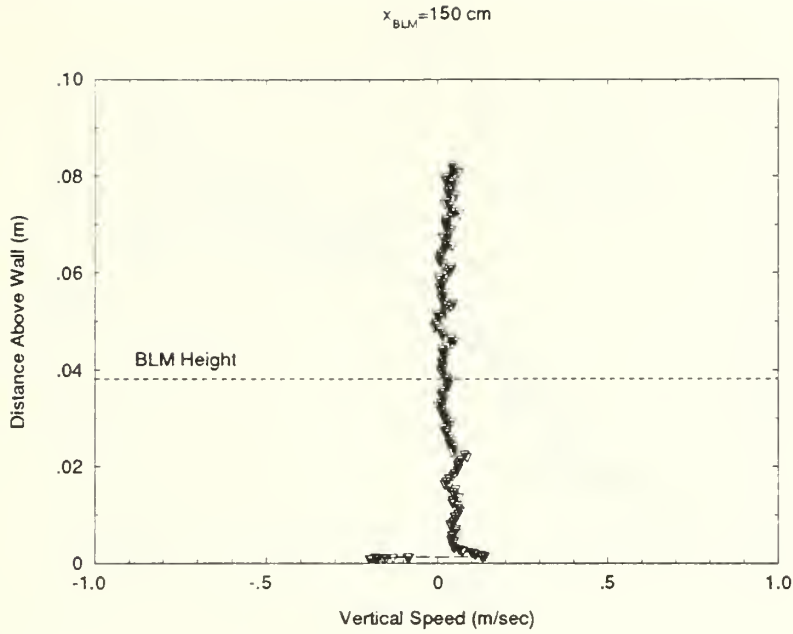


Figure 3.9(e) Vertical Velocity Profile ($U_{\infty}=19$ m/sec)

Manipulated boundary layer profiles for $\sqrt{u'^2}$, normalized with respect to the free stream speed, indicate a reduction of turbulent intensity in the near-wall region of the boundary layer extending outward a distance approximately the height of the individual BLM. Very near the BLM the strong influence of the manipulator structure is evident as $\sqrt{u'^2}$ varies rapidly with position (Figure 3.10(a)). As distance downstream from the manipulator increases, the rapid variation of $\sqrt{u'^2}$ dies out, and its value is some 25%-40% of the unmanipulated profile up to a distance from the wall approximating the manipulator height (Figures 3.10 (b) and (c)). Farther downstream the profile is restored in the outer portion of the boundary layer, but near the wall the $\sqrt{u'^2}$ profile remains essentially flat rather than increasing as the wall is approached.

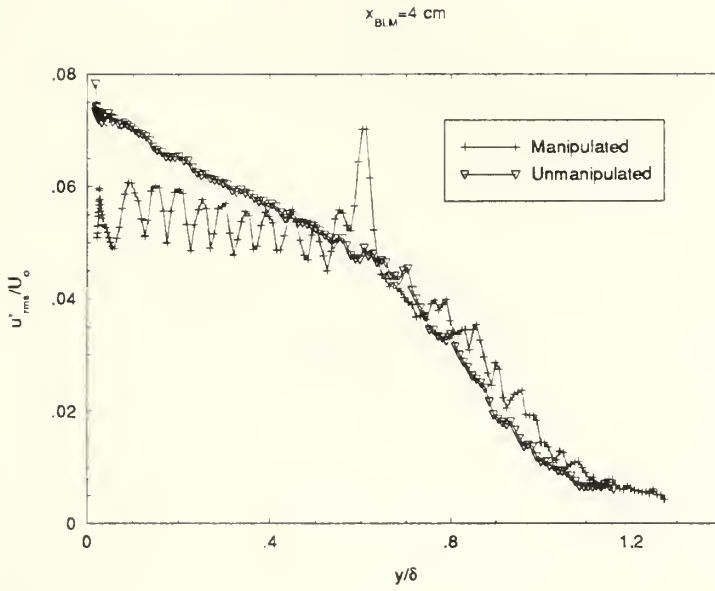


Figure 3.10(a) $\frac{\sqrt{u'^2}}{U_\infty}$ vs $\frac{y}{\delta}$ ($U_\infty=19 \text{ m/sec}$, $x_{BLM}=4 \text{ cm}$)

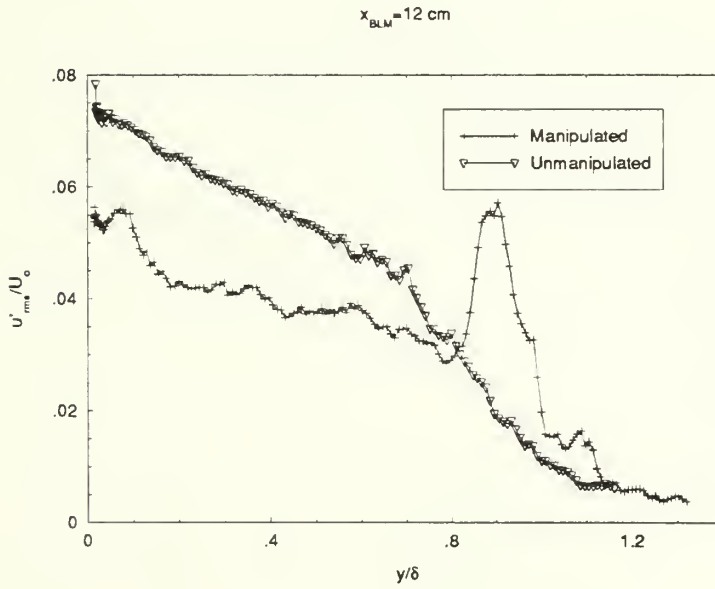


Figure 3.10(b) $\frac{\sqrt{u'^2}}{U_\infty}$ vs $\frac{y}{\delta}$ ($U_\infty=19 \text{ m/sec}$, $x_{BLM}=12 \text{ cm}$)

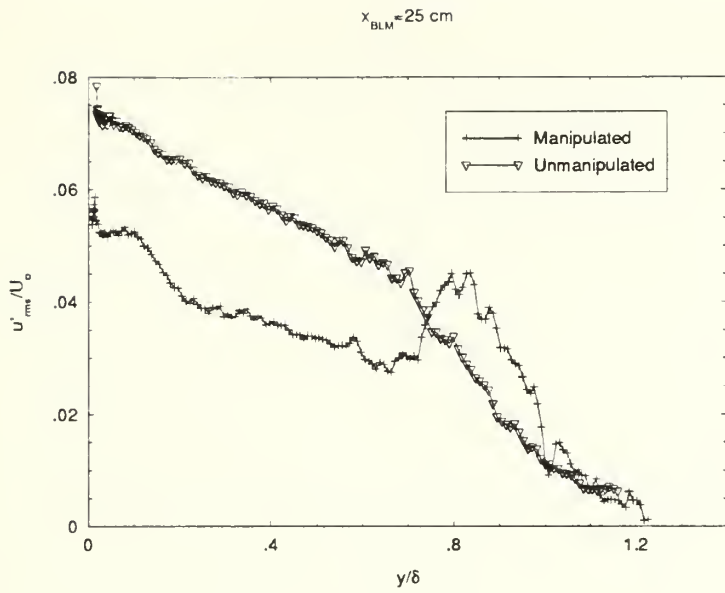


Figure 3.10(c) $\frac{\sqrt{u'^2}}{U_\infty}$ vs $\frac{y}{\delta}$ ($U_\infty=19 \text{ m/sec}$, $x_{BLM}=25 \text{ cm}$)

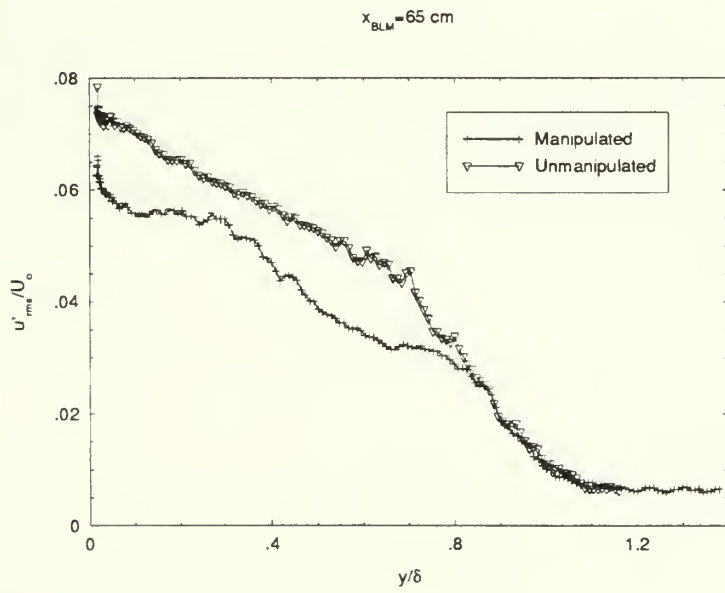


Figure 3.10(d) $\frac{\sqrt{u'^2}}{U_\infty}$ vs $\frac{y}{\delta}$ ($U_\infty=19 \text{ m/sec}$, $x_{BLM}=65 \text{ cm}$)

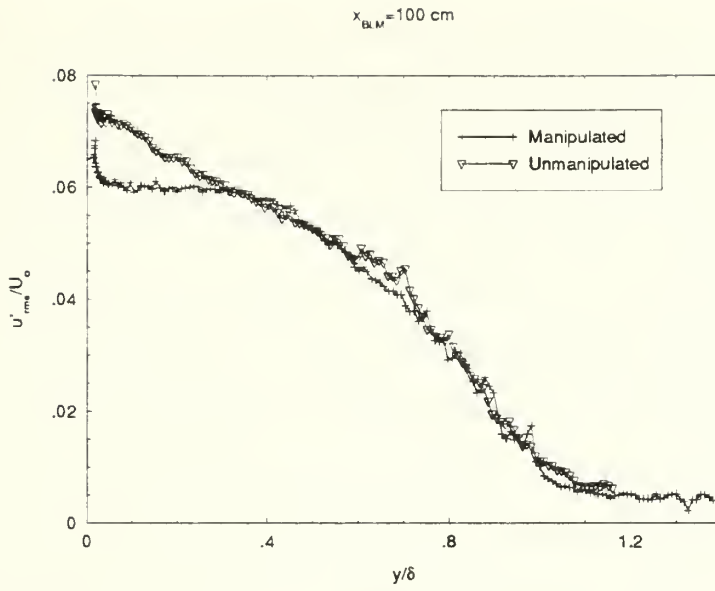


Figure 3.10(e) $\frac{\sqrt{u'^2}}{U_\infty}$ vs $\frac{y}{\delta}$ ($U_\infty=19 \text{ m/sec}$, $x_{BLM}=100 \text{ cm}$)

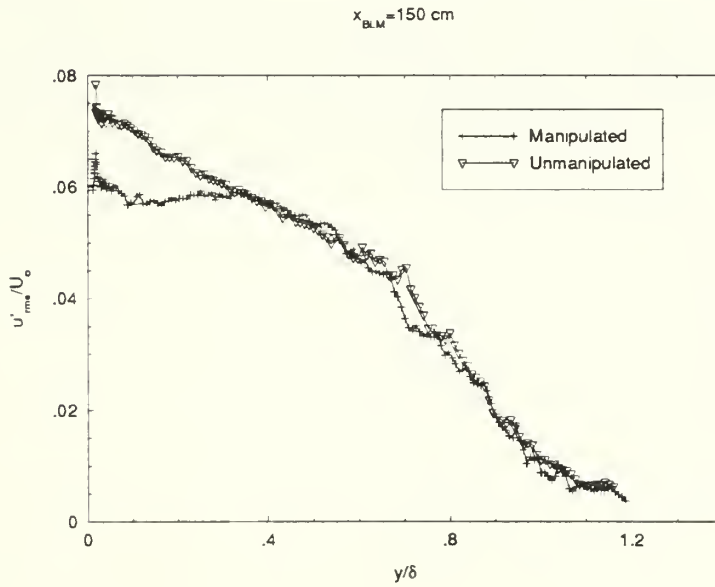


Figure 3.10(f) $\frac{\sqrt{u'^2}}{U_\infty}$ vs $\frac{y}{\delta}$ ($U_\infty=19 \text{ m/sec}$, $x_{BLM}=150 \text{ cm}$)

The effect of the manipulators on the rms vertical fluctuating velocity component follows a similar pattern to that of $\sqrt{u'^2}$ although the profile recovers more completely farther downstream. Near the manipulator the honeycomb structure dictates the profile as evidenced in Figure 3.11(a). The oscillating profile pattern, however, significantly exceeds the unmanipulated profile values of $\sqrt{v'^2}$. Figure 3.11(a) also indicates a suppression of the near-wall peak in $\sqrt{v'^2}$, approaching values near those of Klebanoff. Farther downstream of the manipulator the near-wall peaking in $\sqrt{v'^2}$ returns and persists (Figures 3.11 (b)-(f)). At intermediate distances downstream of the manipulator $\sqrt{v'^2}$ is reduced in magnitude by as much as 60% and remains essentially constant from a position where y/δ is approximately 0.2 to a distance above the wall where the strong shearing effects at the top of the manipulator begin to influence the profile (Figures 3.11 (b) and (c)). When a position 65 centimeters downstream of a BLM is reached, the profile in $\sqrt{v'^2}$ is partially restored to its unmanipulated form (Figure 3.11(d)). The recovery of $\sqrt{v'^2}$ (Figures 3.11 (e) and (f)) parallels that of $\sqrt{u'^2}$ at the same downstream measurement positions (Figures 10 (e) and (f)) in that values of $\sqrt{v'^2}$ are lower in the manipulated case out to a distance from the wall of $0.3y/\delta$.

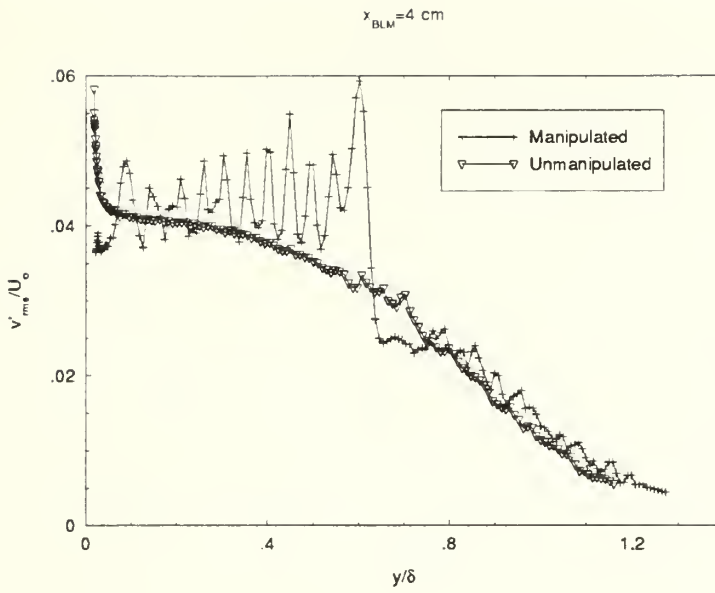


Figure 3.11(a) $\frac{\sqrt{v'^2}}{U_{\infty}}$ vs $\frac{y}{\delta}$ ($U_{\infty}=19 \text{ m/sec}, x_{BLM}=4 \text{ cm}$)

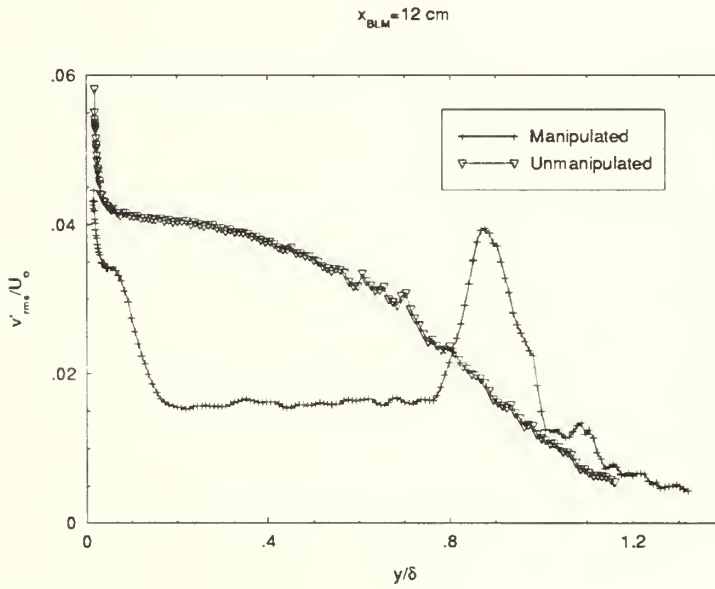


Figure 3.11(b) $\frac{\sqrt{v'^2}}{U_{\infty}}$ vs $\frac{y}{\delta}$ ($U_{\infty}=19 \text{ m/sec}, x_{BLM}=12 \text{ cm}$)

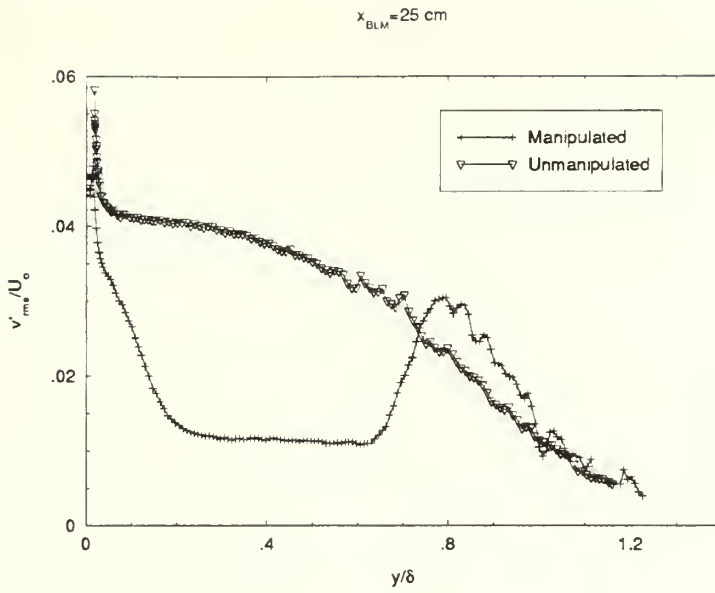


Figure 3.11(c) $\frac{\sqrt{v'^2}}{U_{\infty}}$ vs $\frac{y}{\delta}$ ($U_{\infty} = 19 \text{ m/sec}$, $x_{BLM} = 25 \text{ cm}$)

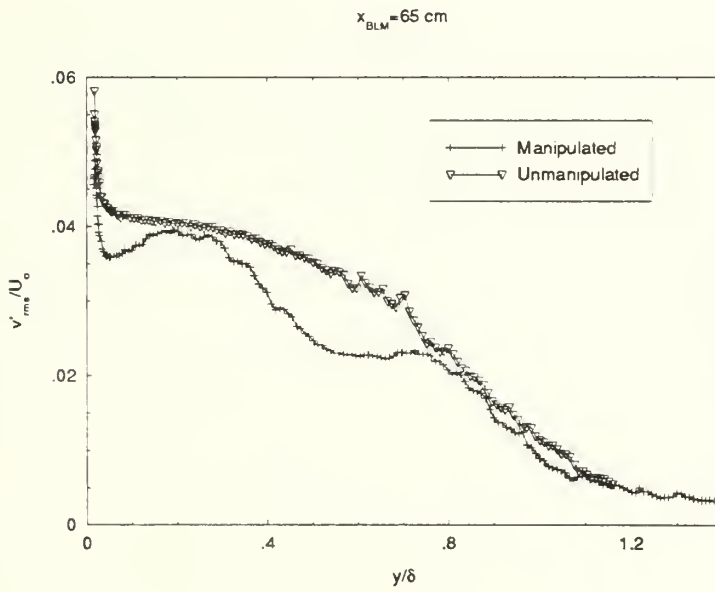


Figure 3.11(d) $\frac{\sqrt{v'^2}}{U_{\infty}}$ vs $\frac{y}{\delta}$ ($U_{\infty} = 19 \text{ m/sec}$, $x_{BLM} = 65 \text{ cm}$)

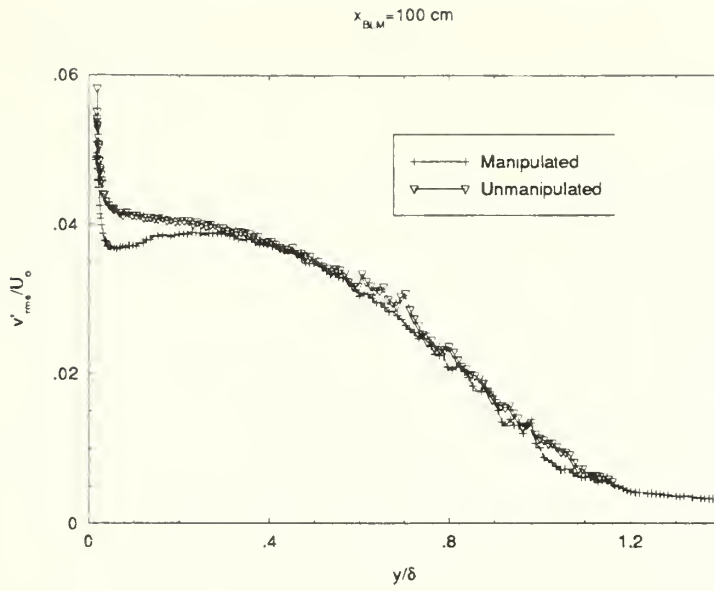


Figure 3.11(e) $\frac{\sqrt{v'^2}}{U_\infty}$ vs $\frac{y}{\delta}$ ($U_\infty = 19 \text{ m/sec}$, $x_{BLM} = 100 \text{ cm}$)

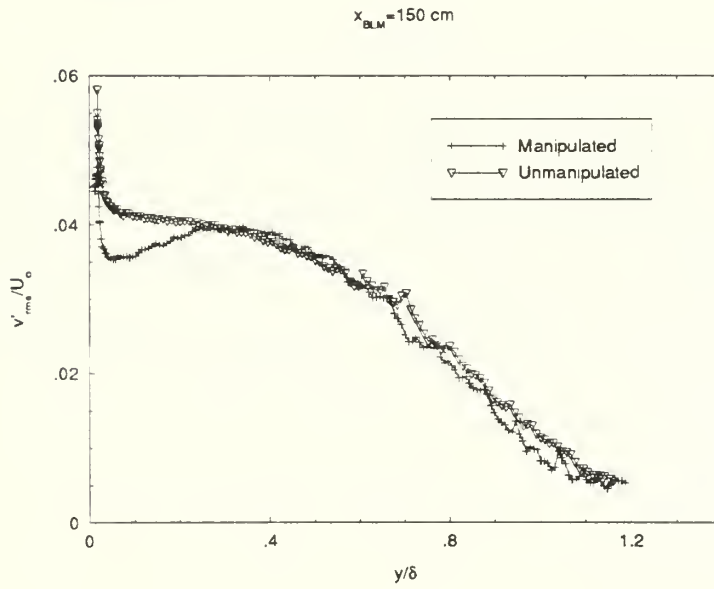


Figure 3.11(f) $\frac{\sqrt{v'^2}}{U_\infty}$ vs $\frac{y}{\delta}$ ($U_\infty = 19 \text{ m/sec}$, $x_{BLM} = 150 \text{ cm}$)

3.3 Stress Measurements

3.3.1 Wall Shear Stress

Wall shear stress for the manipulated boundary layers was measured directly by the calibrated surface differential pressure gauge. Calibration was based on eight data points determined from boundary layer profile data for free stream speeds ranging from 7-35 meters per second. By applying the Coles law of the wall fitting routine for each of eight mean stream velocity profiles, friction velocity and wall shear stress were determined. Wall shear stress was then related to the corresponding pressure drop across the gauge measured at the fence for each measurement speed. The calibration was accomplished over a range of h^+ from 1.02 to 3.74. Figures 3.12 (a) and (b) provide two separate representations of the calibration relationship. A linear least squares fit of the $\log_{10}(\tau_w)$ and $\log_{10}(\Delta P)$ calibration data resulted in a calibration curve represented by Equation (3.10) and plotted in Figure 3.12(a).

$$\tau_w = .28\Delta P^{0.63} \quad (3.10)$$

Equation (3.10) for τ_w agrees well with the findings of Gur and Leehey using a similar gauge. An alternate formulation of the relationship between wall shear stress and pressure drop across the surface gauge in terms of h^+ is provided by Figure 3.12(b). For a given fence height and fluid, the formulations are equivalent.

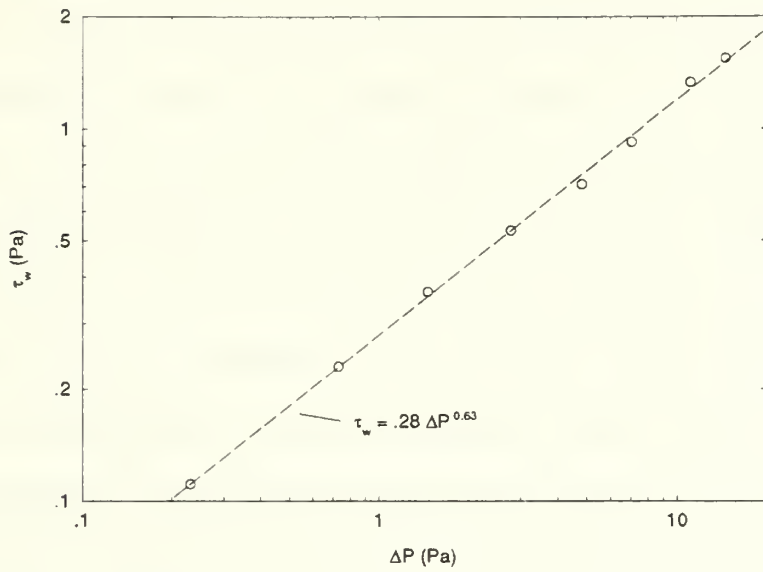


Figure 3.12(a) Surface Fence Calibration (ΔP vs τ_w)

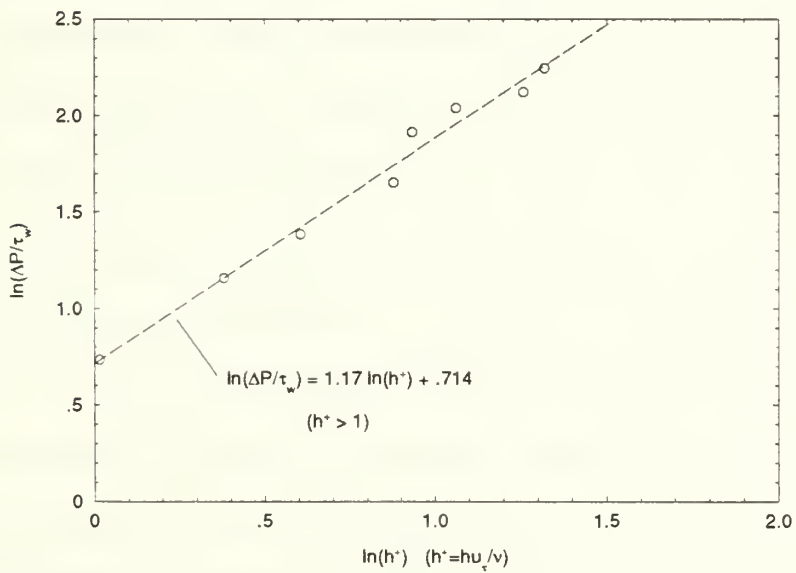


Figure 3.12(b) Surface Fence Calibration - Alternate Formulation ($\ln(\Delta P / \tau_w)$ vs $\ln(h^+)$)

3.3.2 Reynolds Stress

The most significant influence of the honeycomb manipulators appears in the Reynolds stress profiles normalized to the square of the friction velocity (Figures 3.13 (a) - (f)). The friction velocity was obtained from surface fence measurements at the same position downstream of the BLM where each profile was measured. The profile four centimeters downstream of the manipulator (Figure 3.13(a)) dramatically shows the Reynolds stress term obtaining a negative value (i.e. $\overline{u'v'} > 0$), a phenomenon never occurring within an unmanipulated equilibrium turbulent boundary layer. Two phenomena characterize the peaking pattern exiting the manipulator. First is the distinct influence of each row of manipulator holes on the local Reynolds stress, specifically the oscillating pattern observed in the velocity profiles. Second is the combined influence of all rows of holes, such that superimposed upon the oscillating Reynolds stress pattern is a curvature resulting in the largest positive values of $\overline{u'v'}$ at approximately the mid-height of the manipulator (shown by the large negative peaks in $\frac{-\overline{u'v'}}{u_\tau^2}$ near the manipulator mid-height in Figure 3.13(a)). The negative peaks in $\frac{-\overline{u'v'}}{u_\tau^2}$ tend to decrease in magnitude at measurement positions away from the mid-height toward the top and base of the BLM.

Farther downstream the Reynolds stress becomes positive again (i.e. $\overline{u'v'} < 0$) but is greatly reduced in magnitude over a depth of the boundary layer corresponding to a major fraction of the manipulator height (Figures 3.13 (b) and (c)). (Westphal apparently found a similar reduction in Reynolds stresses near the flat plate manipulators used in his experiments but provided no graphical representations of such [7].) The individual manifestations of stresses induced by flow through the honeycomb structure have merged due to diffusion processes. Likewise, the diffusion of the strong shearing influence of the flow over the top boundary of the manipulator is clearly evident as the fractional width of this region with respect to the total boundary layer height has increased.

Still farther downstream the Reynolds stress profile shows signs of restoration to an unmanipulated boundary layer form but takes on two distinct characteristics. The first is a minor suppression near the wall; the second is a mid-layer peaking the same distances from the wall where farther upstream the profile was greatly suppressed (Figures 3.13 (d) - (f)). As mentioned previously, Westphal found similar mid-layer peaking far downstream from single and tandem flat plate manipulators [7]. Westphal's profiles lack the fine point-to-point measurement detail of the present work, and suppression of the Reynolds stress as the wall is approached is not evident at his downstream measurement locations.

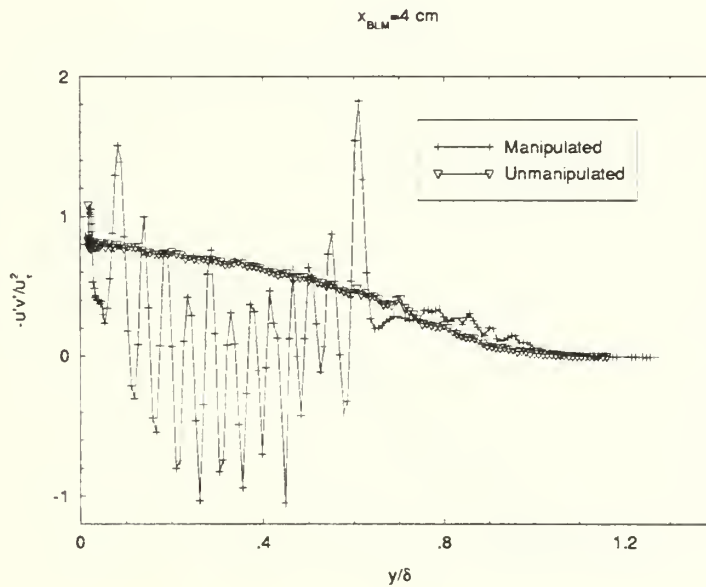


Figure 3.13(a) $\frac{-\overline{u'v'}}{u_\tau^2}$ vs $\frac{y}{\delta}$ ($U_\infty=19$ m/sec)

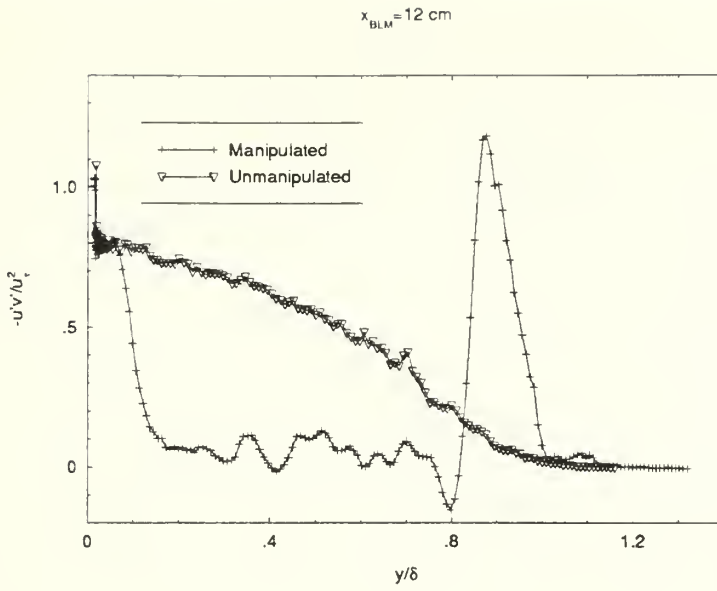


Figure 3.13(b) $\frac{-\overline{u'v'}}{\mu_\tau^2}$ vs $\frac{y}{\delta}$ ($U_\infty = 19 \text{ m/sec}$)

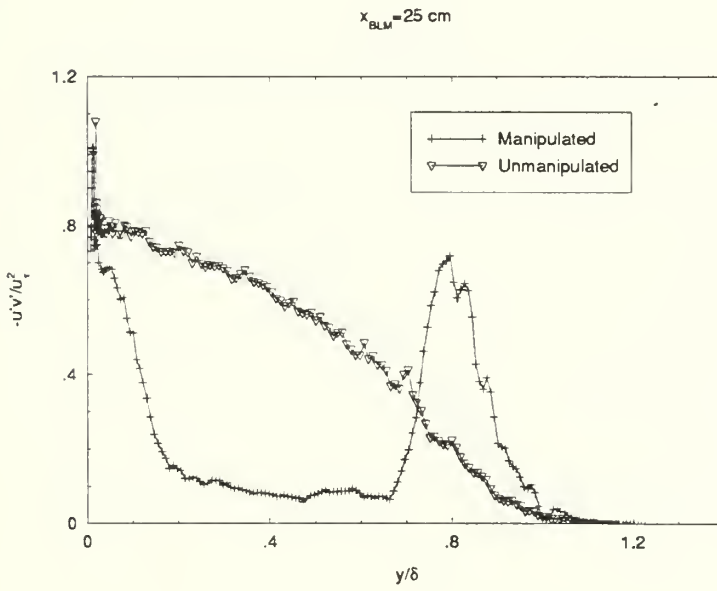


Figure 3.13(c) $\frac{-\overline{u'v'}}{\mu_\tau^2}$ vs $\frac{y}{\delta}$ ($U_\infty = 19 \text{ m/sec}$)

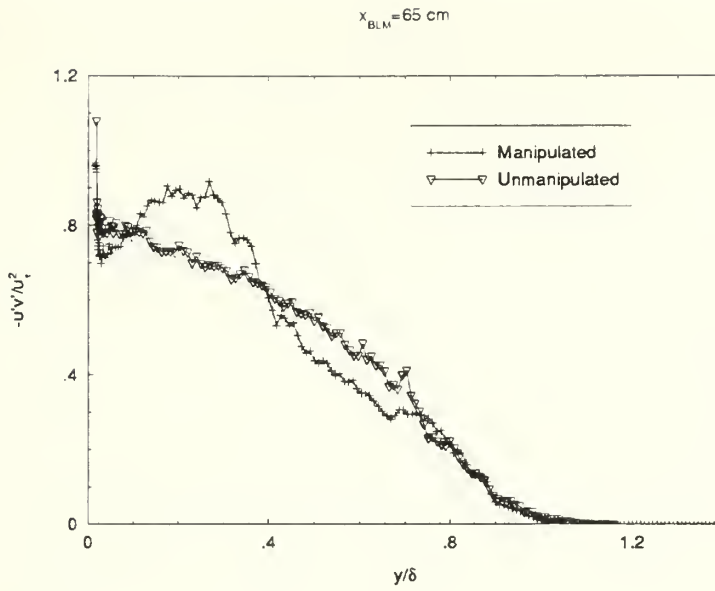


Figure 3.13(d) $\frac{-\overline{u'v'}}{\mu_\tau^2}$ vs $\frac{y}{\delta}$ ($U_\infty = 19 \text{ m/sec}$)

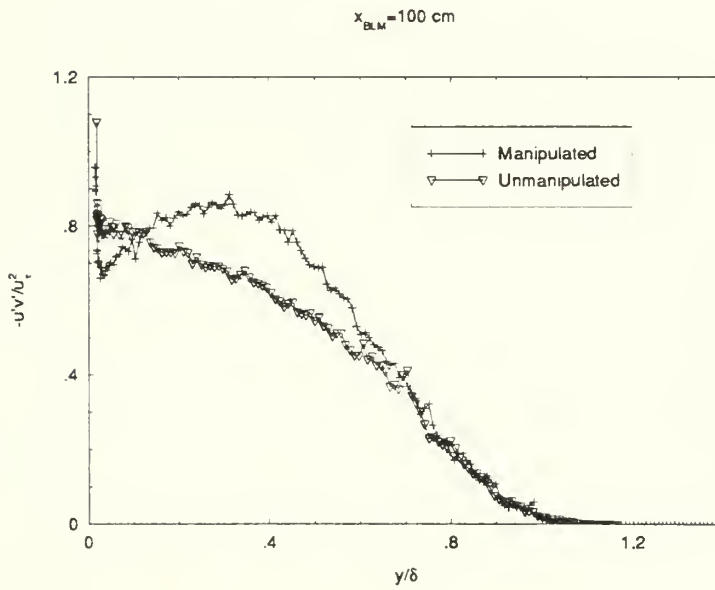


Figure 3.13(e) $\frac{-\overline{u'v'}}{\mu_\tau^2}$ vs $\frac{y}{\delta}$ ($U_\infty = 19 \text{ m/sec}$)

$x_{B.M.} = 150 \text{ cm}$

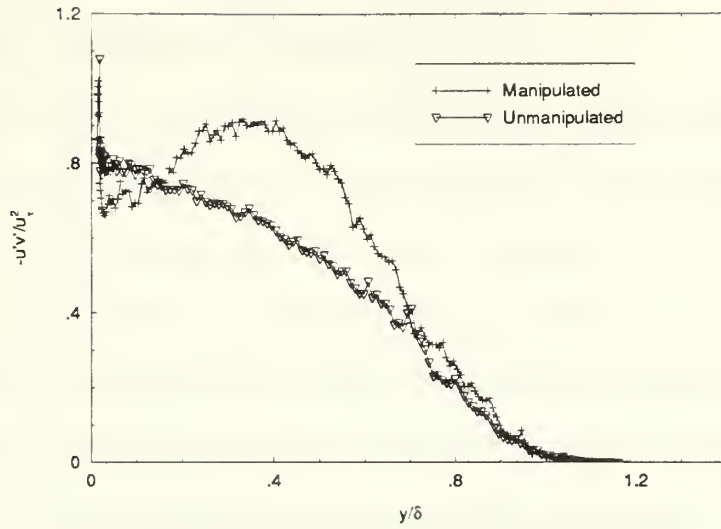


Figure 3.13(f) $\frac{-\overline{u'v'}}{u_\tau^2}$ vs $\frac{y}{\delta}$ ($U_\infty = 19 \text{ m/sec}$)

4 Discussion of Results

4.1 Manipulator Influence on Velocity Profiles

In Section 3.2.2 the manipulated mean and fluctuating velocity profiles were individually described. In this section a more comprehensive view of the data is forwarded which integrates these individual results. The mean velocity profiles in the stream direction generally adhere to expectations based on the use of a honeycomb-structured manipulator (see Section 2.4). All near-manipulator profiles indicate that energy has been extracted from the mean flow and that the scale of the flow has been reduced. Farther downstream, dispersion results in a the loss of local flow identity, and the mean flow energy is gradually restored due to diffusion from the outer regions of the boundary layer to the inner. Full restoration of the mean velocity profile in the stream direction was not observed at the farthest measurement position ($x_{BLM}=150$ cm). The mean vertical velocity profiles are best explained by considering the influence of the manipulator channels on the flow at different channel levels of the manipulator. A horizontal flow in principle should exit these channels but due to the different incident velocities at the different channel levels and due to minor manufacturing differences of the channels an irregular vertical pressure distribution will exist at the manipulator channel exits. The pressure differences will introduce a small vertical velocity component onto the mean flow which quickly dissipates farther downstream.

The same general trends discussed for the mean velocity profiles applies to the fluctuating components. Strong variations in the magnitude of the rms fluctuating stream and vertical velocities near the manipulator, indicative of the honeycomb cell structure, diffuse and superpose to reduce sharply the magnitude of the these velocities throughout a major fraction of the boundary layer thickness. The mechanisms responsible for these effects and the partial recovery of the profile to an unmanipulated form are explored in

the next sub-section. It is more instructive to examine the results of the present measurements in comparison to similar measurements with honeycomb manipulators placed in a free stream. Particular attention is given to the fluctuating stream component. The works of Lumley and McMahon [26], Loerhke and Nagib [27], and Batchelor [28] provide the bases of comparison.

Due to the great differences in the flow structure incident upon a honeycomb manipulator occupying the cross-section of a flow channel from that of a manipulator placed within a boundary layer, direct comparison of mean and fluctuating velocity profiles is not justified. Streamwise variation of these velocities is the primary focus when manipulating the free stream while both transverse and streamwise variations are of interest in manipulated boundary layers. What is of interest are the turbulent energy decay relationships for screens and grids, which have also been applied to free stream honeycomb manipulators. Batchelor specifies an initial decay relationship for the turbulence exiting a free stream manipulator or grid such that $\overline{u'^2} \propto (x - x_0)^{-1}$, where x_0 is a virtual origin approximately equal to ten times the honeycomb cell diameter [28]. In general, the relationship applies for approximately 100 cell diameters downstream of the manipulator, which is approximately 32 centimeters for the present measurements. With measurements in the manipulated boundary layer at 4, 12, and 25 centimeters downstream of the BLM, no such decay behavior could be found. Manipulated boundary layer energy decay in $\overline{u'^2}$ occurs more gradually and levels off in the region 12 centimeters downstream of the manipulator. If the peak value of Reynolds stress at four centimeters from the manipulator is compared to the mid-layer value at 12 centimeters, the decay is comparable to that found for grids, but between 12 and 25 centimeters, the relationship is invalid. Also, the turbulent energy decay still farther downstream of grids varies as $x^{-5/2}$ [26]. This is not observed for boundary layer honeycomb manipulators, and the turbulence levels rise gradually to levels observed in unmanipulated boundary layers

at the far downstream locations. In summary, turbulent energy decay relationships and velocity variations in the stream direction for grids and free stream honeycomb manipulators have little bearing on the present investigation of turbulent boundary layer honeycomb manipulators, particularly in understanding energy transport phenomenon.

4.2 Manipulator Influence on Measured Stresses

The friction coefficient (C_f) provides a measure of the wall shear stress. By relating the friction coefficient in the manipulated boundary layer, at a specific free stream speed and location relative to the boundary layer's virtual origin, to the friction coefficient of the unmanipulated boundary layer at the same free stream speed and location, the influence of the manipulator on wall shear stress is quantified. As the manipulator's position upstream of the measurement location is varied, the streamwise influence of the manipulator upon wall shear stress is determined. Figure 4.1 summarizes manipulator influence on wall shear stress as a result of varying not only free stream speed and manipulator location in the boundary layer, but also manipulator height. The ratio between the manipulated and unmanipulated friction coefficients is plotted as BLM height and upstream distance from the measurement location are varied, both of which are normalized to the displacement thickness of the unmanipulated boundary layer at the location of the BLM. In Figure 4.1 d^* represents δ_{und}^* , and x_{BLM} has been multiplied by 0.01 to improve overall plot scaling.

As shown by Figure 4.1, a 35%-40% reduction in the friction coefficient is evident just downstream of the manipulator; this reduction is relatively insensitive to changes in manipulator height. As distance downstream from the manipulator increases, the friction coefficient ratio becomes relatively constant beyond 150 displacement thicknesses for the approximate range $4 < \frac{h_{BLM}}{\delta_{und}^*} < 5$. Roth and Leehey found the same trend in the behavior of the friction coefficient ratio for a one-eighth-inch-cell honeycomb manipulator

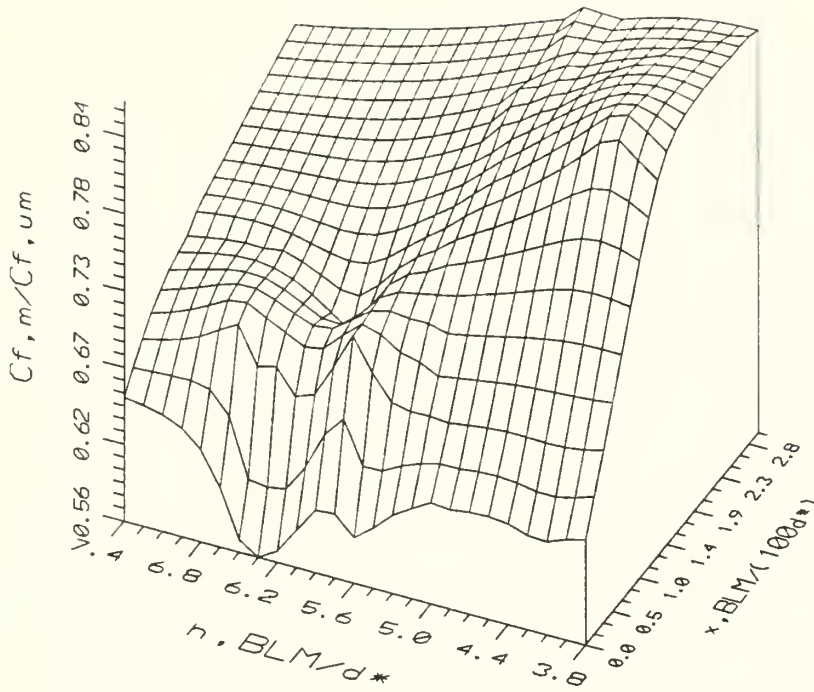


Figure 4.1 Friction Coefficient Ratio

approximately 1.3 inches in height [6]. As the height-to-displacement thickness of the manipulator increases, the friction coefficient ratio slopes upward toward a value of unity at far downstream locations. A depression in the friction coefficient ratio is observed in the range $6.0 < \frac{h_{BLM}}{\delta_{und}^*} < 6.5$ out to a distance downstream of $100 \delta_{und}^*$. By referring to Tables 3.1 through 3.4, the depression is determined to occur when the free stream speed is 19 meters per second and when $25cm < x_{BLM} < 65cm$ and $4cm < h_{BLM} < 5cm$. The small number of data points used in developing Figure 4.1 makes discussion of the causes of this surface feature premature; it is also premature to draw conclusions regarding optimization of parameters. The matter warrants further detailed investigation.

By examining the Reynolds stress profiles at all measurement speeds and the friction coefficient ratio plot at measurement positions close to the manipulator, a reduction in the magnitude of the friction coefficient between the manipulated and unmanipulated boundary layers occurs in conjunction with a reduction of the Reynolds

stresses in the boundary layer, excepting the large shearing peak from the top of the manipulator. Simply stated, closest to the manipulator the Reynolds stresses are least and so is the wall shear stress. It may be surmised then that a reduction in the Reynolds stress levels in the boundary layer will decrease the transport of turbulent energy toward the wall, which in turn reduces the wall shear stress or friction coefficient. This view is overly simplistic and cannot be accepted at measurement positions farther downstream where the Reynolds stress distribution obtains an enhanced structure in the mid-layer (see e.g. Figures 3.13 (d) - (f)). Westphal was concerned with this phenomenon and suggested that a net reduction in skin friction, using the flat plate type manipulator, may be minimal due to the rapid recovery of the Reynolds stresses through the diffusion process [7]. The fact that the coefficient of friction ratio is still significantly less than one ($\frac{C_{f,m}}{C_{f,um}} \approx 0.8$) even at downstream positions where the Reynolds stress profile is enhanced indicates other mechanisms are at work.

A physical description of how the honeycomb manipulator influences the flow structure of the boundary layer is best obtained by examining the equations for the mean and turbulent kinetic energies. Such equations are specified or may be extracted from analyses found in the works of Hinze [29] and Townsend [8]. The framework for understanding manipulated flow is established by applying these equations to the unmanipulated turbulent boundary layer.

The mean kinetic energy equation in standard tensor notation, neglecting thermal and gravitational effects, is given by Equation (4.1).

$$\frac{1}{2} \frac{\partial (\overline{u_i})^2}{\partial t} + \frac{1}{2} \overline{u_j} \frac{\partial (\overline{u_i})^2}{\partial x_j} = - \frac{\partial \{(\overline{p})(\overline{u_j})\}}{\partial x_j} - \overline{u_i} \frac{\partial \overline{u'_i u'_j}}{\partial x_j} + \nu \overline{u_i} \frac{\partial^2 \overline{u_i}}{\partial x_j^2} \quad (4.1)$$

For steady-state conditions ($\frac{\partial}{\partial t} = 0$) and recognizing the *continuity* relationship ($\frac{\partial \overline{u_i}}{\partial x_i} = 0$), the expression is simplified. Also, the Reynolds stress and viscous stress terms can be

combined to give the total stress,

$$\hat{\tau}_{ij} = \nu \frac{\partial \bar{u}_i}{\partial x_j} - \overline{u'_i u'_j} \quad . \quad (4.2)$$

For an unmanipulated boundary layer the Reynolds stress term is the dominant stress term except near the wall where $\frac{\partial \bar{u}}{\partial y}$ is large. The equation for mean kinetic energy reduces to

$$\bar{u}_j \frac{\partial}{\partial x_j} \frac{\bar{u}_i^2}{2} = -\bar{u}_j \frac{\partial \bar{p}}{\partial x_j} + \bar{u}_i \frac{\partial \hat{\tau}_{ij}}{\partial x_j} \quad . \quad (4.3)$$

If homogeneity in the cross-flow direction is assumed, $\bar{u}_3 = \bar{w} = 0$ and all $x_3 = z$ derivatives vanish. Then (4.3) becomes

$$\left(\bar{u} \frac{\partial}{\partial x} + \bar{v} \frac{\partial}{\partial y} \right) \left(\frac{\bar{u}^2}{2} + \frac{\bar{v}^2}{2} \right) = -\bar{u} \frac{\partial \bar{p}}{\partial x} - \bar{v} \frac{\partial \bar{p}}{\partial y} + \bar{u} \frac{\partial \hat{\tau}_{xx}}{\partial x} + \bar{u} \frac{\partial \hat{\tau}_{xy}}{\partial y} + \bar{v} \frac{\partial \hat{\tau}_{yx}}{\partial x} + \bar{v} \frac{\partial \hat{\tau}_{yy}}{\partial y} \quad . \quad (4.4)$$

By consideration of velocity and length scales, albeit with different approaches in neglecting product and derivative terms containing \bar{v} , Hinze and Townsend reduced the mean kinetic energy equation to

$$\left(\bar{u} \frac{\partial}{\partial x} + \bar{v} \frac{\partial}{\partial y} \right) \left(\frac{(\bar{u})^2}{2} + \frac{(\bar{v})^2}{2} \right) = -\bar{u} \frac{\partial \bar{p}}{\partial x} - \hat{\tau} \frac{\partial \bar{u}}{\partial y} + \frac{\partial \hat{\tau} \bar{u}}{\partial y} \quad , \quad (4.5)$$

where $\hat{\tau} = \hat{\tau}_{xy}$ [8,29]. The left-hand side of (4.5) represents the convection of the mean kinetic energy within the boundary layer. The pressure term on the right-hand side describes the work done by the imposed pressure gradient across the volume. The stress terms together equal $-\bar{u} \frac{\partial \hat{\tau}}{\partial y}$. Thus, energy supplied to the mean flow via wind tunnel blower differential pressure is transported primarily by the mean stream flow and transformed into mean kinetic energy and work done by the stress gradient normal to the wall. This latter effect is characterized by an inward transfer of stress energy ($\frac{\partial}{\partial y} (-\hat{\tau} \bar{u})$) toward the wall and conversion of mean flow energy to turbulent energy ($-\hat{\tau} \frac{\partial \bar{u}}{\partial y}$), primarily in the near wall sub-layer [9].

The effects of the blower in supplying energy to the mean flow are best understood by integrating the pressure term in the mean kinetic energy equation over a rectangular Cartesian volume element within the boundary layer, differentially expressed as $dx dy dz$. The original formulation of the pressure gradient as found in (4.1) can be used since negligible terms or terms eliminated by the continuity relationship will not survive the analysis. Thus, the energy supplied to an arbitrary rectangular volume within the boundary layer can be expressed by

$$\int_V \frac{\partial}{\partial x} \{(\bar{u})(\bar{p})\} dx dy dz = \int_{S_2} (\bar{u})(\bar{p}) dx dy - \int_{S_1} (\bar{u})(\bar{p}) dx dy \quad , \quad (4.6)$$

where S_1 and S_2 represent the upstream and downstream faces of the rectangular solid, respectively, and

$$\int_V \frac{\partial}{\partial y} \{(\bar{v})(\bar{p})\} dx dy dz = \int_{A_2} (\bar{v})(\bar{p}) dx dz - \int_{A_1} (\bar{v})(\bar{p}) dx dz \quad , \quad (4.7)$$

where A_1 and A_2 are the near and far surfaces, respectively, of the rectangular volume parallel to the wall. The integral in (4.7) vanishes for unmanipulated flow. In a like manner the other terms in (4.5) may be integrated.

The steady-state turbulent kinetic energy equation, neglecting thermal and gravitational variations, is given by

$$\bar{u}_j \frac{\partial}{\partial x_j} \left(\frac{1}{2} \overline{q^2} \right) + \frac{\partial}{\partial x_j} \left(\overline{p' u'_j} + \frac{1}{2} \overline{q^2 u'_j} \right) + \overline{u'_i u'_j} \frac{\partial \bar{u}_i}{\partial x_j} = \overline{v u'_i} \frac{\partial^2 u'_i}{\partial x_j^2} = -\epsilon_i \quad . \quad (4.8)$$

By applying the same approximations and scales, as done for the mean equation, to eliminate negligible terms, (4.8) becomes

$$\left(\bar{u} \frac{\partial}{\partial x} + \bar{v} \frac{\partial}{\partial y} \right) \left(\frac{1}{2} \overline{q^2} \right) + \frac{\partial}{\partial y} \left(\overline{p' u'} + \frac{1}{2} \overline{q^2 u'} \right) + \overline{u' v'} \frac{\partial \bar{u}}{\partial y} = -\epsilon_i \quad . \quad (4.9)$$

Since $\overline{u'v'} = -\hat{\tau} + v \frac{\partial \bar{u}}{\partial y}$, the mean and turbulent kinetic energy equations, (4.5) and (4.9) can be added to obtain

$$\left(\bar{u} \frac{\partial}{\partial x} + \bar{v} \frac{\partial}{\partial y} \right) \left(\frac{1}{2} \{ (\bar{u})^2 + (\bar{v})^2 + \overline{q^2} \} \right) + \frac{\partial}{\partial y} \left(\overline{p'u'} + \frac{1}{2} \overline{q^2 u'} \right) - \frac{\partial \hat{\tau} \bar{u}}{\partial y} + \epsilon_t + \epsilon_m = -\bar{u} \frac{\partial \bar{p}}{\partial x} \quad , \quad (4.10)$$

where $\epsilon_m = v \left(\frac{\partial \bar{u}}{\partial y} \right)^2 \equiv \text{mean flow viscous dissipation}$.

Using an integral approach, the energy provided to an arbitrary volume by imposed pressure gradients in an unmanipulated boundary layer is converted to mean and turbulent viscous dissipation (heat) within the volume, to a net gain or loss in mean and turbulent kinetic energy within the volume, depending upon the transport of total kinetic energy across the boundaries of the volume, to a loss of kinetic and pressure turbulent energy (second term in (4.10)) from the volume (net outward diffusion), and to a loss of stress energy from the volume (net inward transport toward the wall). The total energy equation (4.10), then, contains only one significant mode of energy transfer to the wall, specifically the term $-\frac{\partial}{\partial y} (\hat{\tau} \bar{u})$. Between the viscous sub-layer and the outer region of the boundary layer, mean stress energy is transported to the wall, primarily via the Reynolds stress. Analysis of the same mechanism in the manipulated boundary layer is therefore important.

In the manipulated cases two streamwise domains are of interest, that immediately downstream of the BLM where the flow structure retains identity with an individual honeycomb cell and that where the flow sub-structures have fused. Moller and Leehey found that honeycomb manipulator influence on wall shear and pressure is likewise divided into streamwise zones, one near zone where the manipulator length scale is dominated by honeycomb cell diameter and a downstream zone where the length scale is dominated by manipulator height [5]. For the experiments undertaken, the boundary of these two domains lies approximately ten centimeters downstream of the downstream face of the BLM. In the near-manipulator domain the use of velocity and, particularly,

spatial scale relationships cannot be continued. The honeycomb manipulators destroy the homogeneity of the mean flow on a scale the size of an individual cell, but not necessarily on the whole. Since but one profile measurement was taken in the near-manipulator domain, insufficient data exists to evaluate energy transport mechanisms by conducting a term-by-term breakdown of Equations (4.3) and (4.8). Based on the manipulated profiles four centimeters downstream of the BLM, the stress gradients $\frac{\partial \hat{\tau}_{ij}}{\partial x_j}$ in both x and y directions (and perhaps z) may be significant in this domain. Since Moller and Leehey found an increase in the spanwise ("cross channel") coherence of the wall pressure cross-spectral density in a honeycomb-manipulated boundary layer [5], the manipulator likely transforms the one-dimensional energy transport mechanism of an unmanipulated boundary layer into three-dimensional ones. Thus, the homogeneity of the cross-flow is likewise lost. This effect weakens progressing downstream from the manipulator.

Beyond the near-manipulator domain the flow structure "remembers" the manipulator's effects but undergoes restoration to a form approximating the unmanipulated profile. A most dramatic influence of the manipulator is seen in the strong suppression of the Reynolds stress 25 and 65 centimeters downstream of the manipulator. Also, since the scaling relationships have essentially been restored (i.e. Equation (4.5) applies again), the term $\hat{\tau}\bar{u}$ becomes the dominant mode of energy transport toward the wall. Comparisons of the profiles of the Reynolds stress and $\hat{\tau}\bar{u}$ between the manipulated and unmanipulated cases (Figures 3.13 (a)-(f) and 4.2 (a)-(f), respectively) provide insight into the decrease in τ_w or C_f in the manipulated boundary layer.

Progressing from the closest measurement position downstream of the BLM to the farthest measurement position, the manipulator's influence on energy transport can be deduced. Near the manipulator competing regions of intense Reynolds and viscous

stresses are introduced into the downstream flow as the honeycomb cells destroy the large scale turbulence in the flow. The cyclic alternation of these stresses normal to the wall result in a reduced net transport of energy into the near-wall layer. Thus, wall shear stress decreases. As mentioned previously, more refined measurements at various downstream positions in the near-manipulator domain should indicate which terms of the total stress tensor dominate the transport of energy. Diffusive and particularly convective transport of these stresses cause the regions to merge such that positive and negative stresses superpose to form much lower Reynolds stress levels compared to unmanipulated levels, especially in the mid-layer region. A distinctive Reynolds stress profile, with characteristic mid-layer peaking, emerges as turbulence generated by the manipulator increases in scale due to convective and diffusive transport. Near the wall ($\frac{y}{\delta} < 0.2$) far downstream, the Reynolds stress and $\hat{\tau}\bar{u}$ do not recover to their unmanipulated levels. Although considered a "memory" effect of the manipulator, the physical explanation of the low near-wall stress levels is not apparent from consideration of terms in the kinetic and turbulent energy equations nor from examination of the velocity or stress profiles.

The physical explanation for the reduced wall shear stress at positions downstream of the BLM where the Reynolds stress profile possesses a mid-layer peak may be found in Townsend's interpretation of the transport mechanism of turbulent energy toward the wall. The product of $\hat{\tau}$ and \bar{u} is the quantity of interest. Figures 4.2 (a)-(f) provide profiles of the specific stress energy transport quantity $\hat{\tau}\bar{u}$ normalized to the product $u_{\tau}^2 U_{\infty}$ for each measurement position at the free stream speed of 19 meters per second. The near wall magnitude of $\hat{\tau}\bar{u}$ in the manipulated cases is significantly less than the unmanipulated case. Thus, near the wall the total stress energy available for transport to the wall is reduced by the influence of the manipulator. Hence, wall shear stress or friction coefficient at these locations for the manipulated boundary layer is less than the

unmanipulated layer. The result then of reduced wall shear stresses at the far downstream locations, *despite the mid-layer peaking of the Reynolds stress*, is supported by this analysis of the data in terms of a stress energy transport model.

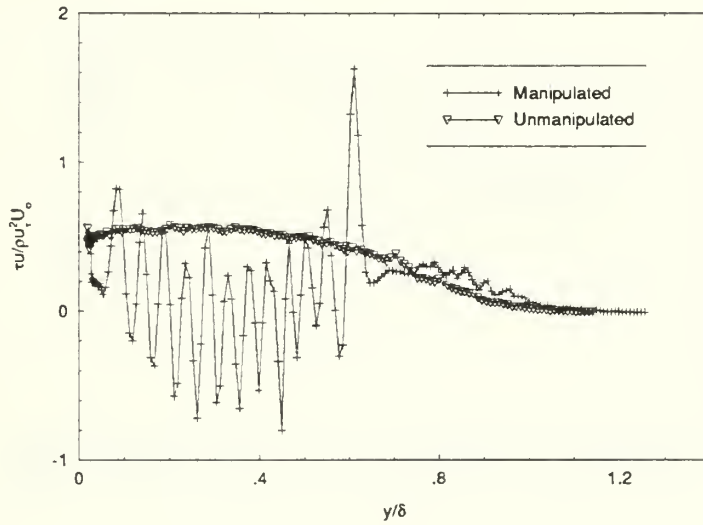


Figure 4.2(a) $\frac{\overline{\tau_w}}{\rho \nu^2 U_\infty}$ vs $\frac{y}{\delta}$ ($U_\infty=19$ m/sec, $x_{BLM}=4$ cm)

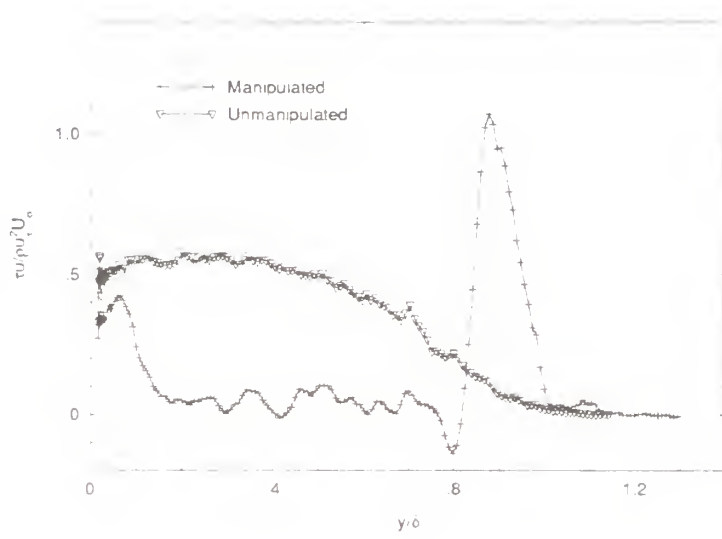


Figure 4.2(b) $\frac{\bar{u}}{u_{\infty}^* L_{\infty}^*}$ vs $\frac{y}{\delta}$ ($U_{\infty}=19$ m/sec, $x_{BLM}=12$ cm)

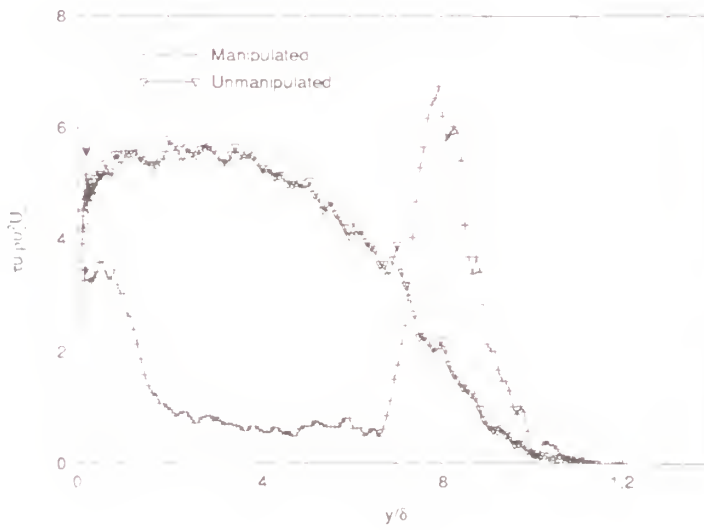


Figure 4.2(c) $\frac{\bar{u}}{u_{\infty}^* L_{\infty}^*}$ vs $\frac{y}{\delta}$ ($U_{\infty}=19$ m/sec, $x_{BLM}=25$ cm)

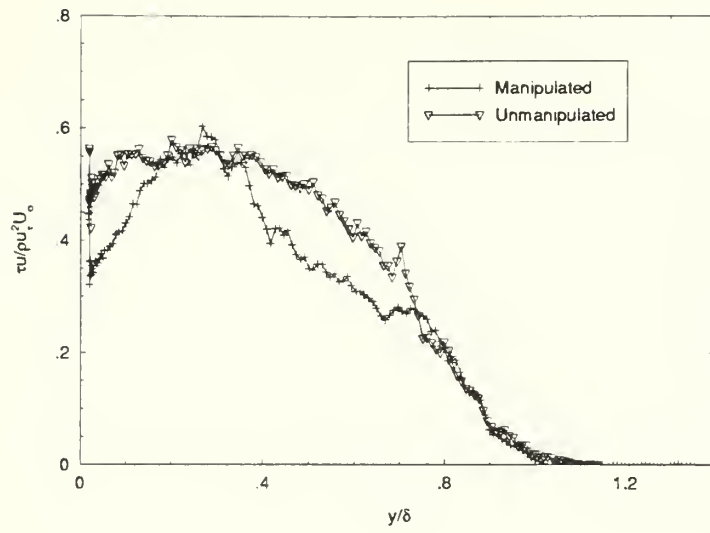


Figure 4.2(d) $\frac{\tau u}{u_\tau^2 U_\infty}$ vs $\frac{y}{\delta}$ ($U_\infty=19$ m/sec, $x_{BLM}=65$ cm)

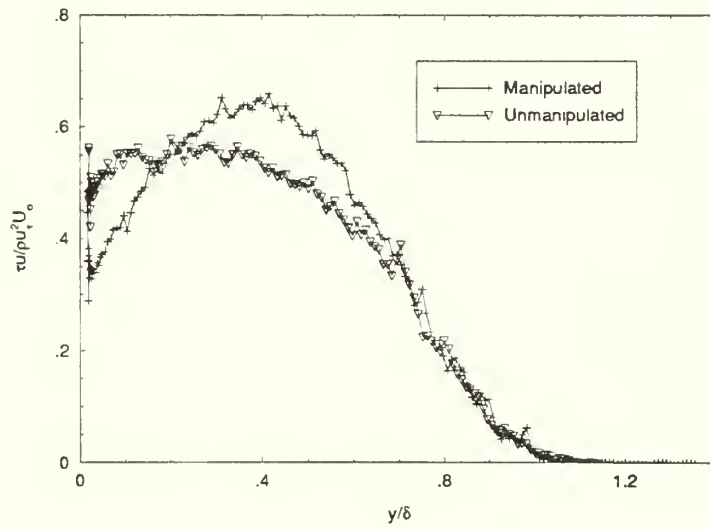


Figure 4.2(e) $\frac{\tau u}{u_\tau^2 U_\infty}$ vs $\frac{y}{\delta}$ ($U_\infty=19$ m/sec, $x_{BLM}=100$ cm)

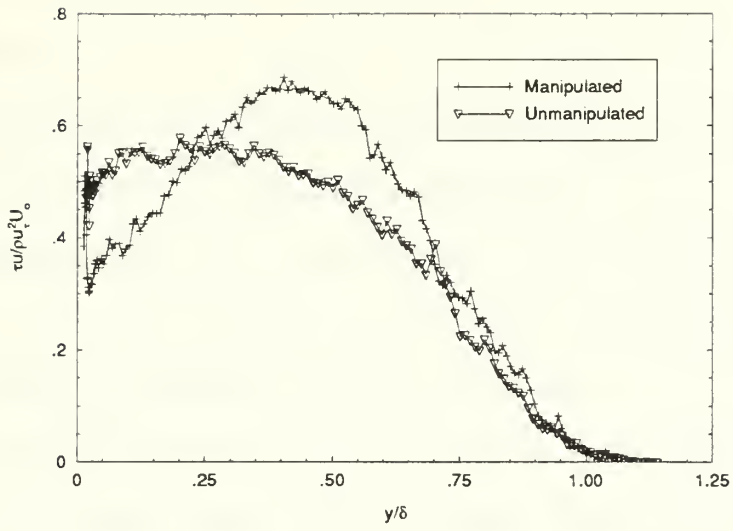


Figure 4.2(f) $\frac{\overline{\tau_w}}{\mu_\infty^2 U_\infty}$ vs $\frac{y}{\delta}$ ($U_\infty=19$ m/sec, $x_{BLM}=150$ cm)

5 Conclusions and Recommendations

5.1 Conclusions

Numerous conclusions follow from the data obtained from X-probe and surface pressure measurements in honeycomb-manipulated boundary layers:

(1) Relationships describing the turbulent energy decay and streamwise velocity variations downstream of free stream honeycomb manipulators and grids do not apply to wall-bounded turbulence manipulated by honeycomb structures.

(2) Velocity and stress profiles downstream of a honeycomb manipulator are characterized by two domains, a near-manipulator domain where the profiles possess a structure determined by individual cells of the manipulator and a downstream domain where the profiles lose the cell-induced sub-structures. For the manipulators used in the measurements, the near-manipulator domain ends approximately 10 centimeters downstream of the downstream face of the BLM.

(3) Honeycomb-manipulated boundary layers exhibit local drag reductions up to 40% compared to an unmanipulated boundary layer at the same free stream speed. The greatest drag reduction or reduction in wall shear stress occurs immediately downstream of the manipulator, and drag reduction persists $150 \delta_{und}^*$ downstream at a level 15% below the unmanipulated case.

(4) Honeycomb manipulators introduce a structure into the downstream flow which strongly suppress the transport of stress energy toward the wall, particularly via the working of Reynolds stresses. The wall-normal gradient of the transport term $\hat{\tau}\bar{u}$, composed primarily of the Reynolds stress except near the wall, determines the flow of energy toward the wall beyond the near-manipulator domain. The reduction in stress energy transported to the wall appears to be the principal cause of the decreased magnitude of the wall shear stress/friction coefficient.

(5) Mid-layer peaking in the Reynolds stress levels of the honeycomb-manipulated boundary layers well downstream of the manipulator was found to conform to previous work with flat plate-type manipulators. Although there are increased levels of Reynolds stress in the mid-layer, there is less stress energy near the wall compared to the unmanipulated boundary layer, resulting in decreased wall shear stress downstream of the manipulator.

(6) The honeycomb manipulator produces sizable oscillations in the mean vertical velocity profile immediately downstream of the manipulator, which decay significantly within the near-manipulator domain. The same behavior is exhibited by the mean stream velocity profile and stress profiles.

(7) Manipulated boundary layers do not adhere to Coles' law of the wall although some profiles were found to closely approximate this law.

5.2 Recommendations

Although all specified objectives were accomplished, the results obtained from manipulated boundary layer measurements warrant similar investigations of expanded scale. To this end, the following recommendations are offered:

(1) Velocity and stress profiles should be measured at fine streamwise steps in the near-manipulator domain to explore in detail the energy transport mechanisms responsible for the strong mid-layer suppression of the Reynolds stress in the downstream domain. Likewise, an increased number of velocity and stress profiles at smaller streamwise intervals should be measured to determine similar mechanisms accounting for the gradual development of the mid-layer peak in Reynolds stress levels farther downstream.

(2) The tops of the manipulators should be tapered and smoothed in an attempt to reduce the large shearing peak introduced into the velocity and stress profiles and to determine any influence of this phenomenon upon energy transport via Reynolds stress.

(3) The speed range of all measurements should be expanded to obtain a more comprehensive understanding of dependencies of the velocity and stress profiles and of energy transport on Reynolds numbers.

(4) A consistent "optimal" manipulator height ($h_{BLM} \propto x^{0.8}$) should be maintained over the entire speed range as x_{BLM} varies, and a constant manipulator height, above and below optimal, should be maintained throughout the speed range as x_{BLM} varies. In this way the variation of $C_{f,m}/C_{f,um}$ with x_{BLM}/δ_{und}^* and h_{BLM}/δ_{und}^* is best determined (see Fig. 4.1). Then, based on these findings, changes should be considered separately in manipulator honeycomb cell size and length.

(5) Maintain X-probe calibration using the velocity-angle-voltage technique to ensure that mean vertical velocity variations are accurately measured. Measurement of the w -component of mean and fluctuating velocities ("cross flow") via triple hot-wire techniques is recommended to obtain a detailed knowledge of all velocity and stress influences. Then, the effects of all stress components (τ_{ij} and $\overline{u_i u_j}$, $i, j = 1, 2, 3$) in energy transport processes can be deduced.

References

- [1] Beeler, G. A., Turbulent Boundary-Layer Wall Pressure Fluctuations Downstream of a Tandem LEBU, AIAA Journal, Volume 24, Number 4, pp, 689-691, April, 1986.
- [2] Nguyen, V. D., et al, Some Experimental Observations of the Law of the Wall Behind Large Eddy Breakup Devices Using Servo-Controlled Skin Friction Balances, AIAA Paper 84-0346, pp. 1-13, January, 1984.
- [3] Coles, D. E., The Law of the Wall in Turbulent Shear Flow, 50 Jahre Grenzschichtforschung, (H. Gortler & W. Tollmien, eds.), F. Vieweg und Sohn, Braunschweig, pp. 153-163.
- [4] Hefner, J. N., Weinstein, L.M., and Bushnell, D.M., Large-Eddy Breakup Scheme for Turbulent Viscous Drag Reduction, Progress in Astronautics and Aeronautics, Volume 72, pp. 111-127, 1980.
- [5] Moller, J. C. and Leehey, P., Measurement of Wall Shear and Wall Pressure Downstream of a Honeycomb Boundary Layer Manipulator, Acoustics and Vibration Laboratory Report No. 97457-3, Massachusetts Institute of Technology, April, 1989.
- [6] Roth, K. W. and Leehey, P., Velocity Profile and Wall Shear Stress Measurements for a Large Eddy Break-up Device (LEBU), Acoustics and Vibration Laboratory Report No. 71435-1, Massachusetts Institute of Technology, November, 1989.
- [7] Westphal, R. V., Skin Friction and Reynolds Stress Measurements for a Turbulent Boundary Layer Following Manipulation Using Flat Plates, AIAA Paper, AIAA-86-0283, AIAA, New York, NY, 1986.
- [8] Townsend, A. A., The Structure of Turbulent Shear Flow, Cambridge University Press, Cambridge, England, 1976 (Second Edition).
- [9] Klebanoff, P., Characteristics of Turbulence in a Boundary Layer with Zero Pressure Gradient, National Advisory Committee for Aeronautics, Technical Note 3178 (NACA TN 3178), July 1954.
- [10] Hanson, C. E., The Design and Construction of a Low Noise, Low Turbulence Wind Tunnel, Acoustics and Vibration Laboratory Report No. 79611-1, Massachusetts Institute of Technology, 1969.
- [11] TSI Incorporated, Hot Wire/Hot Film Anemometry Probes & Accessories, St. Paul, MN, 1988.
- [12] Vagt, J. D. and Fernholz, H., Use of Surface Fences to Measure Wall Shear Stress in Three-dimensional Boundary Layers, Aeronautical Quarterly, May, 1973.
- [13] Schlichting, H., Boundary-Layer Theory, McGraw-Hill Book Company, New York, NY, 1968.

- [14] Lomas, C. G., Fundamentals of Hot Wire Anemometry, Cambridge University Press, New York, NY, 1986.
- [15] Perry, A. E., Hot-Wire Anemometry, Oxford University Press, New York, NY, 1982.
- [16] Schubauer, G. B. and Klebanoff, P. S., Theory and Application of Hot-Wire Instruments in the Investigation of Turbulent Boundary Layers, National Advisory Committee for Aeronautics, **Wartime Report (W-86)**, originally issued March 1946 as ACR-5k27.
- [17] Lekakis, I. C., Coherent Structures in Fully Developed Pipe Flow, Doctoral Thesis, University of Illinois at Urbana-Champaign, Department of Mechanical Engineering, 1988.
- [18] Westphal, R. V. et al, Crossed Hot-Wire Data Acquisition and Reduction System, NASA TM-85871, January, 1984.
- [19] Willmarth, W. W. and Bogar, T. J., Survey and New Measurements of Turbulent Structure Near the Wall, **The Physics of Fluids**, Vol. 20, No. 10, Part II, October, 1977.
- [20] Lueptow, R., The Turbulent Boundary Layer on a Cylinder in Axial Flow, Doctoral Thesis, Massachusetts Institute of Technology Department of Mechanical Engineering, 1986.
- [21] Cebeci, T. and Smith, A. M. O., Analysis of Turbulent Boundary Layers, Academic Press, New York, NY, 1974.
- [22] Johnson, F. D. and Eckelmann, H., A Variable Angle Method of Calibration for X-probes Applied to Wall-Bounded Turbulent Shear Flow, **Experiments in Fluids** 2, pp. 121-130, 1984.
- [23] Lueptow, R. M., Breuer, K. S., and Haritonidis, J. H., Computer-aided Calibration of X-probes Using a Look-up Table, **Experiments in Fluids** 6, pp. 115-118, 1988.
- [24] Oster, D. and Wygnanski, I., The Forced Mixing Layer Between Parallel Streams, **The Journal of Fluid Mechanics** (123), pp. 91-130, 1982.
- [25] Newland, D. E., An Introduction to Random Vibrations and Spectral Analysis, (Second Edition), John Wiley & Sons, Inc., New York, NY, 1984.
- [26] Lumley, J. and McMahon, J., Reducing Water Tunnel Turbulence by Means of a Honeycomb, **Journal of Basic Engineering**, Transactions of the ASME, Volume 89, pp. 764-770, December, 1967.
- [27] Loehrke, R. and Nagib, H., Control of Free-Stream Turbulence by Means of Honeycombs: A Balance Between Suppression and Generation, **Journal of Basic Engineering**, Transactions of the ASME, Volume 98, pp. 342-353, September, 1976.

- [28] Batchelor, G., The Theory of Homogeneous Turbulence, Cambridge University Press, London, England, 1960.
- [29] Hinze, J., Turbulence, McGraw-Hill Book Company, Inc., New York, NY, 1959.
- [30] Lomas, C., Fundamentals of Hot Wire Anemometry, Cambridge University Press, New York, NY, 1986.

Appendix A Supplementary Graphs

The body of this document contained graphical representations of data at the speed of 19 meters per second for both manipulated and unmanipulated boundary layer measurements. For completeness and comparison the data collected at 15 and 23 meters per second are included in this Appendix. The order of presentation follows that for 19 meters per second and includes both unmanipulated and manipulated data as found in Sections 3.2.1, 3.2.2, and 3.3.2 only.

A.1 Fifteen Meters Per Second Data

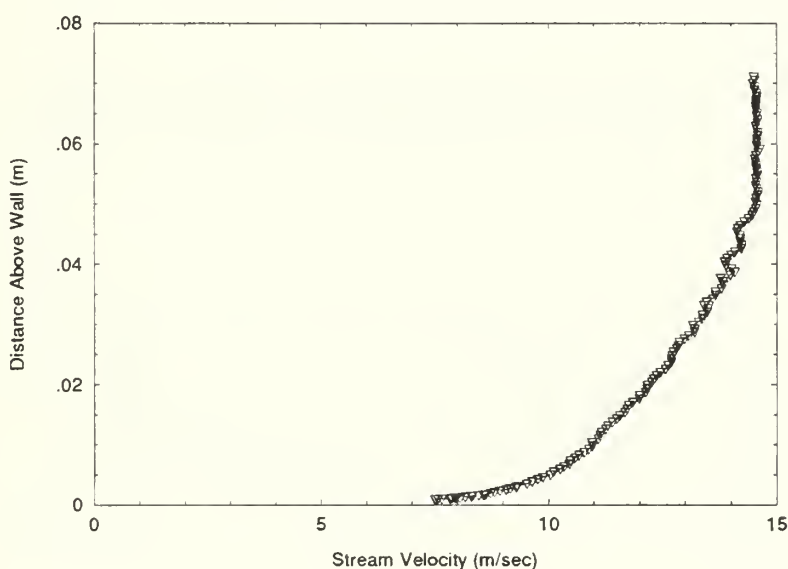


Figure A.1.1 Unmanipulated Mean Velocity Profile ($U_{\infty}=15$ m/sec)

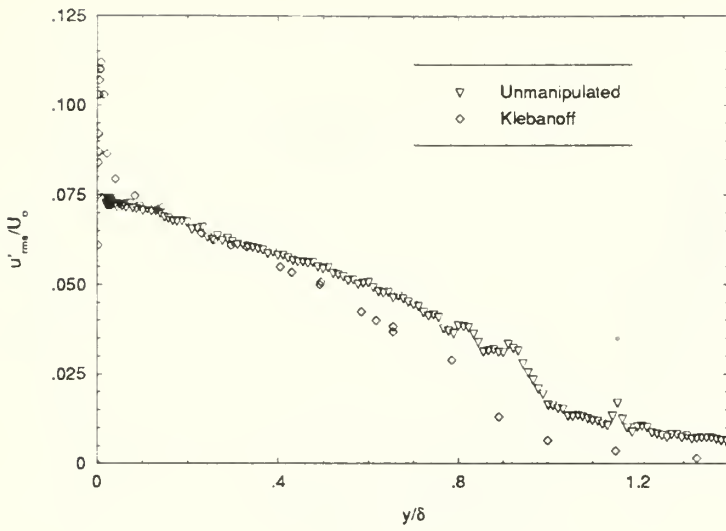


Figure A.1.2 $\frac{\sqrt{u'^2}}{U_{\infty}}$ vs $\frac{y}{\delta}$ (Unmanipulated, $U_{\infty}=15$ m/sec)

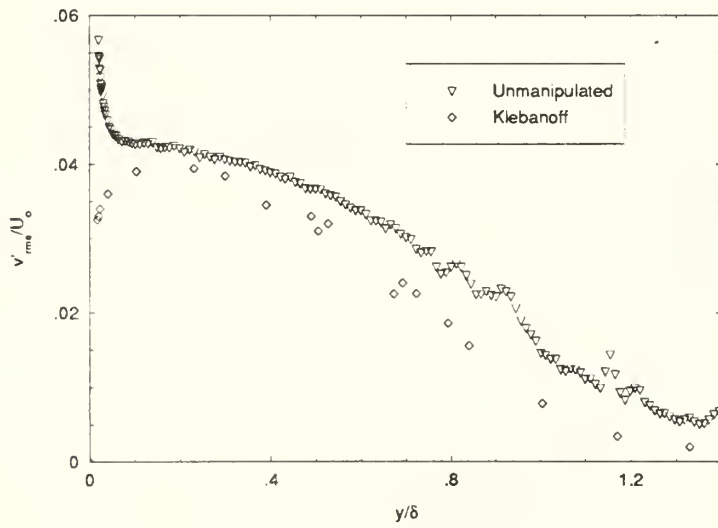


Figure A.1.3 $\frac{\sqrt{v'^2}}{U_{\infty}}$ vs $\frac{y}{\delta}$ (Unmanipulated, $U_{\infty}=15$ m/sec)

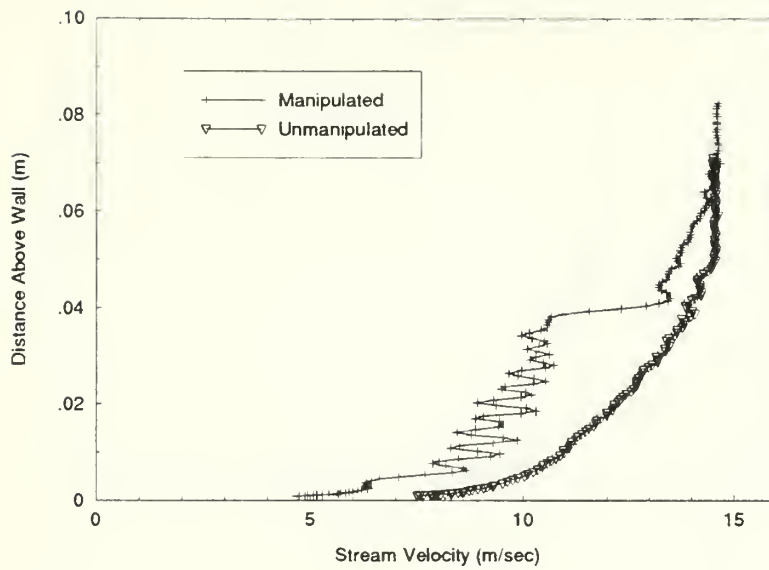


Figure A.1.4 Stream Velocity Profile Comparison ($x_{BLM}=4$ cm)

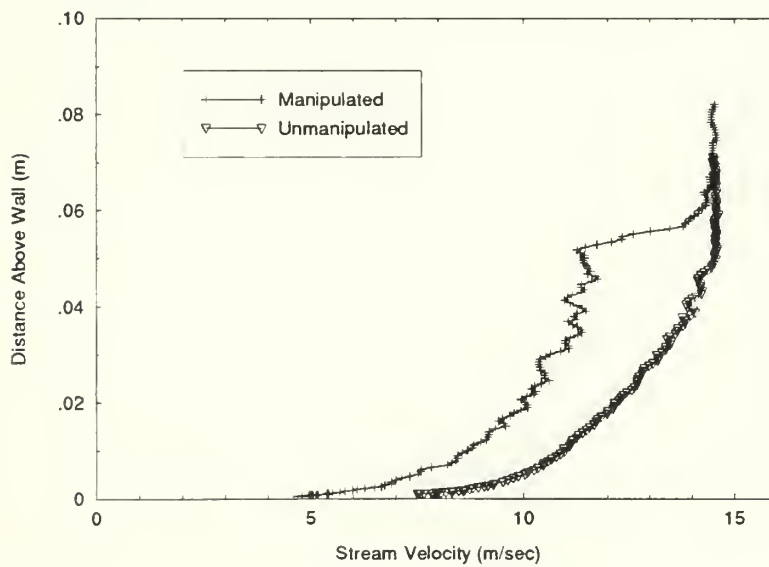


Figure A.1.5 Stream Velocity Profile Comparison ($x_{BLM}=12$ cm)

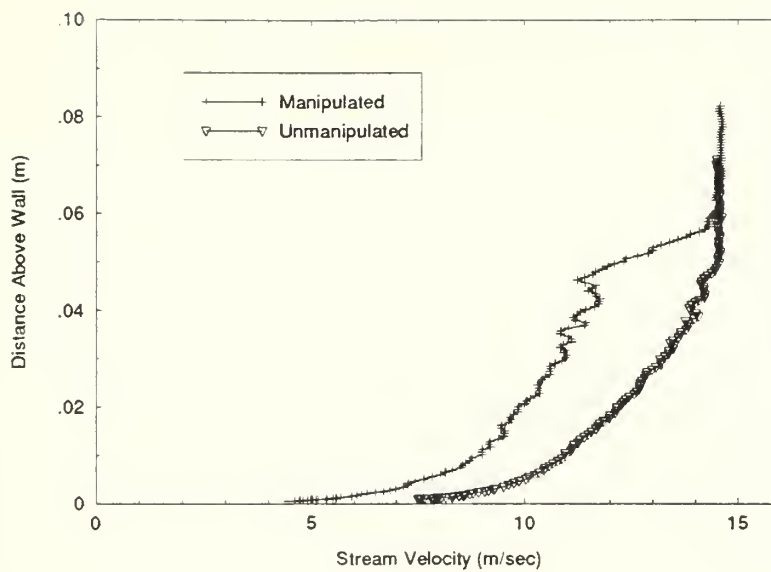


Figure A.1.6 Stream Velocity Profile Comparison ($x_{BLM}=25$ cm)

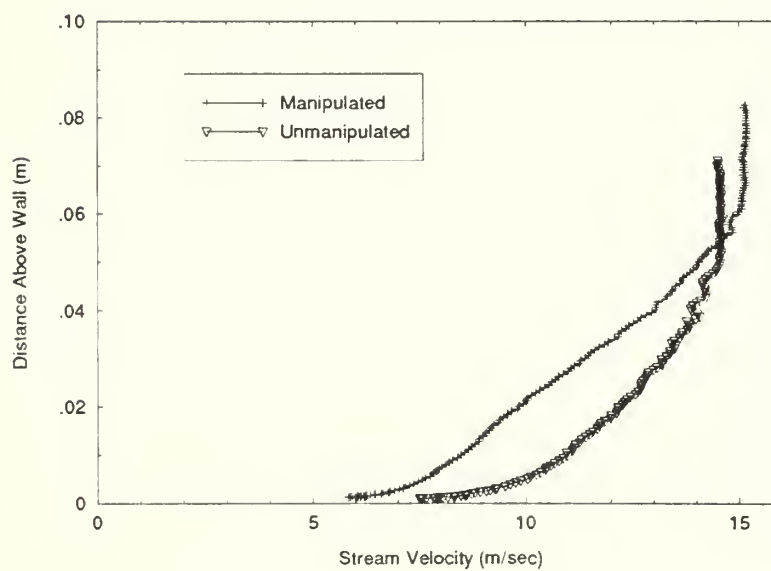


Figure A.1.7 Stream Velocity Profile Comparison ($x_{BLM}=65$ cm)

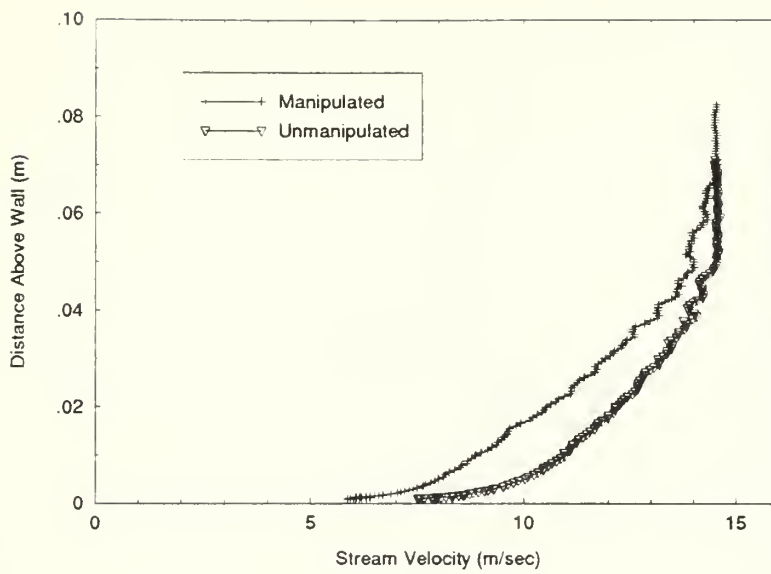


Figure A.1.8 Stream Velocity Profile Comparison ($x_{BLM}=100$ cm)

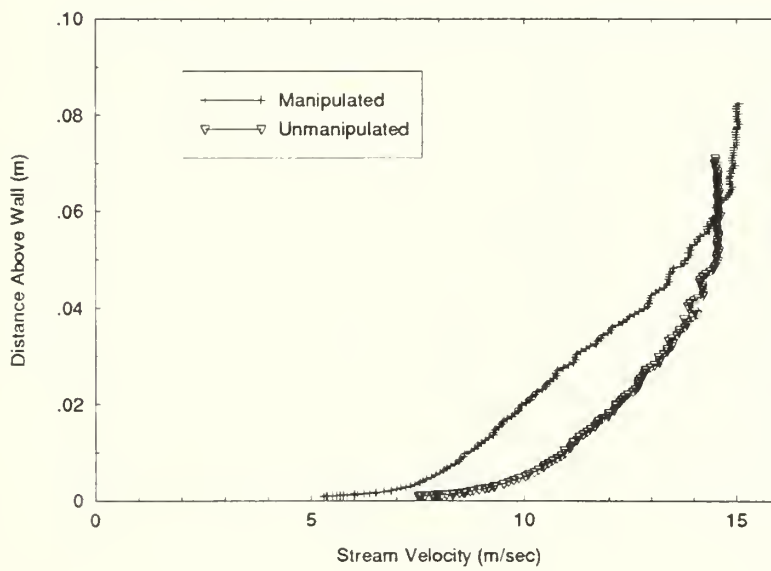


Figure A.1.9 Stream Velocity Profile Comparison ($x_{BLM}=150$ cm)

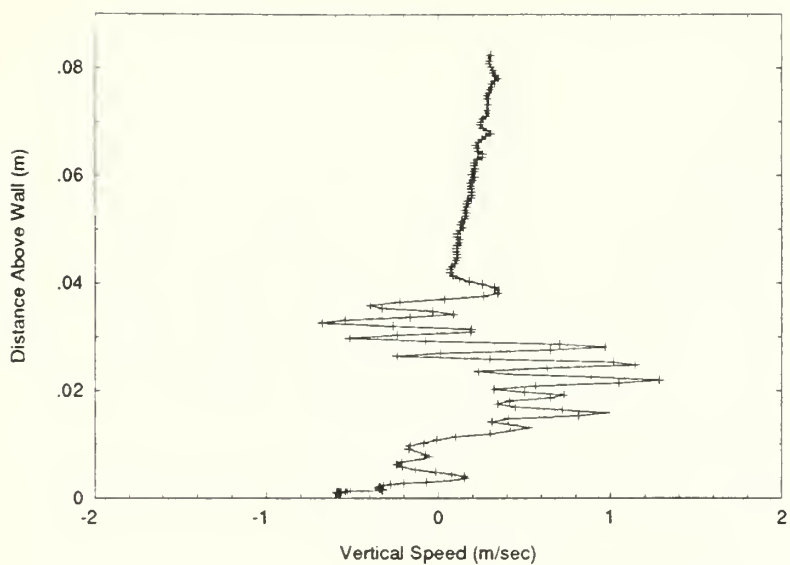


Figure A.1.10 Vertical Velocity Profile ($x_{BLM}=4$ cm)

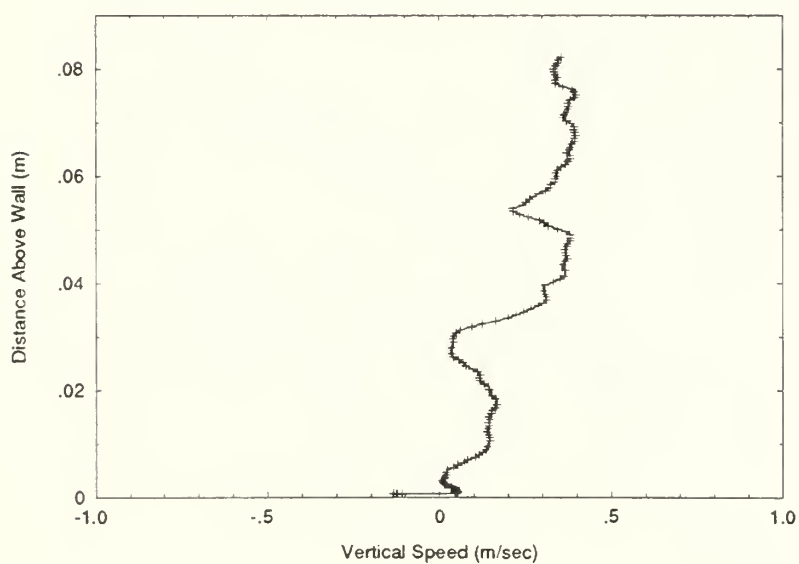


Figure A.1.11 Vertical Velocity Profile ($x_{BLM}=12$ cm)

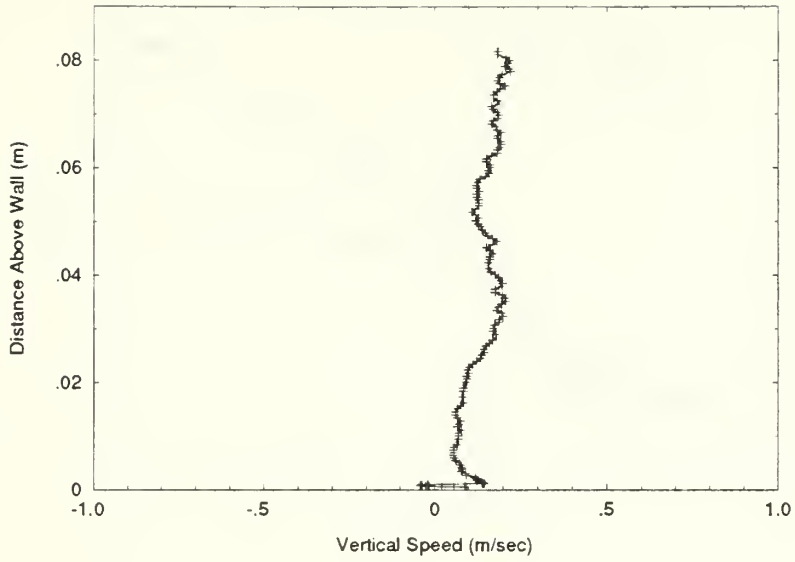


Figure A.1.12 Vertical Velocity Profile ($x_{BLM}=25$ cm)

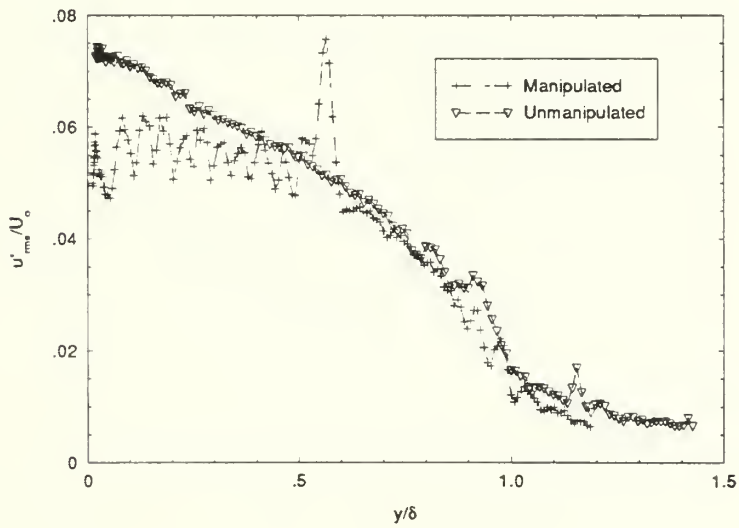


Figure A.1.13 $\frac{\sqrt{u'^2}}{U_\infty}$ vs $\frac{y}{\delta}$ ($x_{BLM}=4$ cm)

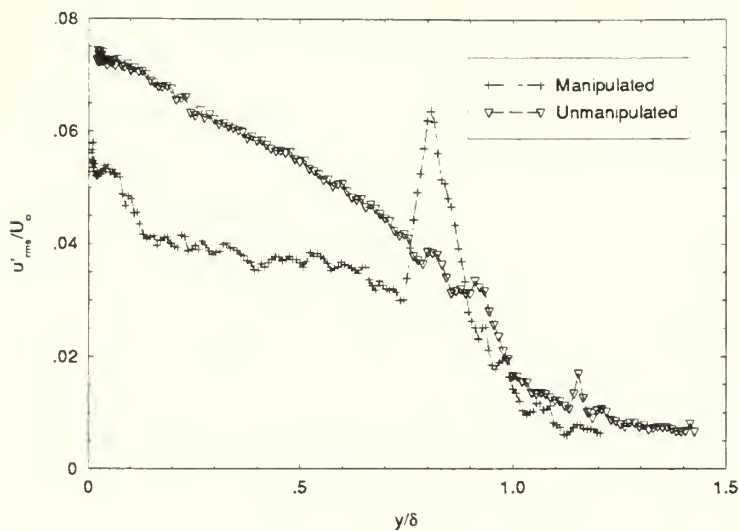


Figure A.1.14 $\frac{\sqrt{u'^2}}{U_{\infty}}$ vs $\frac{y}{\delta}$ ($x_{\text{BLM}}=12$ cm)

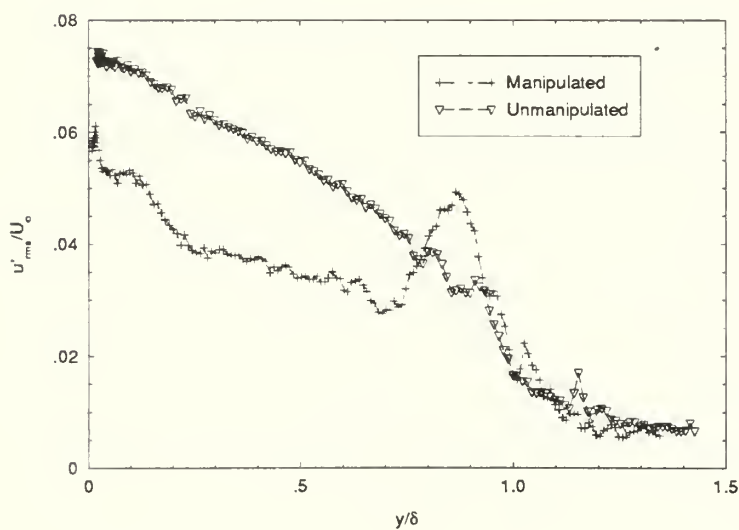


Figure A.1.15 $\frac{\sqrt{u'^2}}{U_{\infty}}$ vs $\frac{y}{\delta}$ ($x_{\text{BLM}}=25$ cm)

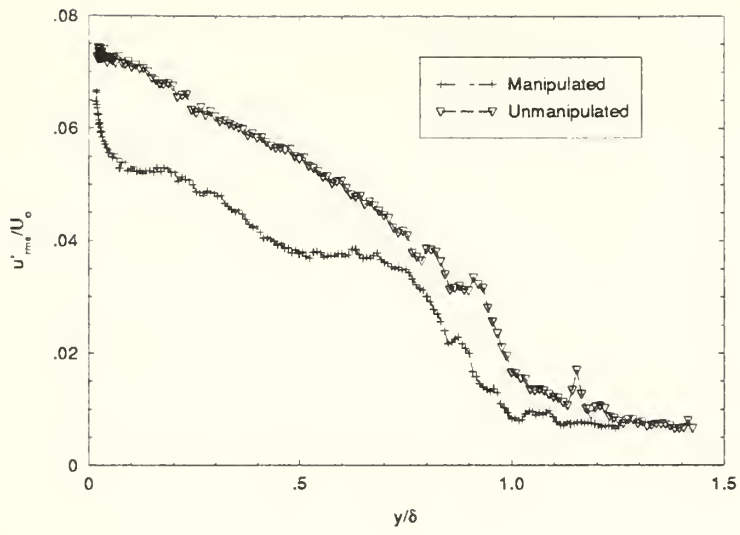


Figure A.1.16 $\frac{\sqrt{u'^2}}{U_\infty}$ vs $\frac{y}{\delta}$ ($x_{BLM}=65$ cm)

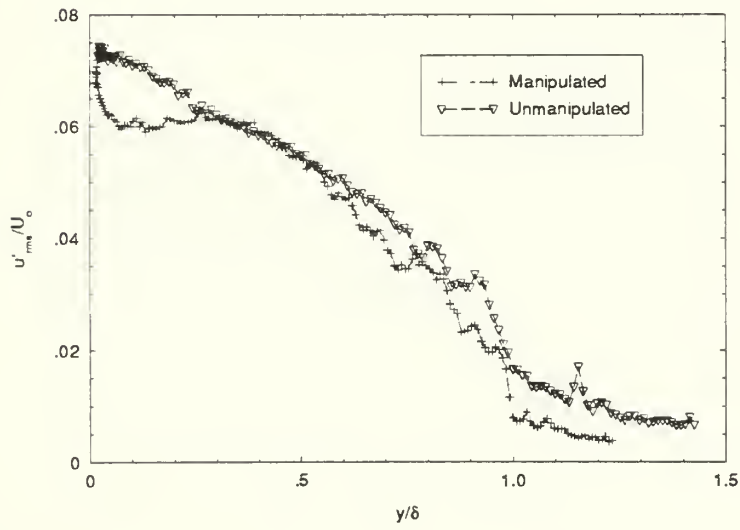


Figure A.1.17 $\frac{\sqrt{u'^2}}{U_\infty}$ vs $\frac{y}{\delta}$ ($x_{BLM}=100$ cm)

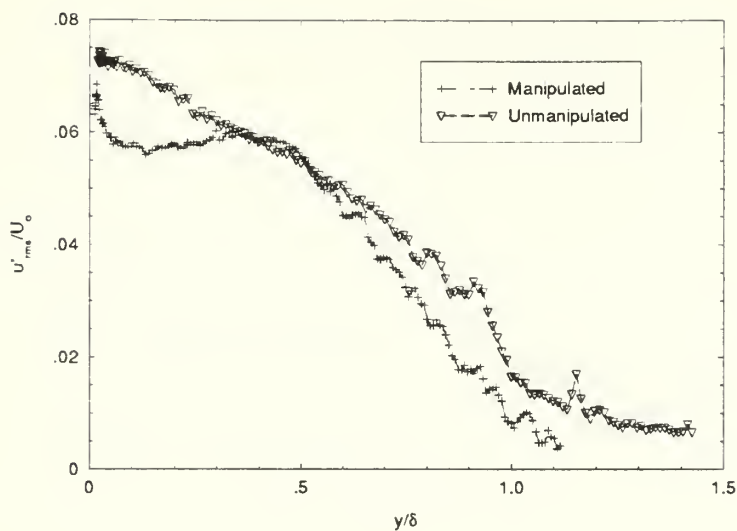


Figure A.1.18 $\frac{\sqrt{u'^2}}{U_{\infty}}$ vs $\frac{y}{\delta}$ ($x_{BLM}=150$ cm)

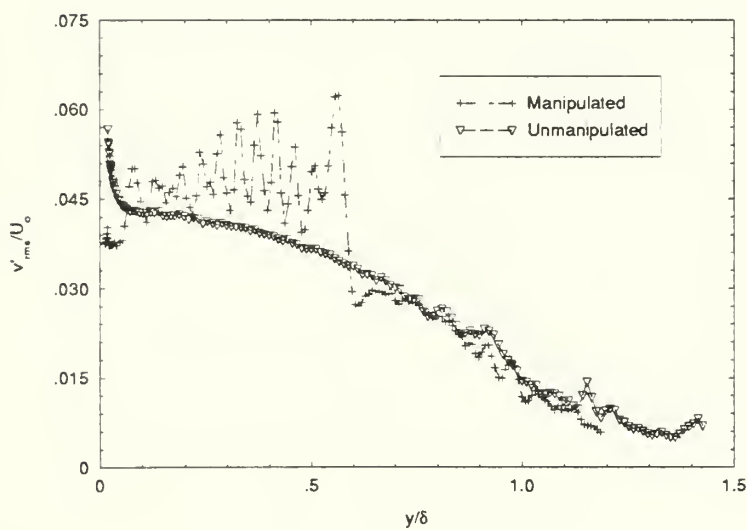


Figure A.1.19 $\frac{\sqrt{v'^2}}{U_{\infty}}$ vs $\frac{y}{\delta}$ ($x_{BLM}=4$ cm)

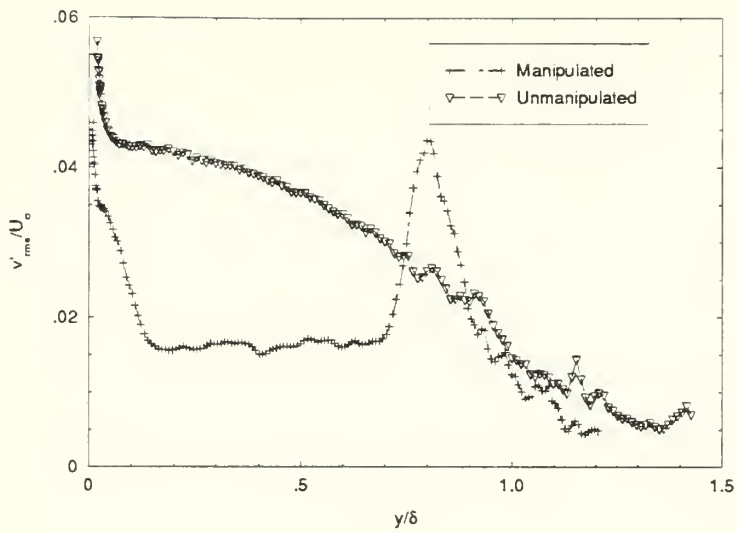


Figure A.1.20 $\frac{\sqrt{v'^2}}{U_\infty}$ vs $\frac{y}{\delta}$ ($x_{\text{BLM}}=12$ cm)

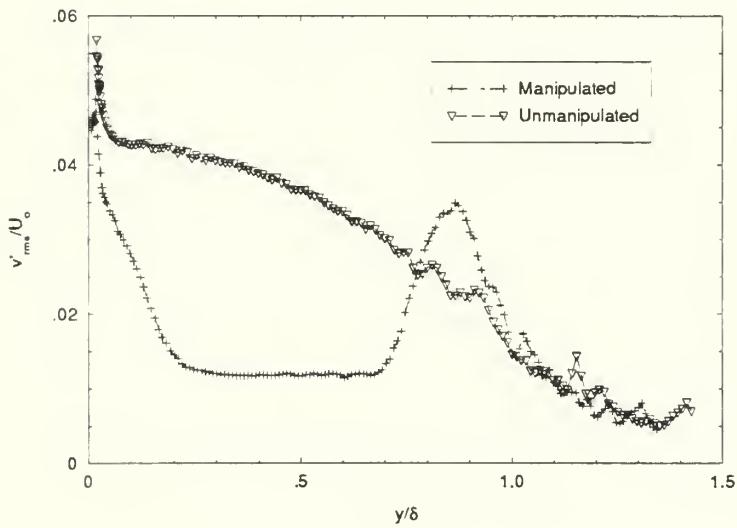


Figure A.1.21 $\frac{\sqrt{v'^2}}{U_\infty}$ vs $\frac{y}{\delta}$ ($x_{\text{BLM}}=25$ cm)

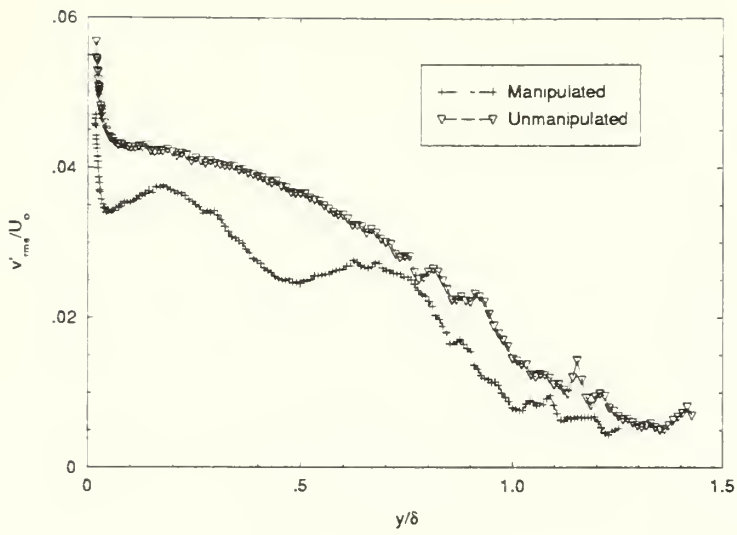


Figure A.1.22 $\frac{\sqrt{v'^2}}{U_\infty}$ vs $\frac{y}{\delta}$ ($x_{BLM}=65$ cm)

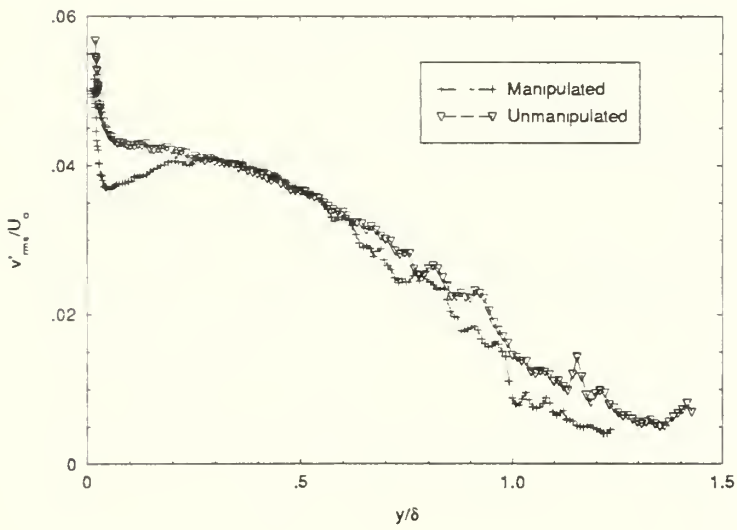


Figure A.1.23 $\frac{\sqrt{v'^2}}{U_\infty}$ vs $\frac{y}{\delta}$ ($x_{BLM}=100$ cm)

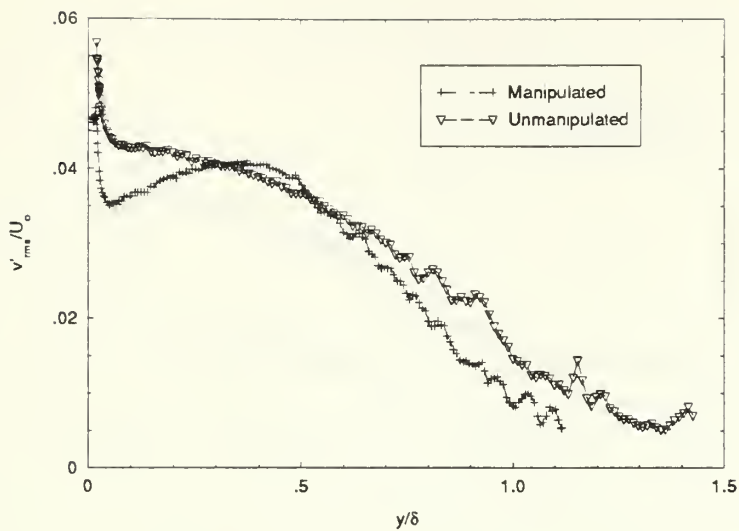


Figure A.1.24 $\frac{\sqrt{v'^2}}{U_\infty}$ vs $\frac{y}{\delta}$ ($x_{BLM}=150$ cm)

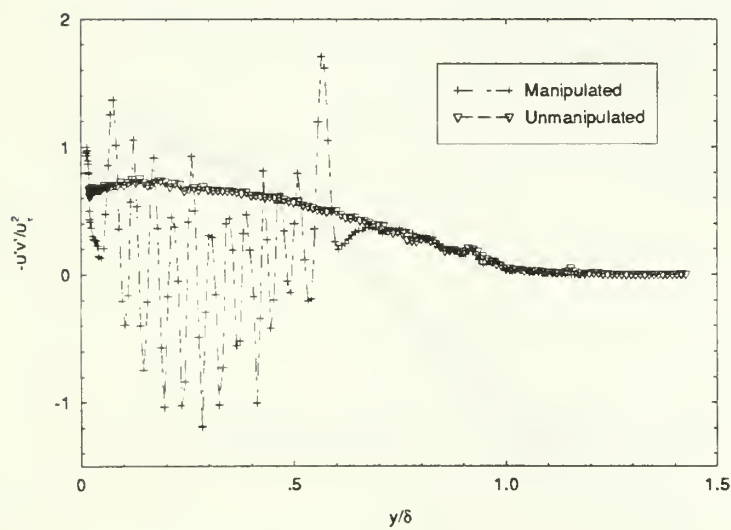


Figure A.1.25 $\frac{-\overline{u'v'}}{u_\tau^2}$ vs $\frac{y}{\delta}$ ($x_{BLM}=4$ cm)

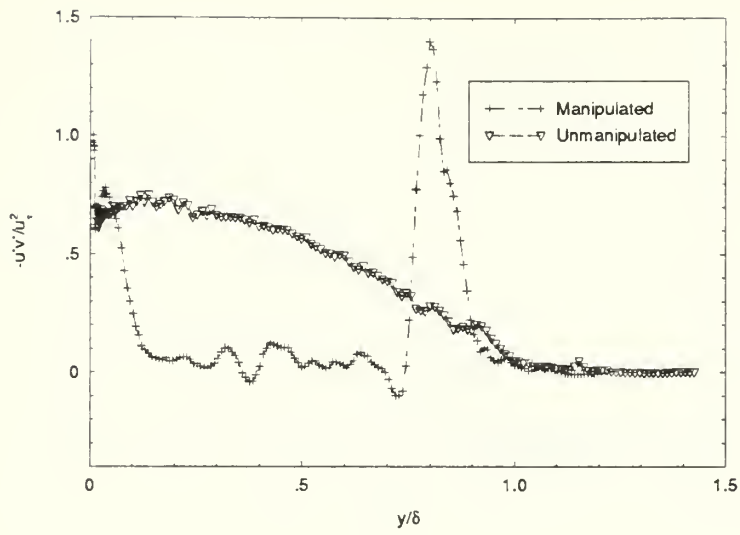


Figure A.1.26 $\frac{-\overline{u'v'}}{u_\tau^2}$ vs $\frac{y}{\delta}$ ($x_{BLM}=12$ cm)

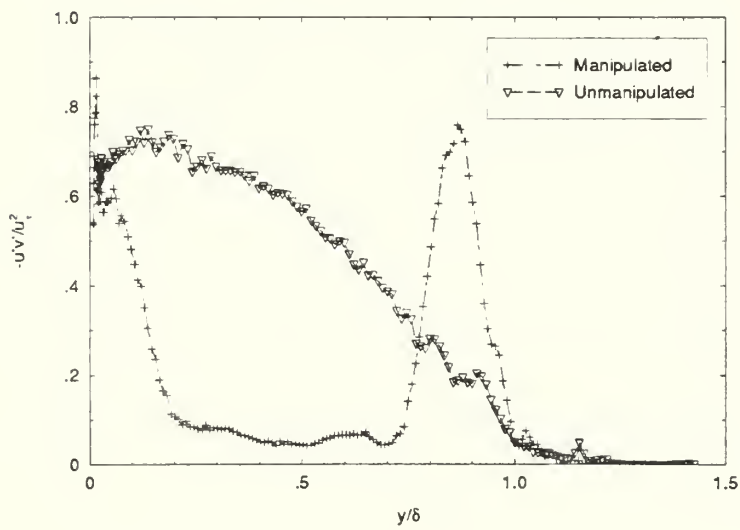


Figure A.1.27 $\frac{-\overline{u'v'}}{u_\tau^2}$ vs $\frac{y}{\delta}$ ($x_{BLM}=25$ cm)

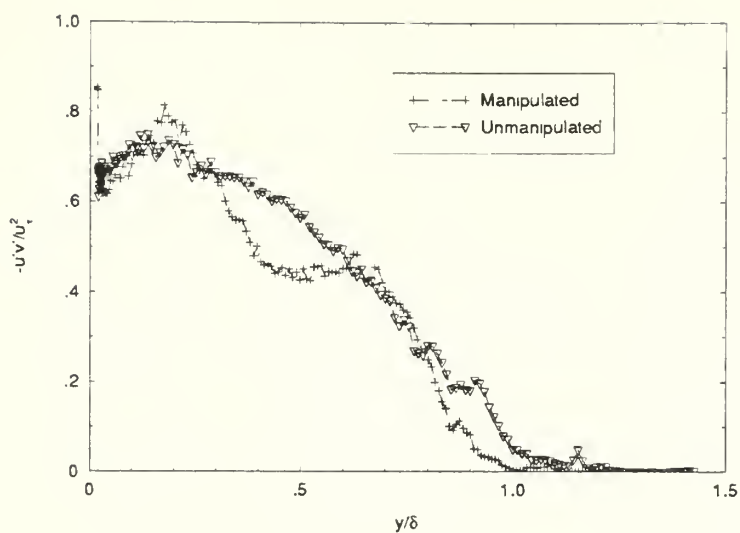


Figure A.1.28 $\frac{-\overline{u'v'}}{u_\tau^2}$ vs $\frac{y}{\delta}$ ($x_{BLM}=65$ cm)

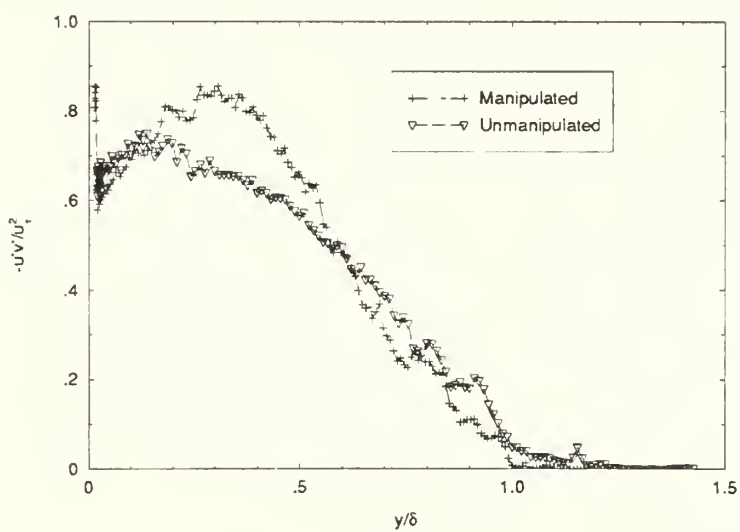


Figure A.1.29 $\frac{-\overline{u'v'}}{u_\tau^2}$ vs $\frac{y}{\delta}$ ($x_{BLM}=100$ cm)

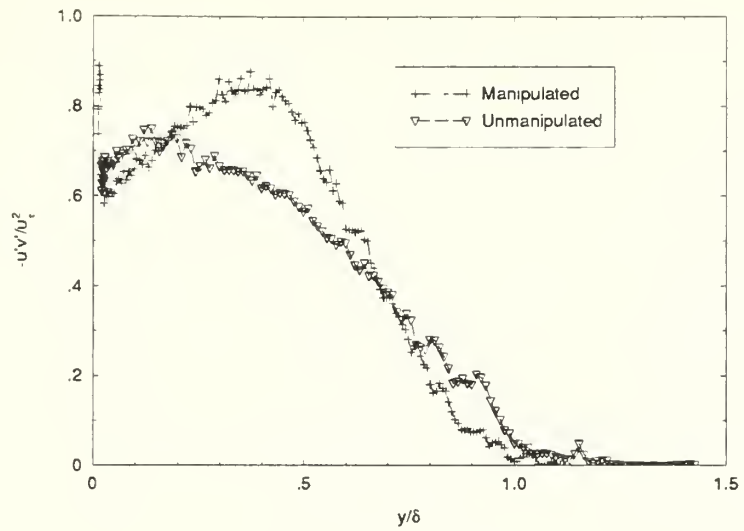


Figure A.1.30 $\frac{-\overline{u'v'}}{u_{\tau}^2}$ vs $\frac{y}{\delta}$ ($x_{BLM}=150$ cm)

A.2 Twenty-Three Meters Per Second Data

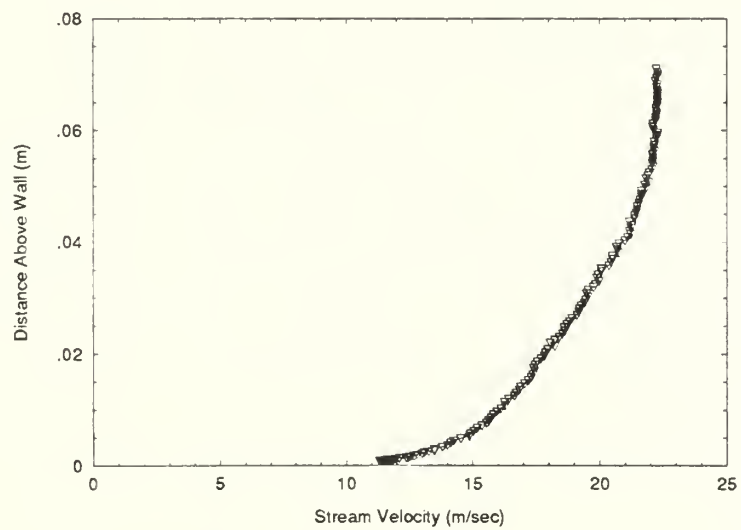


Figure A.2.1 Unmanipulated Mean Velocity Profile ($U_{\infty}=23$ m/sec)

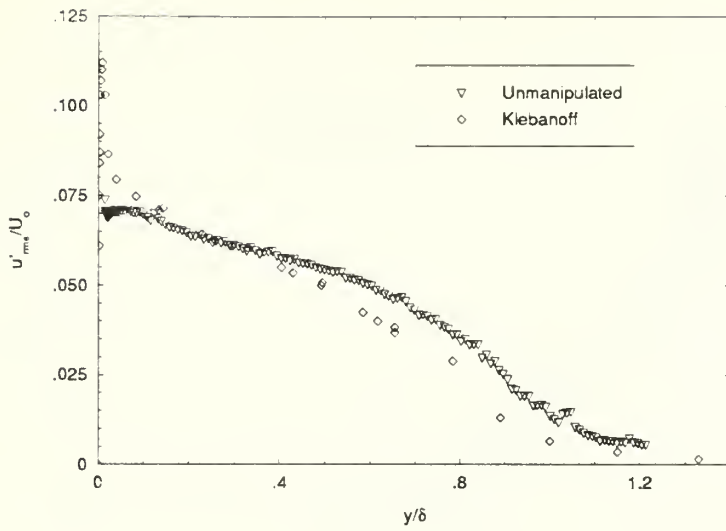


Figure A.2.2 $\frac{\sqrt{u'^2}}{U_\infty}$ vs $\frac{y}{\delta}$ (Unmanipulated, $U_\infty=23$ m/sec)

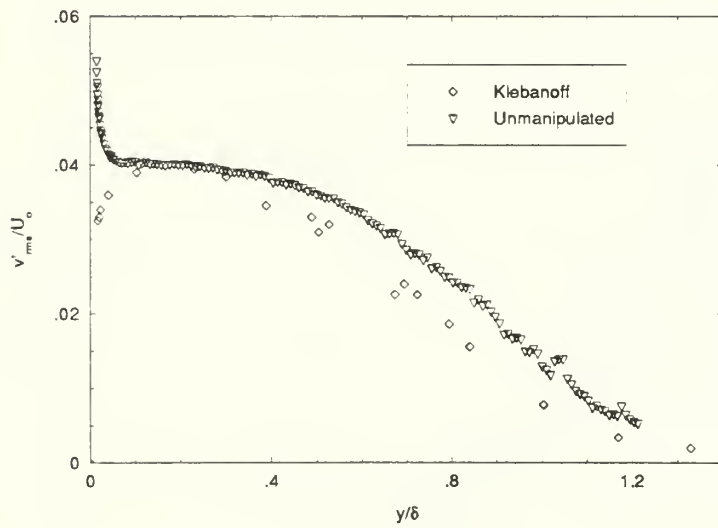


Figure A.2.3 $\frac{\sqrt{v'^2}}{U_\infty}$ vs $\frac{y}{\delta}$ (Unmanipulated, $U_\infty=23$ m/sec)

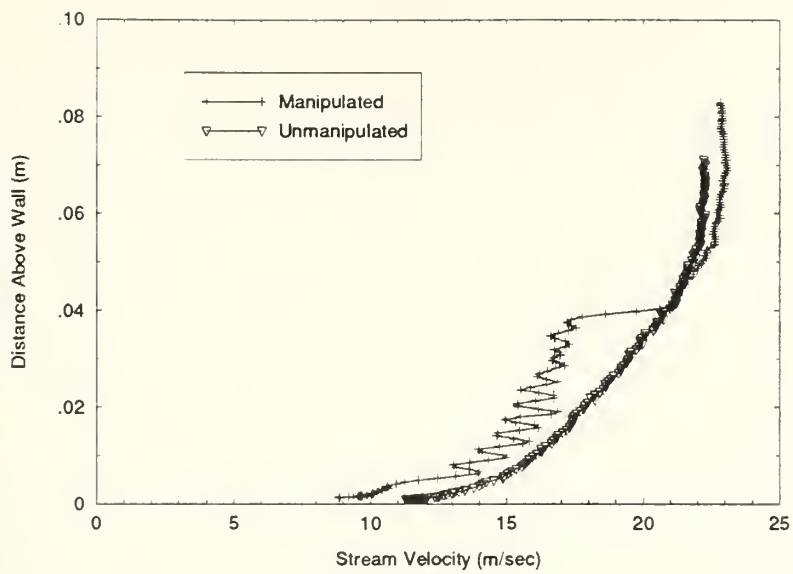


Figure A.2.4 Stream Velocity Profile Comparison ($x_{BLM}=4$ cm)

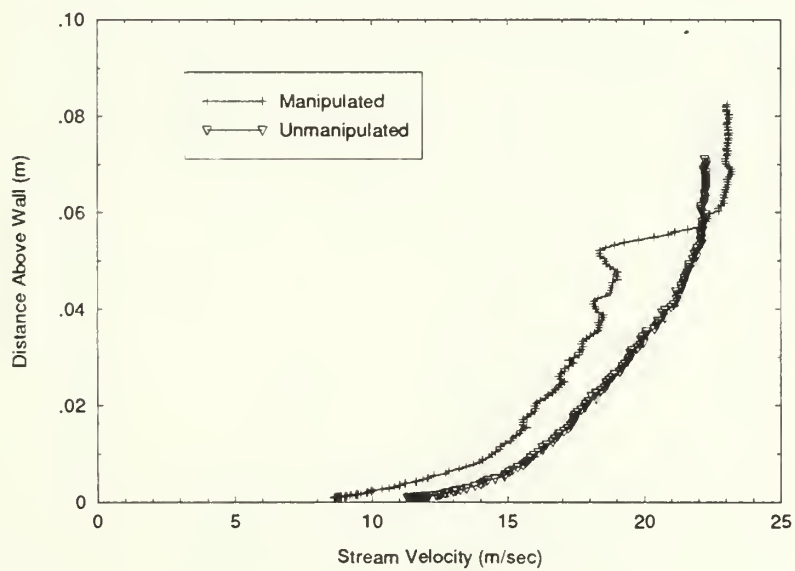


Figure A.2.5 Stream Velocity Profile Comparison ($x_{BLM}=12$ cm)

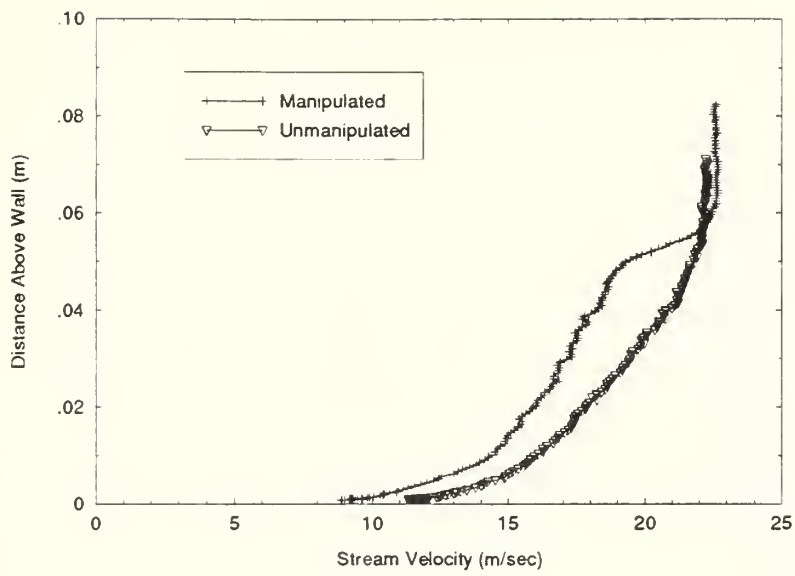


Figure A.2.6 Stream Velocity Profile Comparison ($x_{BLM}=25$ cm)

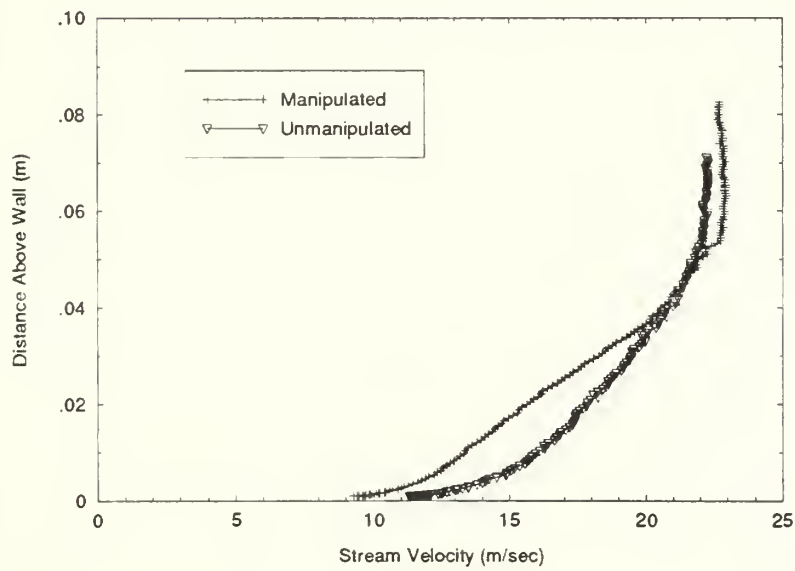


Figure A.2.7 Stream Velocity Profile Comparison ($x_{BLM}=65$ cm)

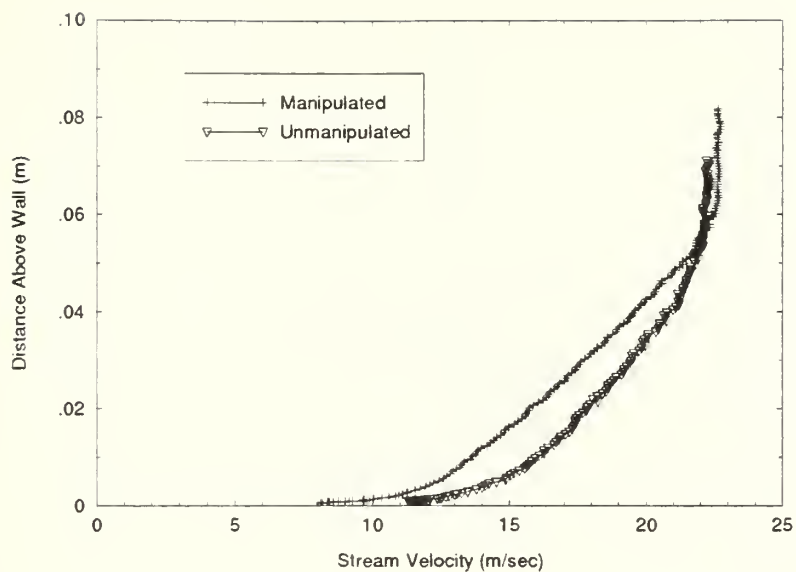


Figure A.2.8 Stream Velocity Profile Comparison ($x_{BLM}=100$ cm)

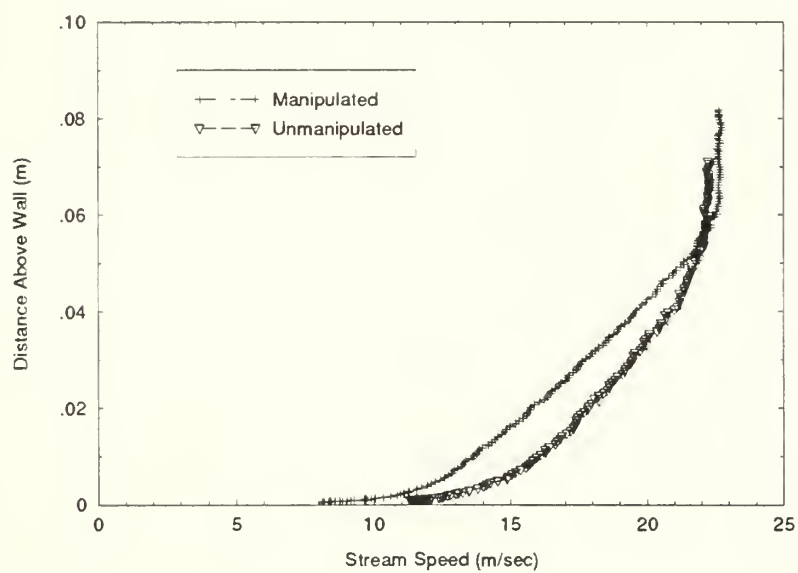


Figure A.2.9 Stream Velocity Profile Comparison ($x_{BLM}=150$ cm)

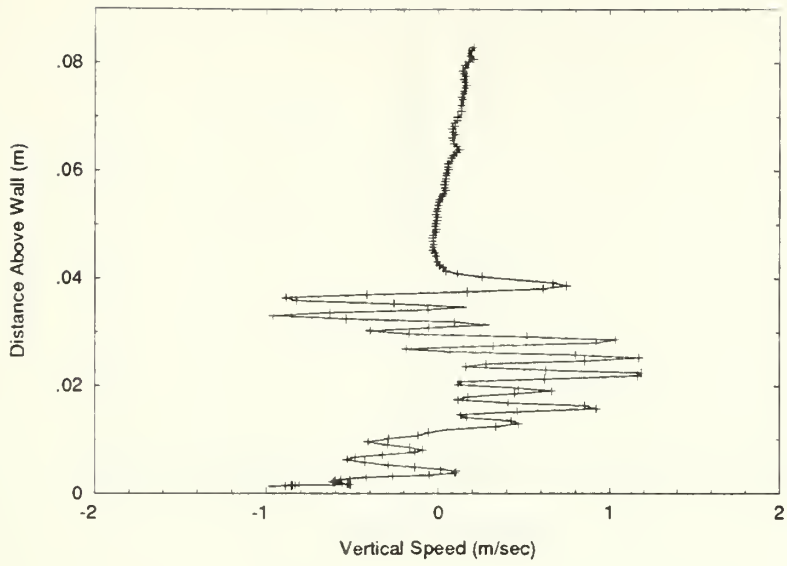


Figure A.2.10 Vertical Velocity Profile ($x_{BLM}=4$ cm)

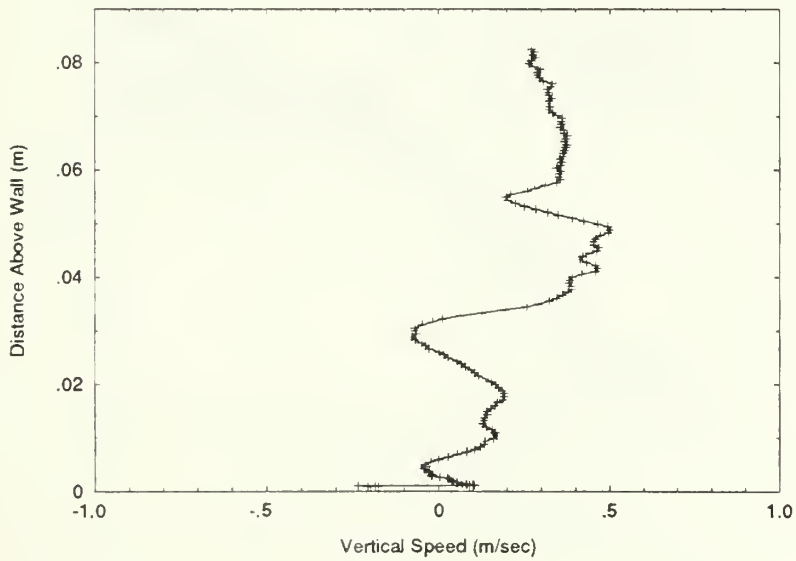


Figure A.2.11 Vertical Velocity Profile ($x_{BLM}=12$ cm)

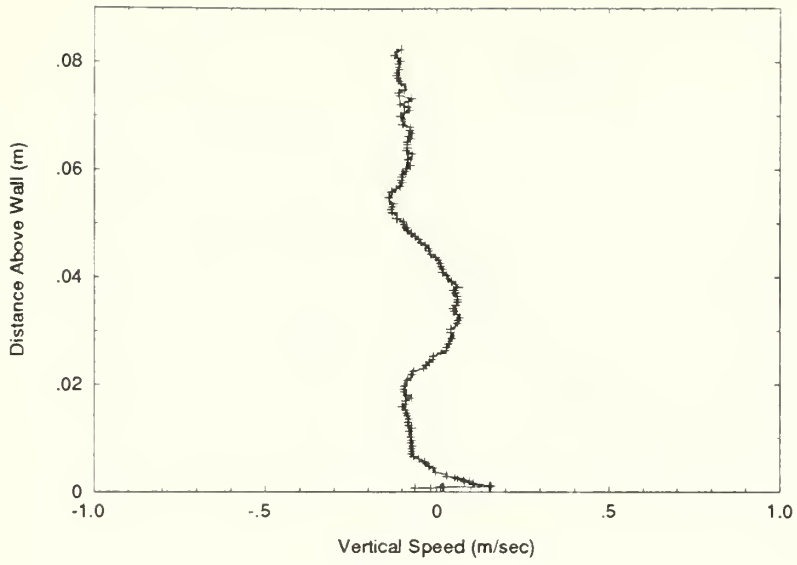


Figure A.2.12 Vertical Velocity Profile ($x_{BLM}=25$ cm)

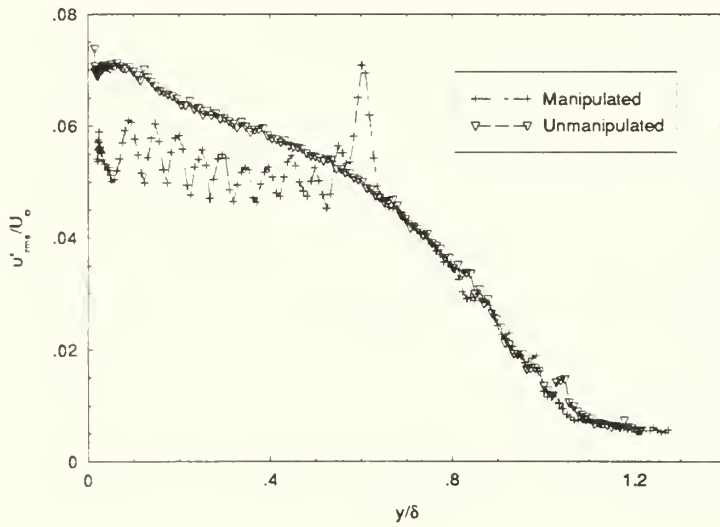


Figure A.2.13 $\frac{\sqrt{u'^2}}{U_{\infty}}$ vs $\frac{y}{\delta}$ ($x_{BLM}=4$ cm)

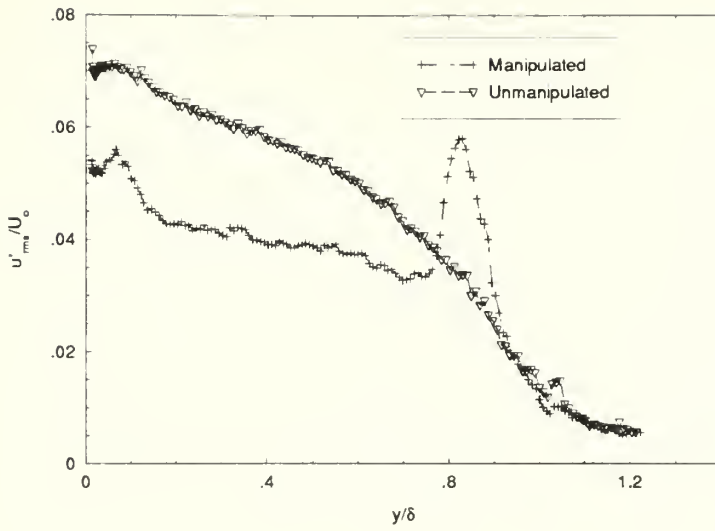


Figure A.2.14 $\frac{\sqrt{u'^2}}{U_{\infty}}$ vs $\frac{y}{\delta}$ ($x_{BLM}=12$ cm)

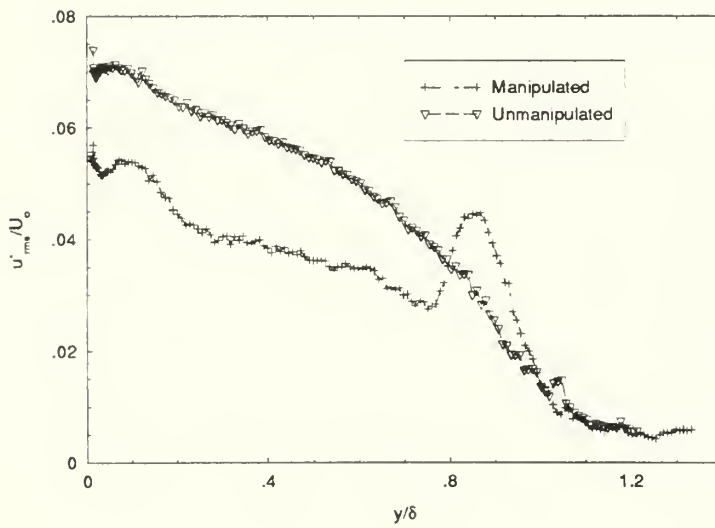


Figure A.2.15 $\frac{\sqrt{u'^2}}{U_{\infty}}$ vs $\frac{y}{\delta}$ ($x_{BLM}=25$ cm)

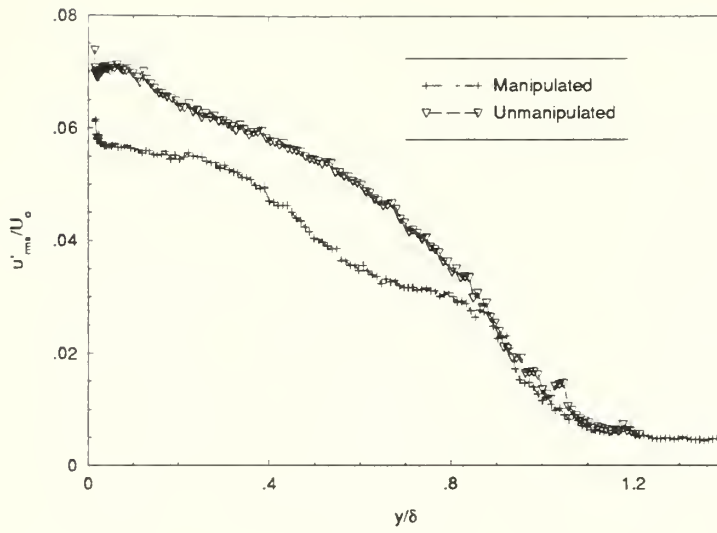


Figure A.2.16 $\frac{\sqrt{u'^2}}{U_0}$ vs $\frac{y}{\delta}$ ($x_{BLM}=65$ cm)

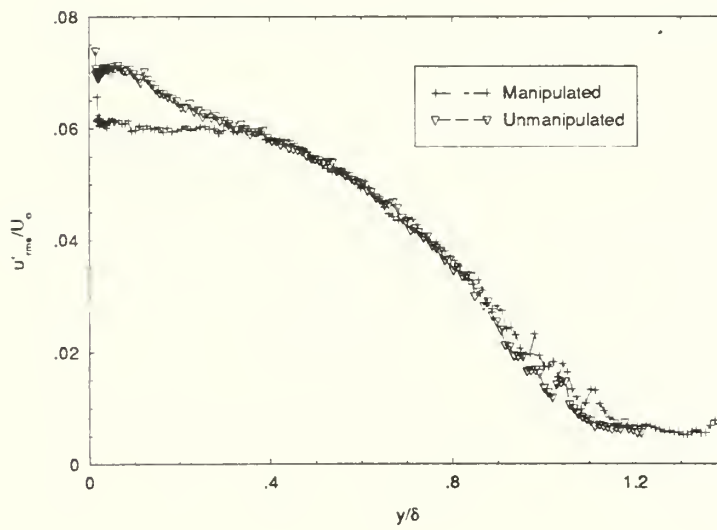


Figure A.2.17 $\frac{\sqrt{u'^2}}{U_0}$ vs $\frac{y}{\delta}$ ($x_{BLM}=100$ cm)

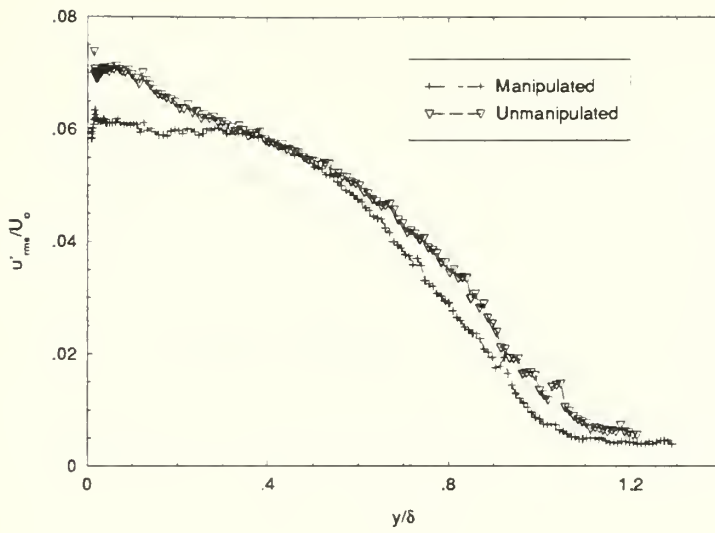


Figure A.2.18 $\frac{\sqrt{u'^2}}{U_\infty}$ vs $\frac{y}{\delta}$ ($x_{BLM}=150$ cm)

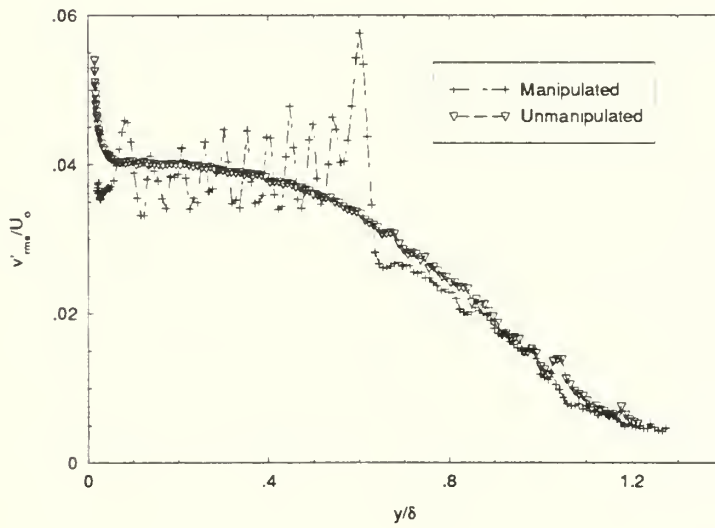


Figure A.2.19 $\frac{\sqrt{v'^2}}{U_\infty}$ vs $\frac{y}{\delta}$ ($x_{BLM}=4$ cm)

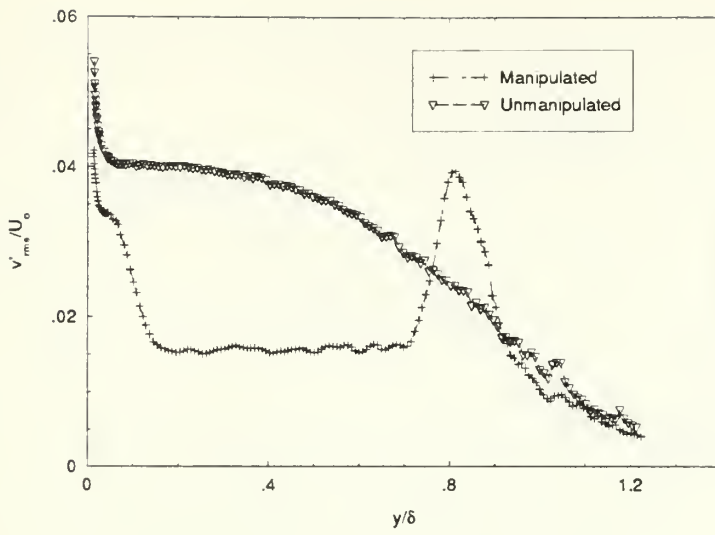


Figure A.2.20 $\frac{\sqrt{v'^2}}{U_\infty}$ vs $\frac{y}{\delta}$ ($x_{BLM}=12$ cm)

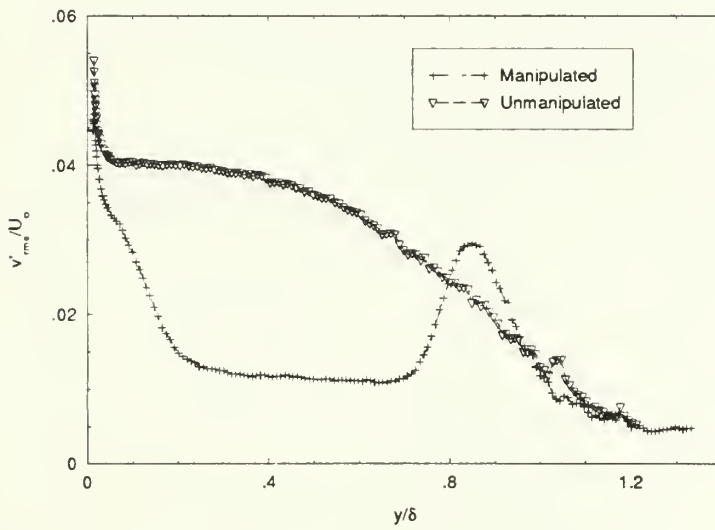


Figure A.2.21 $\frac{\sqrt{v'^2}}{U_\infty}$ vs $\frac{y}{\delta}$ ($x_{BLM}=25$ cm)

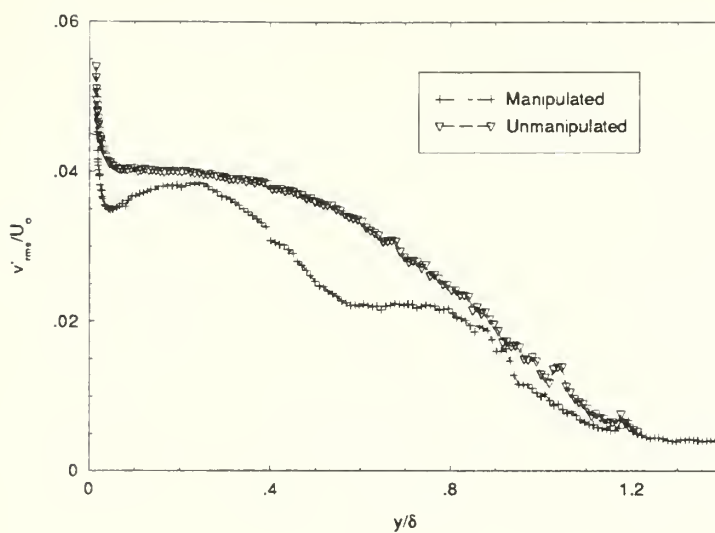


Figure A.2.22 $\frac{\sqrt{v'^2}}{U_\infty}$ vs $\frac{y}{\delta}$ ($x_{\text{BLM}}=65$ cm)

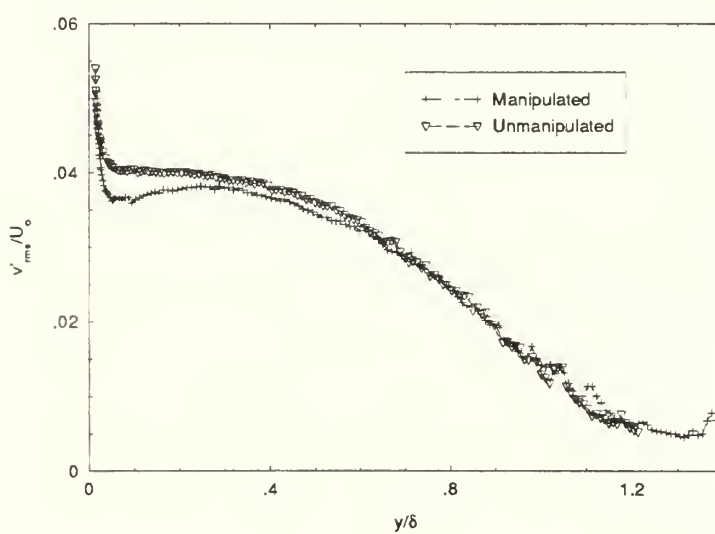


Figure A.2.23 $\frac{\sqrt{v'^2}}{U_\infty}$ vs $\frac{y}{\delta}$ ($x_{\text{BLM}}=100$ cm)

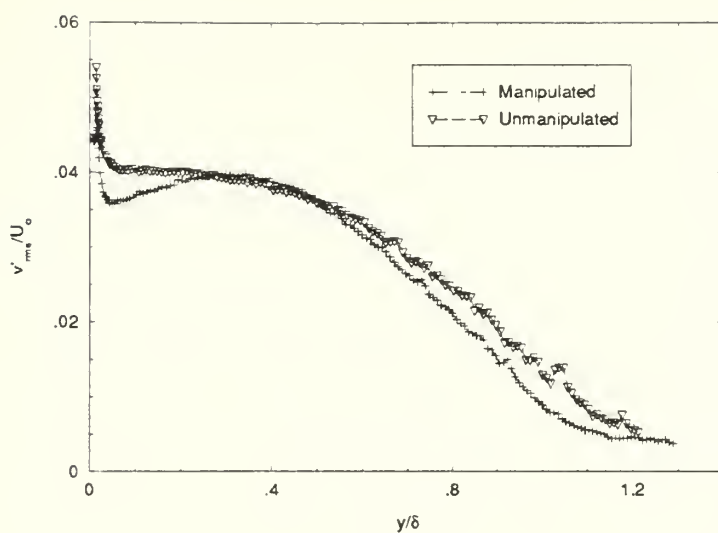


Figure A.2.24 $\frac{\sqrt{v'^2}}{U_\infty}$ vs $\frac{y}{\delta}$ ($x_{BLM}=150$ cm)

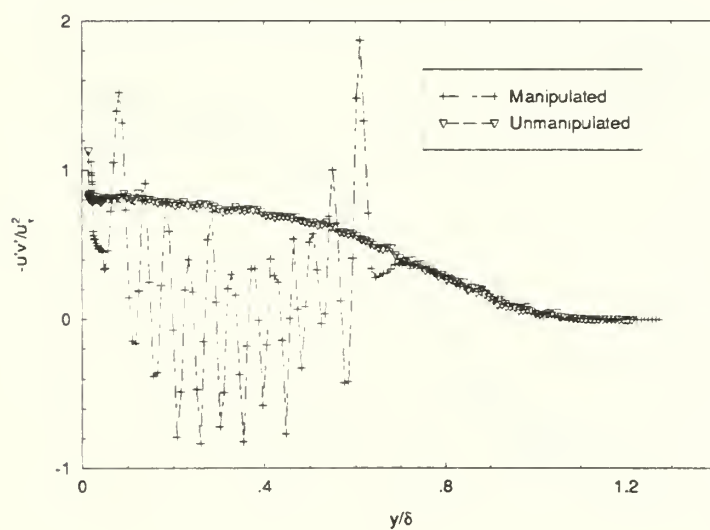


Figure A.2.25 $\frac{-\overline{u'v'}}{u_\tau^2}$ vs $\frac{y}{\delta}$ ($x_{BLM}=4$ cm)

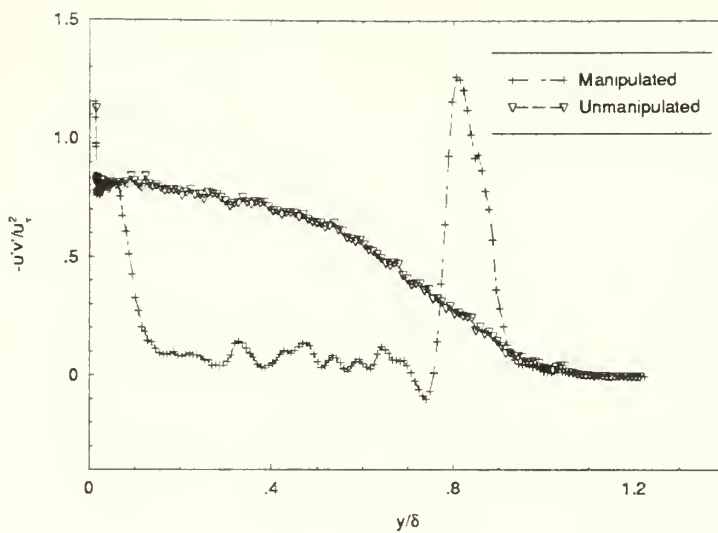


Figure A.2.26 $\frac{\overline{-u'v'}}{u_\tau^2}$ vs $\frac{y}{\delta}$ ($x_{\text{BLM}}=12$ cm)

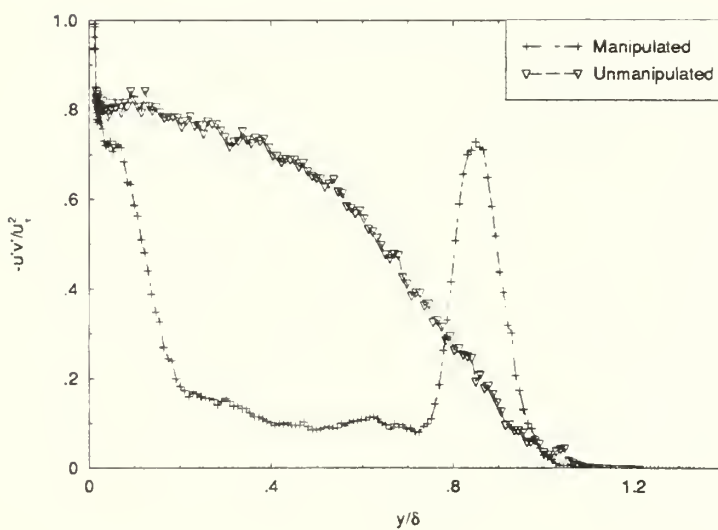


Figure A.2.27 $\frac{\overline{-u'v'}}{u_\tau^2}$ vs $\frac{y}{\delta}$ ($x_{\text{BLM}}=25$ cm)

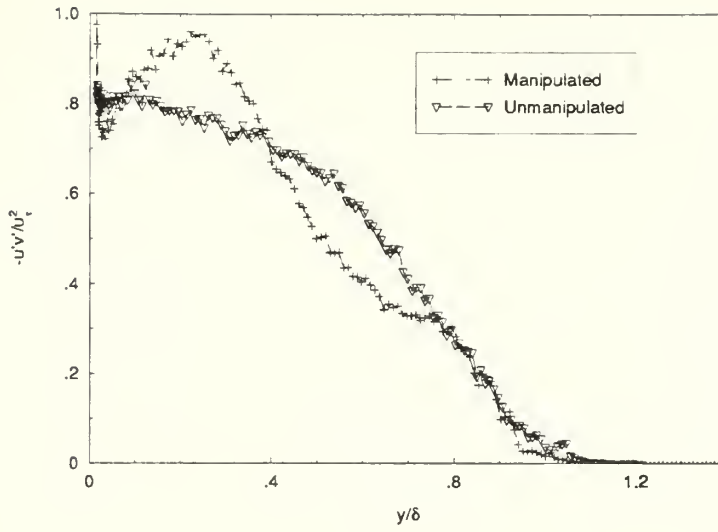


Figure A.2.28 $\frac{\overline{-u'v'}}{u_\tau^2}$ vs $\frac{y}{\delta}$ ($x_{\text{BLM}}=65$ cm)

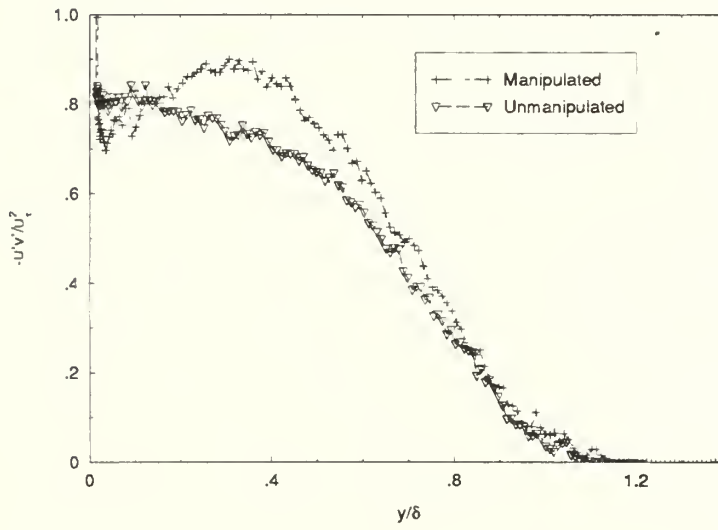


Figure A.2.29 $\frac{\overline{-u'v'}}{u_\tau^2}$ vs $\frac{y}{\delta}$ ($x_{\text{BLM}}=100$ cm)

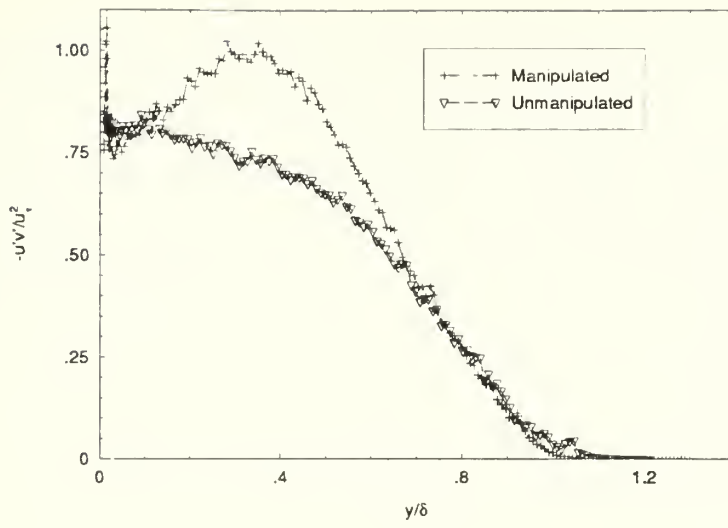


Figure A.2.30 $\frac{\overline{-u'v'}}{\mu_\tau^2}$ vs $\frac{y}{\delta}$ ($x_{\text{BLM}}=150$ cm)

Appendix B Tabular Data

Raw data collected for the calibration of the X-probe and the unmanipulated and manipulated turbulent boundary layers is not included in this document. The data is stored on floppy disks in the Acoustics and Vibrations Laboratory at the Massachusetts Institute of Technology. Copies of the data file disks are also held by the author and his thesis supervisor.

Appendix C Computer Programs

Computer programs for the collection and manipulation of X-probe data, including graphical representation, are found in this Appendix. All programs are in the FORTRAN computer language. The programs were run on the MASSCOMP UNIX system. The data acquisition program for surface gauge differential pressures is not included. Mr. Yuksel Gur of the Acoustics and Vibration Laboratory of the Massachusetts Institute of Technology courteously provided the program and gauge for use in the measurements. Subroutines formulated by Mr. Kay Herbert, also of the Acoustics and Vibrations Laboratory, for similar applications are included and referenced within the programs.

The programs are presented in the logical order of use. First the X-probe is calibrated and the two-dimensional polynomial linear least squares fits for u and v accomplished. The coefficients from these fits are used to transform X-probe instantaneous voltages into instantaneous velocities in the data acquisition program for the boundary layer. Statistics are performed in the data acquisition program to calculate mean velocities and rms values of both fluctuating components and the covariance of the fluctuating components, the Reynolds stress. The remaining programs use the output data of boundary layer measurements and the differential pressures from the surface differential pressure gauge to calculate boundary layer parameters and present the data in a format consistent with historical representations.

There are two separate programming paths to follow depending upon whether the boundary layer was manipulated or unmanipulated. If unmanipulated, the Coles fitting algorithm uses mean velocity profile data to determine both friction velocity, y -offset, and other parameters such as boundary layer displacement and momentum thicknesses. Then, differential pressures are used in conjunction with corresponding friction velocities to determine a calibration curve of wall shear stress as a function of differential pressure.

If manipulated data is obtained, the differential pressure gauge readings taken with each manipulated profile are averaged and used to determine friction velocity. The friction velocity is used in an interactive Coles fitting algorithm (visual slope matching of historical and measurement data) to determine y-offset of the manipulated data and subsequently other boundary layer parameters. In the plotting programs graphical profile representation corresponds to the format used by Klebanoff [9].

PROGRAM XVANGCAL: Data Acquisition of Calibration Voltages (X-probe) and Pitot Pressure (Converted to Velocity) at Each Calibration Angle

Input

Pitot gain
temperature
angle

Output

velocity-angle-voltage data files
(q- α -volt(1)-volt(2))
velocity-velocity-voltage data files
(u-v-volt(1)-volt(2))

```
c*****
c  This program collects pressure and voltage data
c  for an X-probe hot-wire pair placed in a stream.
c  One pressure (chan2) and two voltage channels
c  are used, and the pressure data is converted to
c  velocities. Data formatted into four columns
c  is placed into four output files, two in q-a format
c  and two in u-v format. Two output files are for
c  quick analysis to determine calibration coefficients.
c  These files eliminate low velocity data points where
c  mutual heat transfer between sensors distorts voltage
c  data. To include these points, the two other files
c  can be modified by eliminating non-entries.
c  All data acquisition terms are identified in the
c  MASSCOMP Data Acquisition Manual with example
c  programs provided.
c  Note: When preparing for data collection, ensure
c  that the X-probe is set to the correct angle and
c  small increments of increasing velocity are made
c  for the first few data points.
c
c  Frank Camelio September 1989
c*****
c  program xvangcal
c  include '/usr/include/mr.f'
c  integer RDWR, NEARFRQ, LOW, NOTUSED
c  integer NFRAMES, NCHAN
c  parameter (NFRAMES = 80000)
c  Number selected for NFRAMES can be increased if desired but
c  experience has shown that 80000 sample points are sufficient
c  for mean velocity data.
```



```

parameter (NCHAN = 3)
parameter (RDWR = 0)
parameter (NEARFRQ = 0)
parameter (FREQ = 8000.0)
parameter (BRSFRQ = 1000000.0)
parameter (LOW = 0)
parameter (NOTUSED = 0)
character frameclkdev*(*)
character burstclkdev*(*)
character addev*(*)
parameter (frameclkdev = '/dev/dacp0/clk0')
parameter (burstclkdev = '/dev/dacp0/clk1')
parameter (addev = '/dev/dacp0/adf0')
integer adpn, clkpn1, clkpn2, fchan, incr, gain
integer byteslocked
integer status(2)
integer*2 rawdata(NCHAN*NFRAMES)
real rfreq,rbrst
real*4 ang,q(25),ve1(25),ve2(25),pe(25),u(25),v(25)
c*****
c   ang=angle manually set for calibration velocity range
c   q=tunnel stream velocity
c   ve1=voltage measured from X-probe channel 1
c   ve2=voltage measured from X-probe channel 2
c   pe=voltage measure from Pitot (Validyne)
c       (converted to velocity for the output files)
c   u=q*cos(ang), velocity component parallel to probe axis
c   v=q*sin(ang), velocity component normal to probe axis
c       an parallel to probe support stem
c   Configured for a maximum of 25 velocity data points
c   for each angle set during the calibration.
c   For each angle step through 25 or less (recommend
c   12 minimum) RPM's (velocities) repeating the same
c   RPM's at the other angles.
c*****
character*10 date
common rawdata
data adpn /-1/
data clkpn1 /-1/
data clkpn2 /-1/
call mlock(0,0,byteslocked)
write(6,*) byteslocked, ' bytes locked in memory'
write(6,*)
c fmt = format files containing all determined parameters & text
open(8,FILE='xqacal.dat',STATUS='fresh')
open(85,FILE='xuvcal.dat',STATUS='fresh')
open(9,FILE='xqacal.fmt',STATUS='fresh')
open(95,FILE='xuvcal.fmt',STATUS='fresh')
write(9,1)
1  format(3x,'q-vel',4x,'angle',4x,'e1',5x,'e2')
write(9,2)
2  format(3x,'m/sec',5x,'rad',4x,'volts',3x,'volts')
write(9,*)
write(95,3)
3  format(3x,'u-vel',4x,'v-vel',4x,'e1',5x,'e2')
write(95,4)
4  format(3x,'m/sec',4x,'m/sec',3x,'volts',3x,'volts')
write(95,*)

```



```

write(6,*) 'chan2=pitot      chan0=hotwire_1'
write(6,*) 'chan1=hotwire_2'
fchan=0
write(6,*)
write(6,*) 'Enter date as a 10 character string (no spaces).'
read(5,*) date
write(6,*)
write(6,*) 'Input gain setting for pitot '
read(5,*) fgain
write(6,*)
write(6,*) 'Enter temperature in deg Fahrenheit.'
read(5,*) tempf
write(6,*)
temp=(tempf-32.)/1.8
rho=1.293/(1+.00367*temp)
l=0
vav1=0
vav2=0
5  k=1
   l=l+1
   write(6,*)
   write(6,*) 'Secure fan, reset RPM to 0, set traverse angle.'
   write(6,*) 'Enter angle setting of probe relative to the'
   write(6,*) 'stream flow ( + or - in degrees).'
   read(5,*) ang
   ang=ang*3.14159/180
   write(6,*)
   write(6,*) 'start at velocity=0 '
10  write(6,*) 'take data, re-set angle, or quit?'
   write(6,*) '( > 0 = data, 0=re-set, < 0 = quit) '
c*****
c  Each time re-set is chosen, values for a given calibration
c  run are written to file and the angle must be changed.
c  After calibration on final angle setting, enter -1 to
c  write to file and terminate program.
c*****
   read(5,*) connum
   if (connum.le.0) goto 25
   write(6,*)
   call mopen(adpn,addev,RDWR)
   call mopen(clkpn1,frameclkdev,RDWR)
   call mopen(clkpn2,burstclkdev,RDWR)
   call mrclk2(clkpn1, clkpn2, NOTUSED, NEARFRQ, FREQ,
&  rfreq, NEARFRQ, BRSFRQ, rbrst, NCHAN, LOW)
   write(6,*) 'freq for clk6 = ',rfreq
   write(6,*) 'freq for clk7 = ',rbrst
   incr=1
   gain=0
   call mradxin(adpn,clkpn1,clkpn2,fchan,NCHAN,incr,gain,
&  NFRAMES,rawdata)
   write(6,*) 'transfer starting ....'
   call mrevwt(adpn,status,80000)
   write(6,*) 'transfer complete'
   call mrclosall
c The following terms are pressure, velocity rawdata voltage sums.
   pvol=0.
   vvol1=0.
   vvol2=0.
   do 20 i=1,NFRAMES*NCHAN-2,3
     vvol1=vvol1+float(rawdata(i))
     vvol2=vvol2+float(rawdata(i+1))
20  pvol=pvol+float(rawdata(i+2))

```



```

pe(k)=pvol*.00244141/float(NFRAMES)/fgain
ve1(k)=vvol1*.00244141/float(NFRAMES)
ve2(k)=vvol2*.00244141/float(NFRAMES)
c The following line grouping is entered to detect problems in the
c course of calibration. Calibration is conducted from low to
c high values of pressure and velocity. If a voltage on any
c channel is less than a preceding voltage measurement, the
c appropriate warning is sent to screen. For example, hot-wire
c resistance changes can indicate a potential failure, or more
c commonly at low velocities near zero, the flow may not have
c stabilized and pitot voltage is erratic.
write(6,*)
write(6,*) pe(k),ve1(k),ve2(k)
write(6,*)
if(k.gt.1) then
  if(pe(k).lt.pe(k-1)) then
    write(6,*) 'CAUTION: RE-SETTING - P VALUE < PRECEDING'
    l=l-1
    goto 5
  endif
  if(ve1(k).lt.ve1(k-1)) then
    write(6,*) 'CAUTION: RE-SETTING - V1 VALUE < PRECEDING'
  endif
  if(ve2(k).lt.ve2(k-1)) then
    write(6,*) 'CAUTION: RE-SETTING - V2 VALUE < PRECEDING'
    l=l-1
    goto 5
  endif
endif
k=k+1
goto 10
25 pe0=pe(1)
k=k-1
do 30 j=1,k
ccc Set zero offset for pressure at each calibration angle.
pe(j)=pe(j)-pe0
q(j)=sqrt(19.614*pe(j)/rho)
u(j)=q(j)*cos(ang)
v(j)=q(j)*sin(ang)
if(j.eq.1.or.q(j).lt.1.5) goto 28
write(8,*) q(j),ang,ve1(j),ve2(j)
write(85,*) u(j),v(j),ve1(j),ve2(j)
write(6,*) q(j),ang,ve1(j),ve2(j)
28 write(9,*) q(j),ang,ve1(j),ve2(j)
30 write(95,*) u(j),v(j),ve1(j),ve2(j)
vav1=vav1+ve1(1)
vav2=vav2+ve2(1)
if (connum.eq.0) goto 5
if (connum.lt.0) goto 50
50 vav1=vav1/l
vav2=vav2/l
write(6,*) 0.0,0.0,vav1,vav2
write(8,*) 0.0,0.0,vav1,vav2
write(85,*) 0.0,0.0,vav1,vav2
write(9,*)
write(9,*)
c The average zero velocity voltage is calculated for info only.
write(9,*) 'eav1(0)=' ,vav1, ' eav2(0)=' ,vav2
write(9,*) 'Ch0=pitot Ch1=hotwire1 Ch2=hotwire2'
write(9,*) 'Pitot gain = ',fgain
write(9,*) 'Temp (F) = ',tempf
write(9,*) 'Date: ',date

```



```

write(9,*) 'Filename: xqacal.fmt'
write(95,*)
write(95,*)
write(95,*) 'eav1(0)=',vav1,' eav2(0)=',vav2
write(95,*) 'Ch0=pitot Ch1=hotwire1 Ch2=hotwire2'
write(95,*) 'Pitot gain = ',fgain
write(95,*) 'Temp (F) = ',tempf
write(95,*) 'Date: ',date
write(95,*) 'Filename: xuvcal.fmt'
close(8)
close(85)
close(9)
close(95)
stop
end

```

c*****

PROGRAM XCOEFF:

Linear Least Squares Fit of Velocity - Angle Calibration Data to Determine Coefficients of a Two-Dimensional Polynomial Representation u and v or Q and $.$

Input

data file name
data file type
number of coefficients

Output

coefficients files
coefficients and error files

c*****

c This program reads velocity-angle-voltage data or stream
c and vertical velocity data and fits separately a double
c polynomial surface, one in velocity and one in angle OR
c one in u-velocity and one in v-velocity, to voltage data
c on both channels of an X-probe. The data is obtained from
c a calibration which pivots the probe at different positive
c and negative angles with respect to the free stream.
c Polynomial order is either 3, giving 16 coefficients, or
c 4, giving 25 coefficients.
c The 2-d polynomial format is:

```

c      N N
c      f(e1,e2)=SUM SUM a(i,j)*e1**(j-1)*e2**(i-1) [N=4 or 5]
c      i=1 j=1

```

c where e1,e2 are channel voltages and a(i,j) are the fitted
c coefficients. For simplicity in analysis coefficients are
c transferred to vector format vice an array.

c*****

```

program xcoeff
implicit real*8 (a-h,o-z)
real*8 qu(200,1),av(200,1)
real*8 quest(200),qudel(200),avest(200),avdel(200)
real*8 etqu(25,1),etav(25,1),qufest(200),avfest(200)
real*8 ee(200,25),eet(25,200),ete(25,25)
real*8 qumaxerr,quaverr,qusumerr,quvarsum,quvar
real*8 avmaxerr,avaverr,avsumerr,avvarsum,avvar
real*8 qurel(200),avrel(200)

```

c*****

c qu=q or u velocity obtained from calibration file
c av=angle or v velocity obtained from calibration file
c ...err=error terms in comparing fitted to measured values


```

c ...sum=term used in determining avg error
c ...rel=relative error term
c ...del=difference term
c ...fest=term estimated after functional calculation
c ...est=estimated term from least squares fit
c ee=two channel voltage product in polynomial
c eet,ete,etqu,etav=arrays of voltages and velocities used
c           in matrix multiplication (t=transpose)
c qu16,qu25=resulting functions for calculating q or u
c av16,av25=resulting functions for calculating angle or velocity
c ao,bo=coefficients for qu and av functions respectively
c*****
character*15 name,fileout1,fileout2
common /arry/ xx(25,27),ix(25)
common /xco/ e1(200),e2(200)
common /funcalc/ ao(25),bo(25)
real qu16,av16,qu25,av25
external qu16,av16,qu25,av25
50  write(6,*) 'Enter name of calibration data file.'
    read(5,*) name
    write(6,*)
c*****
c READ VALUES FROM Q-A OR U-V CALIBRATION .DAT FILE
c*****
    open(51,file=name,status='old')
    m=1
100  read(51,*,end=150) qu(m,1),av(m,1),e1(m),e2(m)
    m=m+1
    goto 100
150  close(51)
    m=m-1
    write(6,*) 'Enter 1 if data is q-a, 2 if u-v.'
    read(5,*) num2
    write(6,*)
200  write(6,*) 'Enter # of coefficients to fit (INTEGER).'
    read(5,*) num1
    write(6,*)
    if (num1.eq.16.and.num2.eq.1) then
        fileout1='x16coqa.dat'
        fileout2='x16coqa.fmt'
    endif
    if (num1.eq.16.and.num2.eq.2) then
        fileout1='x16couv.dat'
        fileout2='x16couv.fmt'
    endif
    if (num1.eq.25.and.num2.eq.1) then
        fileout1='x25coqa.dat'
        fileout2='x25coqa.fmt'
    endif
    if (num1.eq.25.and.num2.eq.2) then
        fileout1='x25couv.dat'
        fileout2='x25couv.fmt'
    endif
    open(7,file=fileout1,status='fresh')
    open(8,file=fileout2,status='fresh')
    if(num2.eq.1) write(8,*) ' q coeff', ' a coeff'
    if(num2.eq.2) write(8,*) ' u coeff', ' v coeff'
300  if (num1.eq.16) call coeff16(m,ee)
    if (num1.eq.25) call coeff25(m,ee)
    do 400 i=1,m
        do 400 j=1,num1
400  eet(j,i)=ee(i,j)

```



```

call matmlt(eet,ee,ete,num1,m,num1)
call matmlt(eet,qu,etqu,num1,m,1)
call matmlt(eet,av,etav,num1,m,1)
do 500 i=1,num1
  do 500 j=1,num1
500  xx(i,j)=ete(i,j)
  do 600 i=1,num1
    xx(i,num1+1)=etqu(i,1)
600  xx(i,num1+2)=etav(i,1)
  call algr(num1,2,1,e)
  do 700 i=1,num1
    ao(i)=xx(i,num1+1)
    bo(i)=xx(i,num1+2)
    write(6,*) ao(i),bo(i)
    write(7,*) ao(i),bo(i)
700  write(8,*) ao(i),bo(i)
    write(8,*)
    write(8,*)
  close(7)
c*****
c  ERROR ANALYSIS
c*****
  write(8,*)
  if(num2.eq.1) then
    write(8,*) ' q-act ', ' q-fit ', 'q-funct '
    &,' delta-q', ' q rel err'
  endif
  if(num2.eq.2) then
    write(8,*) ' u-act ', ' u-fit ', 'u-funct '
    &,' delta-u', ' u rel err'
  endif
  do 800 i=1,m
    if(num1.eq.16) qufest(i)=qu16(e1(i),e2(i))
    if(num1.eq.25) qufest(i)=qu25(e1(i),e2(i))
    quest(i)=0
    do 750 j=1,num1
750  quest(i)=quest(i)+ao(j)*ee(i,j)
    qudel(i)=qu(i,1)-quest(i)
    if(qu(i,1).eq.0.) then
      qurel(i)=0.
    else
      qurel(i)=100*qudel(i)/qu(i,1)
    endif
    if(qurel(i).eq.0.) then
      write(8,760) qu(i,1),quest(i),qufest(i),qudel(i)
760  format(4f9.5,3x)
    else
      write(8,770) qu(i,1),quest(i),qufest(i),qudel(i),qurel(i)
770  format(5f9.5,3x)
    endif
    if(i.eq.1) qumaxerr=abs(qudel(i))
    qumaxerr=max(abs(qudel(i)),qumaxerr)
800  continue
    write(8,*)
    qusumerr=0
    do 900 i=1,m
900  qusumerr=qusumerr+abs(qudel(i))
    quaverr=qusumerr/dbl(m)
    quvarsum=0
    do 1000 i=1,m
1000  quvarsum=quvarsum+(abs(qudel(i))-quaverr)**2
    quvar=quvarsum/dbl(m)

```



```

write(8,*)
if(num2.eq.1) then
  write(8,*) 'Max q vel error magnitude (m/sec) = ',qumaxerr
  write(8,*) 'Avg q vel error magnitude (m/sec) = ',quaverr
  write(8,*) 'Var q vel error magnitude (m/sec) = ',quvar
endif
if(num2.eq.2) then
  write(8,*) 'Max u vel error magnitude (m/sec) = ',qumaxerr
  write(8,*) 'Avg u vel error magnitude (m/sec) = ',quaverr
  write(8,*) 'Var u vel error magnitude (m/sec) = ',quvar
endif
write(8,*)
write(8,*)
if(num2.eq.1) then
  write(8,*) ' a-act ', ' a-fit ', ' a-funct', ' delta-a'
  &,' a rel err'
endif
if(num2.eq.2) then
  write(8,*) ' v-act ', ' v-fit ', ' v-funct', ' delta-v'
  &,' v rel err'
endif
do 1100 i=1,m
  if(num1.eq.16) avfest(i)=av16(e1(i),e2(i))
  if(num1.eq.25) avfest(i)=av25(e1(i),e2(i))
  avest(i)=0
  do 1050 j=1,num1
1050   avest(i)=avest(i)+bo(j)*ee(i,j)
  avdel(i)=av(i,1)-avest(i)
  if(av(i,1).eq.0.) then
    avrel(i)=0.
  else
    avrel(i)=100*avdel(i)/av(i,1)
  endif
  if(avrel(i).eq.0.) then
    write(8,760) av(i,1),avest(i),avfest(i),avdel(i)
  else
    write(8,770) av(i,1),avest(i),avfest(i),avdel(i),avrel(i)
  endif
  if(i.eq.1) avmaxerr=abs(avdel(i))
  avmaxerr=max(abs(avdel(i)),avmaxerr)
1100 continue
  write(8,*)
  avsumerr=0
  do 1200 i=1,m
1200   avsumerr=avsumerr+abs(avdel(i))
  avaverr=avsumerr/dbble(m)
  avvarsum=0
  do 1300 i=1,m
1300   avvarsum=avvarsum+(abs(avdel(i))-avaverr)**2
  avvar=avvarsum/dbble(m)
  write(8,*)
  if(num2.eq.1) then
    write(8,*) 'Max ang error magnitude (rad) = ',avmaxerr
    write(8,*) 'Avg ang error magnitude (rad) = ',avaverr
    write(8,*) 'Var ang error magnitude (rad) = ',avvar
  endif
  if(num2.eq.2) then
    write(8,*) 'Max v vel error magnitude (m/sec) = ',avmaxerr
    write(8,*) 'Avg v vel error magnitude (m/sec) = ',avaverr
    write(8,*) 'Var v vel error magnitude (m/sec) = ',avvar
  endif
  write(8,*)

```



```

write(6,*) 'Enter 3 to change # coefficients.'
write(6,*) 'Enter 4 to change q-a to u-v or vice-versa.'
write(6,*) 'Else enter any other integer.'
read(5,*) num3
write(6,*)
if(num3.eq.3) goto 200
if(num3.eq.4) goto 50
close(8)
stop
end
c*****
c  SUBROUTINES - PRODUCTS OF VOLTAGES (16 AND 25 COEFF's)
c*****
      subroutine coeff16(m,ee)
      implicit real*8 (a-h,o-z)
      dimension ee(200,25)
      common /xco/ e1(200),e2(200)
      do 10 i=1,m
         ee(i,1)=1
         ee(i,2)=e1(i)
         ee(i,3)=e1(i)*e1(i)
         ee(i,4)=e1(i)*ee(i,3)
         ee(i,5)=e2(i)
         ee(i,6)=e2(i)*e1(i)
         ee(i,7)=e2(i)*ee(i,3)
         ee(i,8)=e2(i)*ee(i,4)
         ee(i,9)=e2(i)*e2(i)
         ee(i,10)=e2(i)*ee(i,6)
         ee(i,11)=e2(i)*ee(i,7)
         ee(i,12)=e2(i)*ee(i,8)
         ee(i,13)=e2(i)*ee(i,9)
         ee(i,14)=e2(i)*ee(i,10)
         ee(i,15)=e2(i)*ee(i,11)
         ee(i,16)=e2(i)*ee(i,12)
10    continue
      return
      end
c*****
      subroutine coeff25(m,ee)
      implicit real*8 (a-h,o-z)
      dimension ee(200,25)
      common /xco/ e1(200),e2(200)
      do 10 i=1,m
         ee(i,1)=1
         ee(i,2)=e1(i)
         ee(i,3)=e1(i)*e1(i)
         ee(i,4)=e1(i)*ee(i,3)
         ee(i,5)=e1(i)*ee(i,4)
         ee(i,6)=e2(i)
         ee(i,7)=e2(i)*e1(i)
         ee(i,8)=e2(i)*ee(i,3)
         ee(i,9)=e2(i)*ee(i,4)
         ee(i,10)=e2(i)*ee(i,5)
         ee(i,11)=e2(i)*ee(i,6)
         ee(i,12)=e2(i)*ee(i,7)
         ee(i,13)=e2(i)*ee(i,8)
         ee(i,14)=e2(i)*ee(i,9)
         ee(i,15)=e2(i)*ee(i,10)
         ee(i,16)=e2(i)*ee(i,11)
         ee(i,17)=e2(i)*ee(i,12)
         ee(i,18)=e2(i)*ee(i,13)
         ee(i,19)=e2(i)*ee(i,14)

```



```

        ee(i,20)=e2(i)*ee(i,15)
        ee(i,21)=e2(i)*ee(i,16)
        ee(i,22)=e2(i)*ee(i,17)
        ee(i,23)=e2(i)*ee(i,18)
        ee(i,24)=e2(i)*ee(i,19)
        ee(i,25)=e2(i)*ee(i,20)
10    continue
    return
end
c*****
c  SUBROUTINES - MATRIX MULTIPLICATION, SIMUL EQN SOLUTION
c  (see Camahan, Applied Numerical Methods, Chapter 4)
c*****
    subroutine matmlt(aa,u,t,mm,nn,pp)
    real*8 aa(25,200),u(200,25),t(25,25)
    integer pp
    do 1 i=1,mm
        do 1 j=1,pp
1      t(i,j)=0
        do 2 i=1,mm
            do 2 j=1,pp
                do 2 k=1,nn
2          t(i,j)=aa(i,k)*u(k,j)+t(i,j)
        return
    end
c*****
c  algr solve a real algebraic system
c
c  id=1: reduce, solve for nr right hand sides
c  id=0, nr>0: solve for nr right hand sides
c  id=0, nr=0: wielandt correction step
c  id=-1: reduce, first wielandt step
c
c      Kay Herbert 1987
c*****
    subroutine algr(n,nr,id,e)
    implicit real*8 (a-h,o-z)
    common /array/ a(25,27),ix(25)

    m=n+nr
    m1=n-1
    n1=n+1
    if (id.eq.0) go to 10
    do 1 k=1,m1
        xx=0.
        kx=k
        do 2 kk=k,n
            x=dabs(a(kk,k))
            if (x.le.xx) go to 2
            xx=x
            kx=kk
2      continue
        ix(k)=kx
        if (kx.eq.k) go to 3
        do 4 jj=k,m
            z=a(k,jj)
            a(k,jj)=a(kx,jj)
4          a(kx,jj)=z
3      continue
        k1=k+1
        do 1 kk=k1,n
            if (dabs(a(k,k)).le.0.) go to 1

```



```

      a(kk,k)=a(kk,k)/a(k,k)
      do 5 jj=k1,m
5      a(kk,jj)=a(kk,jj)-a(kk,k)*a(k,jj)
1      continue
      if (id.gt.0) go to 12

      a(n,n1)=1.
      do 6 kk=1,m1
      k=n-kk
      a(k,n1)=-a(k,n)
      if (k.eq.m1) go to 6
      k1=k+1
      do 7 l=k1,m1
7      a(k,n1)=a(k,n1)-a(k,l)*a(l,n1)
6      a(k,n1)=a(k,n1)/a(k,k)
      return

10     if (nr.le.0) m=n1
      do 11 l=n1,m
      do 11 k=1,m1
      kx=ix(k)
      z=a(k,l)
      a(k,l)=a(kx,l)
      a(kx,l)=z
      k1=k+1
      do 11 kk=k1,n
11     a(kk,l)=a(kk,l)-a(kk,k)*a(k,l)
      if (nr.gt.0) go to 12

      e=a(n,n)/a(n,m)
      do 13 k=1,n
13     a(k,m)=e*a(k,m)

12     if (m.le.n) return
      do 14 kk=1,n
      k=n1-kk
      if (k.eq.n) go to 15
      k1=k+1
      do 20 l=n1,m
      do 20 ll=k1,n
20     a(k,l)=a(k,l)-a(k,ll)*a(ll,l)
15     do 14 l=n1,m
14     a(k,l)=a(k,l)/a(k,k)
      return
      end
c*****
c  FUNCTIONS TO CONVERT VOLTAGES TO VELOCITY AND ANGLE
c*****
      function qu16(v1,v2)
      implicit real*8 (e,f,v)
      common /funcalc/ e(25),f(25)
      qu16=e(1)+v1*(e(2)+v1*(e(3)+v1*e(4)))+
&v2*(e(5)+v1*(e(6)+v1*(e(7)+v1*e(8)))+
&v2*(e(9)+v1*(e(10)+v1*(e(11)+v1*e(12)))+
&v2*(e(13)+v1*(e(14)+v1*(e(15)+v1*e(16))))))
      return
      end
c*****
      function av16(v1,v2)
      implicit real*8 (e,f,v)
      common /funcalc/ e(25),f(25)

```



```

    av16=f(1)+v1*(f(2)+v1*(f(3)+v1*f(4)))+
    &v2*(f(5)+v1*(f(6)+v1*(f(7)+v1*f(8)))+
    &v2*(f(9)+v1*(f(10)+v1*(f(11)+v1*f(12)))+
    &v2*(f(13)+v1*(f(14)+v1*(f(15)+v1*f(16))))))
    return
end
c*****
function qu25(v1,v2)
implicit real*8 (g,h,v)
common /funcalc/ g(25),h(25)
qu25=g(1)+v1*(g(2)+v1*(g(3)+v1*(g(4)+v1*g(5)))+
&v2*(g(6)+v1*(g(7)+v1*(g(8)+v1*(g(9)+v1*g(10)))+
&v2*(g(11)+v1*(g(12)+v1*(g(13)+v1*(g(14)+v1*g(15)))+
&v2*(g(16)+v1*(g(17)+v1*(g(18)+v1*(g(19)+v1*g(20)))+
&v2*(g(21)+v1*(g(22)+v1*(g(23)+v1*(g(24)+v1*g(25)))))))))
return
end
c*****
function av25(v1,v2)
implicit real*8 (g,h,v)
common /funcalc/ g(25),h(25)
av25=h(1)+v1*(h(2)+v1*(h(3)+v1*(h(4)+v1*h(5)))+
&v2*(h(6)+v1*(h(7)+v1*(h(8)+v1*(h(9)+v1*h(10)))+
&v2*(h(11)+v1*(h(12)+v1*(h(13)+v1*(h(14)+v1*h(15)))+
&v2*(h(16)+v1*(h(17)+v1*(h(18)+v1*(h(19)+v1*h(20)))+
&v2*(h(21)+v1*(h(22)+v1*(h(23)+v1*(h(24)+v1*h(25)))))))))
return
end
c*****

```

PROGRAM XTBLDATACQ: Boundary Layer Data Acquisition Program Utilizing an X-probe and Two-Dimensional Polynomial Calibration Functions -- Outputs Mean, Fluctuating, and Reynolds Stress Velocity Values at Each Measurement Position in the Boundary Layer

Input

coefficients file name
temperature
stream location
traverse control options
maximum distance from wall
stream velocity estimate

Output

output data file
distance from wall
mean stream velocity
mean vertical velocity
rms stream fluctuating velocity
rms vertical fluctuating velocity
Reynolds stress (velocity product)

```

c*****
c This program collects tbl data using an x-probe calibrated
c with a 25 coefficient polynomial surface (voltage). No angle
c correction is used in the calculations. A multi-loop procedure
c is employed where rawdata is transferred to a different
c variable name so that data acquisition and calculations can be
c simultaneously performed. Calculational speed is improved by
c using statistical techniques to determine fluctuating values.
c Note the references to gain using the A/D converter on the
c MASSCOMP. Program readily adjusted to use 16 coefficients.
c*****
program xtblatacq

```



```

include '/usr/include/mr.f'
integer RDWR,NEARFRQ,LOW,NOTUSED
integer NFRAMES,NCHAN,RANGE
real FREQ,BRSRFQ
parameter (RDWR=0)
parameter (NEARFRQ=0)
parameter (FREQ=8000.0)
parameter (BRSRFQ=1000000.0)
parameter (LOW=0)
parameter (NOTUSED=0)
parameter (NFRAMES=10000)
parameter (NCHAN=2)
c*****
c  A/D CONVERTER RANGE IS SET FROM 0 TO +10 VOLTS BY THE
c  THE FOLLOWING PARAMETER STATEMENT. TO CHANGE, SEE
c  DATA ACQUISITION MANUAL UNDER "MRADLAN" AND RE-COMPILE.
c*****
parameter (RANGE=1)
character frameclkdev*(*)
character burstclkdev*(*)
character addev*(*)
character*15 fname
parameter (frameclkdev='/dev/dacp0/clk0')
parameter (burstclkdev='/dev/dacp0/clk1')
parameter (addev = '/dev/dacp0/adf0')
integer adpn,clkpn1,clkpn2,fchan,incr,gain
integer byteslocked
integer status(2)
integer*2 rawdata(NCHAN*NFRAMES)
integer*2 rawdat1(NCHAN*NFRAMES)
integer*2 cgarray (2,NCHAN)
real rfreq,rbrst
common rawdata
common /ufunct25/ za(25)
common /vfunct25/ zb(25)
external u25,v25
c*****
c  TRAVERSE AND PLOTTING INITIALIZATION AND ALIGNMENT
c*****
c traverse control
integer count_clk(2),int_clk,clkpath0,clkdapn
integer intco,numcal
integer*4 tcount,tcount1
integer*4 istep
integer*2 counterval(4)
c plotting
character*30 lp1,lp2,lp3
character*10 ln1,ln2,ln3
real*4 x1(300),y1(300),x2(300)
integer*4 gls(1000)
common /plot2/ gls,ymaxx,umaxx
c traverse
common /wncom/ counterval
external bwintsr
data clkpath0 /-1/
data clkdapn /-1/
data count_clk(1) /-1/
data count_clk(2) /-1/
data int_clk /-1/
data tcount /0/
data istep /0/
data adpn /-1/

```



```

data clkpn1 /-1/
data clkpn2 /-1/
c*****
c  DC GAIN IS SET TO 4 BY THE FOLLOWING DATA STATEMENT.  SEE
c  DATA ACQUISITION MANUAL UNDER "MRADLAN".
c*****
data carray /1,2,2,2/
call system(`/etc/loadacp 0`)
call mlock(0.0,byteslocked)
write(6,*) byteslocked,' bytes locked in memory'
call mopen(clkpath0,'/dev/dacp0/clk4',0)
call mrclocksetter(clkpath0,15,5,3,0,0,2,8)
call mrclockarm(1,clkpath0)
c plotting
lp1='X-PROBE TBL VELOCITIES'
lp2='y (in)'
lp3='uy 10*sqrt(uprms) (m/s)'
lps1='VELOCITY AUTO-SPECTRUM'
open(8,file='xtbldatacq.dat',status='fresh')
c*****
c  READ CALIBRATION DATA FILE
c*****
write(6,*) 'Enter name of (25) coefficients file.'
read(5,*) fname
write(6,*)
open(51,file=fname,status='old')
do 50 i=1,25
  read(51,*) za(i),zb(i)
50 continue
close(51)
c*****
c  INITIALIZE AND COLLECT RAW DATA
c*****
write(6,*)
write(6,*) 'Enter temperature (F) = ? '
read(5,*) tempf
write(6,*)
write(6,*) 'Ensure probe calibration temperature and test'
write(6,*) 'temperature are within +/- 3F. Else RECALIBRATE'
write(6,*)
write(6,*) 'Put traverse in desired x-location'
write(6,*) 'Enter x-location (in).'
read(5,*) xposi
write(6,*)
write(6,*)
write(6,*) 'Ensure the following electrical set-up:'
write(6,*) 'Chan0=HotWire1-dc  Chan1=HotWire2-dc'
write(6,*)
c traverse
call mopen(count_clk(1),'/dev/dacp0/clk6',0)
call mopen(count_clk(2),'/dev/dacp0/clk5',0)
call mopen(clkdapn,'/dev/dacp0/clkda3',0)
call mopen(int_clk,'/dev/dacp0/clk7',0)
thresh=2.0
call mrclockdaset(clkdapn,thresh)
idd = 0
iplot = 1
tcount=0
tcount1=0
ibuff=1

```



```

fchan=16
incr=1
c DC gain is set by data statement for cgarrray. If changed, the
c following statement must be changed.
gain=2
if(gain.eq.0) dcgain=1.
if(gain.eq.1) dcgain=2.
if(gain.eq.2) dcgain=4.
140 write(6,*) 'maximum y measurement ? y= ?'
read(5,*) ymaxx
if (ymaxx.gt.4.8) goto 140
write(6,*) 'y - max = ',ymaxx
write(6,*)|

c If one desires to use the traverse in manual mode enter a value
c for ytravmax a distance above the wall desired for initializing
c this mode. To maintain auto traverse throughout, enter a value
c for ytravman > ymaxx.
write(6,*) 'maximum y measurement for auto traverse? y= ?'
read(5,*) ytravmax
write(6,*)
write(6,*) 'maximum u velocity based on tunnel rpm? u= ?'
read(5,*) umaxx
umaxx=1.25*umaxx
write(6,*)
write(6,*)

c Recommend ml be minimum of 10.
write(6,*) 'Enter INTEGER # of data loops, 10000 FRAMES each.'
read(5,*) ml
write(6,*)
write(6,*) 'Install traverse control in output of clk 4'
write(6,*) 'Install traverse count in s of clk 6'
write(6,*) 'Move hot-wire to wall and set Controller '
write(6,*) '1. switch to UP movement !!!'
write(6,*) '2. on computer control'
write(6,*) '3. set y-counter to 0'
write(6,*)
write(6,*)
write(6,*) 'When ready to take data, press return.'
read(5,*)
write(6,*)
call mropen(adpn,addev,RDWR)
call mropen(clkpn1,frameclkdev,RDWR)
call mropen(clkpn2,burstclkdev,RDWR)
call mradmod(adpn,RANGE,0)
call mradran(adpn,2,cgarrray)
c*****
c LOOP starts here -- for each vertical position in b.l.
150 continue
c*****
yposi=.001*float(tcoun)
puav=0.
pvav=0.
pup2=0.
pvp2=0.
pupvp=0.
c*****
cc data acquisition
call mrcik2(clkpn1,clkpn2,NOTUSED,NEARFRQ,FREQ,rfreq,
& NEARFRQ,BRSFRQ,rbrst,NCHAN,LOW)
call mradxin(adpn,clkpn1,clkpn2,fchan,NCHAN,incr,gain,
& NFRAMES,rawdata)
call mrevwt(adpn,status,100000)

```



```

c*****
do 405 kl=1,ml
do 155 i=1,NCHAN*NFRAMES
155  rawdat1(i)=rawdata(i)
c*****
cc  data acquisition
    if(kl.eq.ml) goto 175
    call mrc1k2(clkpn1,clkpn2,NOTUSED,NEARFRQ,FREQ,rfreq,
&      NEARFRQ,BRSFRQ,rbrst,NCHAN,LOW)
    call mradxin(adpn,clkpn1,clkpn2,fchan,NCHAN,incr,gain,
&      NFRAMES,rawdata)
c*****
c  The statistical technique of calculating fluctuating
c  velocities are standard ones and outlined in Carnahan,
c  Applied Numerical Methods, Sections 8.5 & 8.6. Note that
c  rawdata is converted and stored as rawdat1 so that
c  simultaneous data acquisition and calculations occur. The
c  first data set is obtained before entering the "ml" loop,
c  and no data is collected in the loop when i=ml. The letter
c  p before a term refers to cumulative values for i=1 to ml.
c  Other terms are identified below unless obvious:
c  ui=instantaneous u velocity component
c  vi=instantaneous v velocity component
c  .av=avg value  .av2=sums of squares later averaged
c  uvav=sum of instantaneous velocity product
c  up2=u prime squared  vp2=v prime squared
c  upvp=Reynolds stress fluctuating velocity product
c*****
175  uav=0.
    vav=0.
    uav2=0.
    vav2=0.
    uvav=0.
do 200 i=1,NFRAMES
    j=1+NCHAN*(i-1)
    vol0=.00244141*real(rawdat1(j))/dcgain
    vol1=.00244141*real(rawdat1(j+1))/dcgain
    ui=u25(vol0,vol1)
    vi=v25(vol0,vol1)
    uav=uav+ui
    vav=vav+vi
    uav2=uav2+ui*ui
    vav2=vav2+vi*vi
    uvav=uvav+ui*vi
200  continue
201  uav=uav/real(NFRAMES)
    vav=vav/real(NFRAMES)
    up2=(uav2-real(NFRAMES)*uav**2)/real(NFRAMES-1)
    vp2=(vav2-real(NFRAMES)*vav**2)/real(NFRAMES-1)
    uvav=uvav/real(NFRAMES)
    upvp=uvav-uav*vav
    puav=puav+uav
    pvav=pvav+vav
    pupvp=pupvp+upvp
    pup2=pup2+up2
    pvp2=pvp2+vp2
c*****
    if(kl.eq.ml) goto 405
    call mrevwt(adpn,status,100000)
c*****
405  continue
    puav=puav/real(ml)

```



```

        pvav=pvav/real(m1)
        pupvp=pupvp/real(m1)
        puprms=sqrt(pup2/real(m1))
        pvprms=sqrt(pvp2/real(m1))
c*****
415  x2(iplot)=10.*puprms
        x1(iplot)=puav
        y1(iplot)=yposi
c    call plot(iplot,x1,y1,x2,lp1,lp2,lp3,idd)
        iplot=iplot+1
        idd=1
        write(8,445) yposi,puav,pvav,
        &puprms,pupvp,pvprms
        write(6,*)
        write(6,420)
420  format(5x,'y',7x,'uy',8x,'vy',5x,'uprms',5x,
        &'upvp',5x,'vprms')
        write(6,445) yposi,puav,pvav,
        &puprms,pupvp,pvprms
445  format(6f9.5,3x)
        write(6,*)
500  write(6,*) 'tcount =',tcount
        write(6,*)
c*****
c traverse
        if(yposi.ge.ytravmax) goto 650
600  call mrclkintgat (int_clk,1)
        call mrccounters (2,count_clk,3,1,0)
        call mrbufall (count_clk,counterval,2,4)
        call mrclkarm (2,count_clk)
        call mrxinq (count_clk(1),1,1,0)
c
        if (tcount.ge.300) istep=3600
        if (tcount.lt.300) istep=3000
        if (tcount.lt.150) istep=2400
        if (tcount.lt.80) istep=1200
        if (tcount.lt.30) istep=400
        if (tcount.lt.15) istep=150
        if (yposi.gt.ymaxx) goto 700
        call mrclksetter(clkpath0,15,5,istep,0,0,2,8)
        call mrclkarm(1,clkpath0)
        call astpause$(0,3000)
c
        call mrclkdis(1,clkpath0)
        call mrcloneshot (int_clk,0,50.,rdelay,0,100.,rwidth,0,0)
        call mrclkarm (1,int_clk)
        tcount=tcount+counterval(ibuff)
        if (ibuff.eq.1) then
            ibuff=3
        else
            ibuff=1
        endif
        if(yposi.lt.ytravmax) goto 690
c*****
650  if (yposi.gt.ymaxx) goto 700
        write(6,*) 'Ensure traverse in manual for remaining data.'
        write(6,*)
        write(6,*) 'Move traverse to desired y-position. Enter value'
        write(6,*) 'accurate to 3 decimal places.'
        read (5,*) yman
        tcount=int(1000.*yman)
        write(6,*)

```



```

c*****
c LOOP ends here
690  goto 150
c*****
c finish
c
700  write(8,*) tempf,' temperature (F)'
      write(8,*) xposi,' inches downstream of reference point'
      close(8)
      call mronesot(int_clk,0,50.,rdelay,0,100.,rwidth,0,0)
      call mrcclkarm(1,int_clk)
      write(6,*) 'switch traverse control to manual'
      write(6,*) 'press return'
      read(5,*)

      idd=2
      iplot=iplot-1
      call plot(iplot,x1,y1,x2,lp1,lp2,lp3,idd)
      call mrcclkintgat(int_clk,0)
      call mrclosall
      stop
      end
*****
ccc  FUNCTIONS TO CONVERT VOLTAGES TO VELOCITY AND ANGLE  ccc
*****

      function u25(e1,e2)
      common /ufunct25/ a(25)
      u25=a(1)+e1*(a(2)+e1*(a(3)+e1*(a(4)+e1*a(5))))+
&e2*(a(6)+e1*(a(7)+e1*(a(8)+e1*(a(9)+e1*a(10))))+
&e2*(a(11)+e1*(a(12)+e1*(a(13)+e1*(a(14)+e1*a(15))))+
&e2*(a(16)+e1*(a(17)+e1*(a(18)+e1*(a(19)+e1*a(20))))+
&e2*(a(21)+e1*(a(22)+e1*(a(23)+e1*(a(24)+e1*a(25))))))
      return
      end
c*****
      function v25(e1,e2)
      common /vfunct25/ b(25)
      v25=b(1)+e1*(b(2)+e1*(b(3)+e1*(b(4)+e1*b(5))))+
&e2*(b(6)+e1*(b(7)+e1*(b(8)+e1*(b(9)+e1*b(10))))+
&e2*(b(11)+e1*(b(12)+e1*(b(13)+e1*(b(14)+e1*b(15))))+
&e2*(b(16)+e1*(b(17)+e1*(b(18)+e1*(b(19)+e1*b(20))))+
&e2*(b(21)+e1*(b(22)+e1*(b(23)+e1*(b(24)+e1*b(25))))))
      return
      end
c*****
c  SUBROUTINES -- PLOTTING (see MASSCOMP Data Presentation
c                      Manual)
c  Link plot routines with sp-45 library (-lmp)
c*****
      subroutine plot(int,xa,ya,xb,l1,l2,l3,id)
      integer*4 NULL
      integer*4 SIZEOFGCA
      integer*4 NULLINTRAY
      real*4 UNDEF
      parameter (NULL=0)
      parameter (SIZEOFGCA=1000)
      parameter (NULLINTRAY=-2)
      parameter (UNDEF=-.11e39)

```



```

integer*4 gls(SIZEOFGCA)
character*30 l1,l2,l3
character*9 ln
integer*4 mkpts(2),siz(2),li(2)
real xa(1),ya(1),xb(1)
common /plot2/ gls,ymaxx,umaxx
ln='plottbl.g'
call mpinit(gls)
call mpgrids(gls,0,0)
call mpaxtype(gls,3,-1)
call mptics(gls,3,-1,-1)
call mpdevice(gls,"mcdigh",2,0)
call mpaxvals(gls,1,0.,umaxx,UNDEF,10)
call mpaxvals(gls,2,0.,ymaxx,UNDEF,10)
call mptitle(gls,4,-1,-1,' ')
call mptitle(gls,4,-1,2,11)
call mptitle(gls,2,-1,-1,12)
call mptitle(gls,1,-1,-1,13)
mkpts(1)=1
mkpts(2)=1
li(1)=NULL
li(2)=NULL
call mplines(gls,2,li,mkpts)
siz(1)=240
siz(2)=240
call mplotchrs(gls,'x*',2,NULLINTRAY,siz)
call mplotsrcy (gls,1,int,0,ya(1),"F",1,1,NULL,NULL)
call mplotsrcx (gls,1,int,0,xa(1),"F",1,1,NULL,NULL)
call mplotsrcy (gls,2,int,0,ya(1),"F",1,1,NULL,NULL)
call mplotsrcx (gls,2,int,0,xb(1),"F",1,1,NULL,NULL)
call mplot(gls,0,1,0)
if (id.eq.2) then
call mpfile(gls.ln,1,0)
call mpend(gls)
endif
return
end

```

c*****

PROGRAM

AUTOXCOLESFIT:

Non-Interactive Coles Fitting Algorithm for
Unmanipulated Turbulent Boundary Layer Mean
Velocity Profile Data

Input

profile data file name
temperature
stream location

Output

boundary layer parameters data file
Coles fit comparison plot file

c*****

```

program autoxcolesfit
parameter (npo=200,mpo=30)
parameter (np=5,mp=6)
dimension pam(mp,np),yam(mp),pr(np)
dimension ycor(npo),umean(npo),ufluc(npo)
real xplot(npo),yplot(npo),uu(npo),yy(npo)
character*20 name,online
character*20 l1,l2,l3
character*7 ln
common /fu/ ycor,umean,visc,istart,iend

```



```

c*****
c program shear
c reads data-file with mean-velocity and corresponding
c distance from wall, finds coefficients for arbitrary order
c polynomial for best curve fit (usually best values are:
c order=20 or 30 for about 60 data points.)
c Make sure that the data points are closely spaced .
c
c for more info see Applied Numerical Meth.,
c B. Carnahan... page 574
c
c gam.del,b coefficients for polynomial
c icount order of fit
c
c kay herbert, 1988
c*****
    icount=mpo
c====> read data
    write(6,*) 'data-file-name? '
    read(5,*) name
    open (51,file=name,status='old')
    i=0
    umx=0.
    ymx=0.
10  read(51,*,end=100) yco.um,zzz1,ur,zzz2,zzz3
    if (um.lt.-1.or.um.gt.55.) goto 10
    i=i+1
    ycor(i)=yco*.0254
    umean(i)=um
    ufluc(i)=ur
    if (yco.gt.ymx) ymx=yco
    if (um.gt.umx) umx=um
    goto 10
100 continue
125 write(6,*) 'temperature(F) ? '
    read(5,*) tempr
    write(6,*)
    write(6,*) 'xposition (in) ? '
    read(5,*) xposi

126 close(51)
    xposi=xposi*.0254
    imax=i
    mcount=i
    imax2=imax/2
    if (ycor(imax).lt.ycor(1)) then
    do 20 i=1,imax2
    ii=imax-i+1
    dum=ycor(i)
    ycor(i)=ycor(ii)
    ycor(ii)=dum
    dum=umean(i)
    umean(i)=umean(ii)
    umean(ii)=dum
    dum=ufluc(i)
    ufluc(i)=ufluc(ii)
    ufluc(ii)=dum
20  continue
    endif
    call param(tempr,vnu,visc.rho,cnot)
    istart=4
    iend=25

```



```

eps=0.
deps=1.e-4
utau=umx/20.
dutau=utau/10.
pr(1)=eps
pr(2)=utau
yam(1)=funk(pr)
pam(1,1)=pr(1)
pam(1,2)=pr(2)
pr(1)=eps+deps
pr(2)=utau
yam(2)=funk(pr)
pam(2,1)=pr(1)
pam(2,2)=pr(2)
pr(1)=eps
pr(2)=utau+dutau
yam(3)=funk(pr)
pam(3,1)=pr(1)
pam(3,2)=pr(2)
ndim=2
ftol=1.e-6
call amoeba(pam,yam,mp,np,ndim,ftol,funk,iter)
  eps=pam(1,1)
  utau=pam(1,2)
  uinf=umx
do 101 i=1,imax
dd=(ycor(i)+eps)*utau/visc
if (dd.le.15) istart=i
101 if (dd.le.330) iend=i
  deps=1.e-5
  dutau=utau/50.
  pr(1)=eps
  pr(2)=utau
  yam(1)=funk(pr)
  pam(1,1)=pr(1)
  pam(1,2)=pr(2)
  pr(1)=eps+deps
  pr(2)=utau
  yam(2)=funk(pr)
  pam(2,1)=pr(1)
  pam(2,2)=pr(2)
  pr(1)=eps
  pr(2)=utau+dutau
  yam(3)=funk(pr)
  pam(3,1)=pr(1)
  pam(3,2)=pr(2)
  ndim=2
  ftol=1.e-8
  call amoeba(pam,yam,mp,np,ndim,ftol,funk,iter)
  write(6,*) iter,pam(1,1),pam(1,2),umx

c===> plotting
  eps=pam(1,1)
  utau=pam(1,2)
  vmax=25.*utau
  vmin=2.*utau
  kz=0
  do 300 i=1,npo
  ul=vmin+(vmax-vmin)*(float(i-1)/float(np0-1))*2
  call spal(yl,ul,.41,5.0,utau,visc)
  if(yl.le.0.) kz=kz+1
  yplot(i)=yl

```



```

        xplot(i)=ul
300    continue
        kz=kz+1
        mcount=mcount-istart
        do 301 i=1,mcount
            uu(i)=umean(i+istart)/utau
301    yy(i)=(ycor(i+istart)+eps)/visc*utau
        do 302 i=kz,npo
            xplot(i+1-kz)=xplot(i)/utau
302    yplot(i+1-kz)=yplot(i)/visc*utau
        npp=npo+1-kz

        l1=name
        l2='u/u-tau'
        l3='u-tau*y/visc'
        ln='plot2.g'
        write(6,*) 'done'
c    call plot2(npp,yplot,xplot,mcount,yy,
c    *    uu,l1,l2,l3,ln,1)
        do 401 i=1,mcount
            uu(i)=ufluc(i+istart)/utau*20.
401    yy(i)=(ycor(i+istart)+eps)/visc*utau

        l1=name
        l2='u-p*20/u-tau'
        l3='u-tau*y/visc'
        ln='plot1.g'
        write(6,*) 'done'
c    call plot2(npp,yplot,xplot,mcount,yy,
c    *    uu,l1,l2,l3,ln,1)
c    write(6,*) 'output filename ?'
c    read(5,*) oname
        oname = 'xspalinf.dat'
        open (51,file=oname,status='fresh')
        do 501 i=2,mcount+1
            uu(i)=umean(i+istart-1)
501    yy(i)=(ycor(i+istart-1)+eps)
            uu(1)=0.
            yy(1)=0.
            delstar=0.
            phmom=0.
            do 502 i=1,mcount
                ddy=(yy(i+1)-yy(i))/2.
                phmom=phmom+ddy*uu(i)*(uinf-uu(i))
                phmom=phmom+ddy*uu(i)*(uinf-uu(i+1))
                delstar=delstar+ddy*(uinf-uu(i))
502    delstar=delstar+ddy*(uinf-uu(i+1))
            delstar=delstar/uinf
            phmom=phmom/(uinf**2)
            h=delstar/phmom
            red=uinf*delstar/visc
            cf=2.*utau**2/uinf**2
            yplus=eps*utau/visc
            twall=rho*utau**2
            do 503 i=1,mcount
                if(uu(i).ge.(.995*uinf)) then
                    delta=yy(i)
                    i=mcount
                else
                    goto 503
            endif
503    continue

```



```

write(51,*) name,' file-name'
write(51,*) tempr,' temperature (K)'
write(51,*) xposi,' x-position (m)'
write(51,*) visc,' kin. viscosity (m^2/sec)'
write(51,*) rho,' air density (kg/m^3)'
write(51,*) eps,' y-offset (m)', ' =',yplus,' viscous units.'
write(51,*) utau,' shear velocity (m/sec)'
write(51,*) twall,' tauwall (Pa)'
write(51,*) delstar,' displ. thickness (m)'
write(51,*) uinf,' u-infinity (m/sec)'
write(51,*) phmom,' momentum thickness (m)'
write(51,*) h,' Shape Factor'
write(51,*) cf,' cf'
write(51,*) red,' Reynolds number, delstar'
write(51,*) delta,' delta (m)'
close(51)
open (50,file='spal1.dat',status='old',access='sequential')
write(50,*) uinf,utau,red,cf,delstar,twall
close(50)
call system("cat spal1.dat >> cfdata.dat")
stop
end
subroutine plot2(int,xa,ya,intb,xb,yb,l1,l2,l3,ln,id)
include'usr/include/libmp.f'
integer*4 gls(SIZEOFGCA)
character*20 l1,l2,l3
character*7 ln
integer*4 mkpts(3),siz(3)
real xa(1),ya(1),xb(1),yb(1),yc(200)
c*****
c
c plot2, plot 2 x-y graphs
c link with sp-45 library (lmp)
c
c kay herbert 1987
c
c*****
call mpinit(gls)
call mpgrids(gls,0,0)
call mpaxtype(gls,3,-1)
call mptics(gls,3,-1,-1)

call mplotsrcy (gls,1,int,0,ya(1),"F",1,1,NULL,NULL)
call mplotsrcx (gls,1,int,0,xa(1),"F",1,1,NULL,NULL)
call mplotsrcy (gls,2,intb,0,yb(1),"F",1,1,NULL,NULL)
call mplotsrcx (gls,2,intb,0,xb(1),"F",1,1,NULL,NULL)
mkpts(1)=0
mkpts(2)=1
call mplines(gls,2,NULLINTRA Y,mkpts)
siz(1)=240
siz(2)=240
call mplotchrs(gls,'*',1,NULLINTRA Y,siz)

c====> take comment out if screen-plot desired
c call mpdevice(gls,"mcdigh",2,0)
c====
if (id.eq.1) then
call mplogax(gls,1,2)
call mpaxvals(gls,1,1.,5000.,UNDEF,6)
call mpaxvals(gls,2,0.,50.,UNDEF,10)
else

```



```

        call mpaxvals(gls,1,0.,1.,UNDEF,10)
        call mpaxvals(gls,2,0.,10.,UNDEF,10)
    endif
    call mptitle(gls,4,-1,-1,' ')
    call mptitle(gls,4,-1,2,11)
    call mptitle(gls,2,-1,-1,12)
    call mptitle(gls,1,-1,-1,13)

    call mpfile(gls,ln,1,0)
    call mplot(gls,0,1,0)
    call mpend(gls)
    return
end
c*****
subroutine spal(y,u,k,B,ut,visc,delta1)
real k,uu(100),yy(100)
up=u/ut
uu(1)=0.0
yy(1)=0
uu(2)=.99
yy(2)=1
uu(3)=1.96
yy(3)=2
uu(4)=2.90
yy(4)=3
uu(5)=3.80
yy(5)=4
uu(6)=4.65
yy(6)=5
uu(7)=5.45
yy(7)=6
uu(8)=6.19
yy(8)=7
uu(9)=6.87
yy(9)=8
uu(10)=7.49
yy(10)=9
uu(11)=8.05
yy(11)=10
uu(12)=9.00
yy(12)=12
uu(13)=9.76
yy(13)=14
uu(14)=10.4
yy(14)=16
uu(15)=10.97
yy(15)=18
uu(16)=11.49
yy(16)=20
uu(17)=12.34
yy(17)=24
uu(18)=12.99
yy(18)=28
uu(19)=13.48
yy(19)=32
uu(20)=13.88
yy(20)=36
uu(21)=14.22
yy(21)=40
uu(22)=14.51
yy(22)=44
uu(23)=14.87

```



```

yy(23)=50
uu(24)=15.33
yy(24)=60
uu(25)=16.04
yy(25)=80
uu(26)=16.60
yy(26)=100
uu(27)=17.61
yy(27)=150
uu(28)=18.33
yy(28)=200
uu(29)=19.34
yy(29)=300
uu(30)=20.06
yy(30)=400
uu(31)=20.62
yy(31)=500
uu(32)=21.08
yy(32)=600
uu(33)=21.79
yy(33)=800
uu(34)=22.35
yy(34)=1000
uu(35)=23.36
yy(35)=1500
uu(36)=24.08
yy(36)=2000
uu(37)=25.09
yy(37)=3000
uu(38)=25.81
yy(38)=4000
uu(39)=26.37
yy(39)=5000
uu(40)=26.83
yy(40)=6000
uu(41)=27.54
yy(41)=8000
uu(42)=28.10
yy(42)=10000
i=2
10  if (uu(i).lt.up) then
    i=i+1
    goto 10
  endif
  xint=(uu(i)-up)/(uu(i)-uu(i-1))
  yp=xint*(yy(i-1)-yy(i))+yy(i)
  y=yp*visc/ut
  return
end
function funk(pr)
  real k
  dimension pr(20)
  dimension y(200),u(200)
  common /fu/ y,u,visc,ii,iii,delta1
  k=.41
  B=5.0
  funk=0.

```



```

do 1 i=ii,iii
uu=u(i)
y1=y(i)
call spal(y2,uu,k,B,pr(2),visc,delta1)
funk=funk+((y1+pr(1)-y2)/1.)*2
1 continue
return
end
subroutine amoeba(p,y,mp,np,ndim,ftol,funk,iter)
parameter (nmax=20,alpha=1.0,beta=0.5,gamma=2.0,itmax=1500)
dimension p(mp,np),y(mp),pr(nmax),prr(nmax),pbar(nmax)
mpts=ndim+1
iter=0
1 ilo=1
if(y(1).gt.y(2))then
ihi=1
inhi=2
else
ihi=2
inhi=1
endif
do 11 i=1,mpts
if(y(i).lt.y(ilo)) ilo=i
if(y(i).gt.y(ihi)) then
inhi=ihi
ihi=i
else if(y(i).gt.y(inhi))then
if (i.ne.ihi) inhi=i
endif
11 continue
rtol=2.*abs(y(ihi)-y(ilo))/(abs(y(ihi))+abs(y(ilo)))
if(rtol.lt.ftol)return
if(iter.eq.itmax) then
write(6,*) 'exceeding maximum iterations'
return
endif
iter=iter+1
do 12 j=1,ndim
pbar(j)=0.
12 continue
do 14 i=1,mpts
if(i.ne.ihi) then
do 13 j=1,ndim
pbar(j)=pbar(j)+p(i,j)
13 continue
endif
14 continue
do 15 j=1,ndim
pbar(j)=pbar(j)/ndim
pr(j)=(1.+alpha)*pbar(j)-alpha*p(ihi,j)
15 continue
ypr=funk(pr)
if(ypr.le.y(ilo))then
do 16 j=1,ndim
prr(j)=gamma*pr(j)+(1.-gamma)*pbar(j)
16 continue
yprr=funk(prr)
if(yprr.lt.y(ilo))then
do 17 j=1,ndim
p(ihi,j)=prr(j)
17 continue
y(ihi)=yprr

```



```

    else
      do 18 j=1,ndim
        p(ihi,j)=pr(j)
18      continue
      y(ihi)=ypr
    endif
    else if(ypr.ge.y(inhi)) then
      if(ypr.lt.y(ihi))then
        do 19 j=1,ndim
          p(ihi,j)=pr(j)
19        continue
          y(ihi)=ypr
        endif
        do 21 j=1,ndim
          prr(j)=beta*p(ihi,j)+(1.-beta)*pbar(j)
21        continue
          ypr=funk(prr)
          if(ypr.lt.y(ihi)) then
            do 22 j=1,ndim
              p(ihi,j)=prr(j)
22            continue
              y(ihi)=ypr
            else
              do 24 i=1,mpts
                if(i.ne.ilo)then
                  do 23 j=1,ndim
                    pr(j)=0.5*(p(i,j)+p(ilo,j))
                    p(i,j)=pr(j)
23                  continue
                    y(i)=funk(pr)
                  endif
                endif
              continue
            endif
          else
            do 25 j=1,ndim
              p(ihi,j)=pr(j)
25            continue
              y(ihi)=ypr
            endif
          goto 1
        end
      subroutine param(temp,visc,vkin,rho,cnot)
c*****
c subroutine param.f by Kurt W. Roth, 8/88.
c modified by kay herbert
c
c routine to compute viscosity of air at any temperature
c Farenheit, Celsius, or Kelvin; it also computes
c pressure drop for pitot at any speed (m/s).
c
c for viscosity formula, see VISCOSITY OF GASES by WATSON;
c see CRC PHYSICS and CHEMISTRY for density formula.
c
c Error of formula 270-600 K is .25%.
c
c input temperature in fahrenheit(F)
c output viscosity(kg/m-s)
c kinematic viscosity(m^2/s)
c density(kg/m^3)
c speed of sound(m/s)

```



```

c temperature (K)
c
c*****
      integer icaler,krunch
      real TEMP, CONVER, VISC,RE,RHO,VKIN,VEL,DP,CON

      icaler=1

      if (icaler .eq. 2 ) goto 2
      if (icaler .eq. 3) goto 1
      TEMP =( TEMP - 32)/1.8
      if (icaler .eq. 1) goto 2
1      TEMP = TEMP -273.15
2      RHO = 1.293/(1 + .00367*TEMP)
      TEMP = TEMP + 273.15
      s =100/(TEMP)
      a0 = .55279544
      a1 = 2.818916
      a2 = -13.508340
      a3 = 39.353086
      a4 = -41.419387
      RE = sqrt(TEMP)
      VISC=(RE)/(a0 +a1*s +a2*s**2 +a3*s**3 +a4*s**4)/10**6
      VKIN = VISC/RHO
      cnot=1.4*287*temp
      cnot=sqrt(cnot)
      return
      end
c*****

```

PROGRAM

MANUALXCOLE:

Interactive Coles Fitting Algorithm

Input

profile data file name
 Coles data file
 temperature
 u_τ -- estimate
 y^+ offset -- estimate

Output

Coles fit comparison plot file
 Values for u_τ and y^+ offset

```

c*****
c This program uses historical data from Coles for a turbulent
c boundary layer mean velocity profile and compares the
c experimental mean velocity profile to that of Coles. After
c enterin appropriate values for utau and y-offset, a visual
c fit to Coles can be performed (Note: utau may be obtained
c from surface fence, preston tube, or estimated.). The fit
c should be performed such that data for y-plus of 20-200
c either lies directly on Coles data (in the case where no
c determination of utau was made) or parallel to the same (if
c utau is otherwise determined).
c      - frank camelio, june 1989
c*****
      program manualxcole
      real xu(300),xv(300),y(300),ya(50),ua(50)
      real xuu(300),xuv(300),xvv(300),xup(300),yp(300)
      real temp,roh,mu,nu
      character*30 l1,l2,l3,file1
      character*15 ln1

```



```

l2=' UMEAN/UTAU'
l3='YPLUS (y*utau/nu)'
ln1='xtunu.g'
write(6,*) 'Enter file name containing profile data.'
read(5,*) file1
write(6,*)
l1=file1
i=1
open(51,file=file1,status='old')
50  read(51,*,end=100) y(i),xu(i),xv(i),xuu(i),xuv(i),xvv(i)
    i=i+1
    goto 50
100 continue
    close(51)
    int=i-1
    k=1
    open(52,file='coles.dat',status='old')
125  read(52,*,end=130) ua(k),ya(k)
    k=k+1
    goto 125
130 continue
    close(52)
    inta=k-1
c***** Reassign values to select data for plotting *****
    write(6,*) 'Enter temperature (deg F) at time data collected.'
    read(5,*) temp
    temp=(temp-32.)/1.8
    roh=1.293/(1+.00367*temp)
    mu=1.853e-05-(.005e-05*(27-temp))
    nu=mu/roh
160  write(6,*) 'Enter value for utau (m/sec).'
    read(5,*) utau
    write(6,*)
    write(6,*) 'Enter offset in y-plus (viscous units).'
    read(5,*) yoffset
    write(6,*)
    yoff=yoffset*nu/utau
    jp=1
    do 200 j=1,int
        xup(j)=xu(j)/utau
        ypp=.0254*y(j)*utau/nu+yoffset
        if(ypp.lt.1.) goto 200
        yp(jp)=ypp
        xup(jp)=xup(j)
        jp=jp+1
200  continue
    jp = jp-1
    call plot2(inta,ua,ya,jp,xup,yp,l1,l2,l3,ln1)
    write(6,*) 'utau = ',utau,' m/sec'
    write(6,*) 'yoffset (m)= ',yoff,' = ',yoffset,' viscous units.'
250  write(6,*)
    write(6,*) 'Enter INTEGER 1 to try a different'
    write(6,*) 'y-offset and/or utau. Else any integer.'
    read(5,*) k1
    if (k1.eq.1) goto 160
1000 stop
end
c*****c
    subroutine plot2(int,ua,ya,intp,xup,yp,l1,l2,l3,ln1)
    include '/usr/include/libmp.f'

```



```

integer*4 gls(SIZEOFGCA)
character*30 l1,l2,l3
character*10 ln1
integer*4 mkpts(2),siz(2),LINRAY(2)
real ua(1),ya(1),xup(1),yp(1)
call mpinit(gls)
call mpgrids(gls,0,0)
call mpaxtype(gls,3,-1)
call mptics(gls,3,-1,-1)
call mplotsrcy (gls,1,int,0,ua(1),"F",1,1,NULL,NULL)
call mplotsrcx (gls,1,int,0,ya(1),"F",1,1,NULL,NULL)
call mplotsrcy (gls,2,intp,0,xup(1),"F",1,1,NULL,NULL)
call mplotsrcx (gls,2,intp,0,yp(1),"F",1,1,NULL,NULL)
mkpts(1)=0
mkpts(2)=1
LINRAY(1)=1
LINRAY(2)=1
call mplines(gls,2,LINRAY,mkpts)
siz(1)=200
siz(2)=200
call mplotchrs(gls,'*',1,NULLINRAY,siz)

call mpdevice(gls,"mcdigh",2,0)
call mplogax(gls,1,2)
call mpaxvals(gls,1,UNDEF,5000.,UNDEF,6)
call mpaxvals(gls,2,0.,40.,UNDEF,6)
call mptitle(gls,4,-1,-1,' ')
call mptitle(gls,4,-1,2,l1)
call mptitle(gls,2,-1,-1,l2)
call mptitle(gls,1,-1,-1,l3)
call mpfile(gls,ln1,1,0)
call mplot(gls,0,1,0)
call mpend(gls)
return
end

```

c*****

DATA FILE:

Data of Coles [3] to Which Experimental Mean
Velocity Data is Fit (Preceding Program)

c*****

```

.99 1.
1.96 2.
2.9 3.
3.8 4.
4.65 5.
5.45 6.
6.19 7.
6.87 8.
7.49 9.
8.05 10.
9. 12.
9.76 14.
10.4 16.
10.97 18.
11.49 20.
12.34 24.
12.99 28.
13.48 32.
13.88 36.
14.22 40.
14.51 44.

```


14.87 50.
 15.33 60.
 16.04 80.
 16.6 100.
 17.61 150.
 18.33 200.
 19.34 300.
 20.06 400.
 20.62 500.
 21.08 600.
 21.79 800.
 22.35 1000.
 23.36 1500.
 24.08 2000.
 25.09 3000.
 25.81 4000.
 26.37 5000.
 26.83 6000.
 27.54 8000.
 28.1 10000.
 100. 10001.

c*****

PROGRAM

XTBLPARAMETERS:

Coles Interactive Fitting Algorithm and Calculation of
 Various Boundary Layer Parameters

Input

profile data file name
 temperature
 u_τ (Coles fit)
 y^+ offset (Coles fit)

Output

boundary layer parameters data file

c*****

c This program reads boundary layer data as measured
 c with an X-probe (reads output of data acquisition program
 c such as xtbldatacq.f). The values of utau and y-offset
 c from either a manual or auto Coles fit program are
 c required to calculate certain parameters. Note that the
 c boundary layer thickness, delta, is obtained approximately
 c using the .995 definition. This was chosen so that data
 c can be compared with historical results (Klebanoff) when
 c miscellaneous plots are obtained. Another option would be
 c to use the law of the wake and incorporate determination of
 c delta in Coles fit routine.

c*****

```

program xtblparameters
real y(300),u(300),v(300),uu(300),uv(300),vv(300)
real del(300),theta(300),nu
character*20 file1
open(7,file='xtblanal.dat',status='fresh')
write(6,*) 'Enter tbl data file name.'
read(5,*) file1
write(6,*)
write(6,*) 'Enter value for y-offset based on Coles fit.'
read(5,*) yoff
write(6,*)
write(6,*) 'Enter value for utau based on Coles fit.'
read(5,*) utau
write(6,*)

```



```

write(6,*) 'Enter temp (deg F) at time of b.l. measurements.'
read(5,*) temp
write(6,*)
temp=(temp-32.)/1.8
rho=1.293/(1+.00367*temp)
nu=(1.853e-05-.005e-05*(27-temp))/rho
y0=nu*yoff/utau
y(1)=0.
u(1)=0.
v(1)=0.
uu(1)=0.
uv(1)=0.
vv(1)=0.
i=2
open(51,file=file1,status='old')
100 read(51,*,end=200) y(i),u(i),v(i),uu(i),uv(i),vv(i)
y(i)=.0254*y(i)+y0
uinf=max(uinf,u(i))
i=i+1
goto 100
200 close(51)
n=i-1
do 250 i=1,n
if(u(i)/uinf.ge.0.995) then
delta=y(i)
i=n+1
goto 250
endif
250 continue
do 300 i=1,n
del(i)=1-u(i)/uinf
if(del(i).lt.0) del(i)=0.
theta(i)=del(i)*u(i)/uinf
300 if(theta(i).lt.0) theta(i)=0.
delstar=(1-del(2))*y0*.5+del(2)*y(2)
thestar=theta(2)*y(2)*.5
do 400 i=2,n-1
delstar=delstar+0.5*(del(i+1)+del(i))*(y(i+1)-y(i))
400 thestar=thestar+0.5*(theta(i+1)+theta(i))*(y(i+1)-y(i))
h=delstar/thestar
Redel=uinf*delstar/nu
cf=2*utau**2/uinf**2
tauwall=rho*utau**2
write(6,*) 'displacement thickness (m) = ', delstar
write(6,*) 'momentum thickness (m) = ', thestar
write(6,*) 'shape factor = ', h
write(6,*) 'yoffset (m) =',y0,' = ',yoff,' viscous units'
write(6,*) 'kinematic viscosity (m^2/sec) =',nu
write(6,*) 'air density (kg/m^3) = ',rho
write(6,*) 'uinf (m/sec) =',uinf
write(6,*) 'temp C = ',temp
write(6,*) 'Reynolds # (delstar) = ',Redel
write(6,*) 'delta (m) ~',delta
write(6,*) 'cf = ', cf
write(6,*) 'tauwall (Pa) = ',tauwall
write(6,*) 'friction velocity (m/sec) = ', utau
write(7,*) 'displacement thickness (m) = ', delstar
write(7,*) 'momentum thickness (m) = ', thestar
write(7,*) 'shape factor = ', h
write(7,*) 'yoffset (m) =',y0,' = ',yoff,' viscous units'
write(7,*) 'kinematic viscosity (m^2/sec) =',nu
write(7,*) 'air density (kg/m^3) = ',rho

```



```

write(7,*) 'uinf (m/sec) = ',uinf
write(7,*) 'temp C = ',temp
write(7,*) 'Reynolds # (delstar) = ',Redel
write(7,*) 'delta (m) ~',delta
write(7,*) 'cf = ',cf
write(7,*) 'tauwall (Pa) = ',tauwall
write(7,*) 'friction velocity (m/sec) = ', utau
close(7)
stop
end

```

c*****

PROGRAM XTBLPLOT: Plotting of Boundary Layer Parameters

Input

profile data file name
 Klebanoff data file
 u_τ (Coles)
 y offset in meters (Coles)

Output

five plot files
 mean velocity profiles
 Klebanoff comparison profiles
 stream rms fluctuating
 vertical rms fluctuating
 Reynolds stress (normalized)
 shear correlation

c*****

```

c  This program generates five plots of mean velocities,
c  fluctuating velocities, Reynolds stress, and shear
c  correlation as a function of distance or non-dimensional
c  distance from the wall. Fluctuating velocities are
c  plotted with historical data of Klebanoff. Input data
c  is obtained from output of data acquisition program
c  purged of non-numeric terms, from Klebanoff data file,
c  and interactively from results of Coles fitting routine
c  (utau, y-offset).
c  - frank camelio, june 1989

```

c*****

```

program xtblplot
real xu(300),xv(300),y(300),yd(300)
real xuu(300),xuv(300),xvv(300),xut(300)
real vk(50),ykv(50),uk(50),yku(50)
character*30 i1,i12,i13,i22,i23,i32,i41,i42,i51,i52
character*7 ln1,ln2,ln3,ln4,ln5
character*15 fname
i12=' HEIGHT ABOVE WALL (IN.)'
i13='(*)UAVG (x)VAVG (M/SEC)'
i22='(*)u/U (x)u/U (Klebanoff)'
i23=' y/delta'
i32='(*)v/U (x)v/U (Klebanoff)'
i41='NORMALIZED REYNOLDS STRESS'
i42=' -uv/utau^2'
i51='SHEAR CORRELATION'
i52=' -uv/(urms*vrms)'
ln1='xtun1.g'
ln2='xtun2.g'
ln3='xtun3.g'
ln4='xtun4.g'
ln5='xtun5.g'

```



```

open(52,file='klebnoff.dat',status='old')
  read(52,*) nku,nkv
do 25 i=1,nku
25  read(52,*) uk(i),yku(i)
do 50 i=1,nkv
50  read(52,*) vk(i),ykv(i)
close(52)
write(6,*) 'Enter name of tbl complete velocity data file.'
read(5,*) fname
l1=fname
write(6,*)
write(6,*) 'Enter utau in m/sec based on Coles fit.'
read(5,*) utau
write(6,*)
write(6,*) 'Enter yoffset in METERS determined from analysis or'
write(6,*) 'an appropriate fitting routine.'
read(5,*) yoff
write(6,*)
i=1
open(51,file=fname,status='old')
70  read(51,*,end=100) y(i),xu(i),xv(i),xuu(i),xuv(i),xvv(i)
c data in y originally in inches converted to meters.
  y(i)=.0254*y(i)+yoff
  i=i+1
goto 70
100 continue
close(51)
int=i-1
uinf=0.
do 150 j=1,int
  uinf=max(uinf,xu(j))
150 continue
c Note the .995 method of calculating delta
do 155 i=1,int
  if(xu(i)/uinf.ge.0.995) then
    delta=y(i)
    i=int+1
  endif
155 continue
do 160 j=1,int
  xut(j)=-xuv(j)/(utau**2)
160 continue
do 170 j=1,int
  xuv(j)=-xuv(j)/(xuu(j)*xvv(j))
170 continue
do 200 j=1,int
  yd(j)=y(j)/delta
  xuu(j)=xuu(j)/uinf
200 continue
do 400 j=1,int
  xvv(j)=xvv(j)/uinf
400 continue
c*****
call plot1(int,y,xu,int,y,xv,l1,l12,l13,ln1,1)
call plot1(int,xuu,yd,nku,uk,yku,l1,l22,l23,ln2,2)
call plot1(int,xvv,yd,nkv,vk,ykv,l1,l32,l23,ln3,3)
call plot2(int,xut,yd,l41,l42,l23,ln4,4)
call plot2(int,xuv,yd,l51,l52,l23,ln5,5)

```



```

stop
end
c*****c
subroutine plot1(int1,y1,x1,int2,y2,x2,ll1,ll2,ll3,ln,kn)
include '/usr/include/libmp.f'
integer*4 gls(SIZEOFGCA)
integer*4 linray(2),mrkray(2),siz(2)
real x1(int1),y1(int1),x2(int2),y2(int2)
character*30 ll1,ll2,ll3
character*7 ln
call mpinit(gls)
call mpgrids(gls,0,0)
call mpaxtype(gls,3,-1)
call mplotsrcy (gls,1,int1,0,y1(1),"F",1,1,NULL,NULL)
call mplotsrcx (gls,1,int1,0,x1(1),"F",1,1,NULL,NULL)
call mplotsrcy (gls,2,int2,0,y2(1),"F",1,1,NULL,NULL)
call mplotsrcx (gls,2,int2,0,x2(1),"F",1,1,NULL,NULL)
call mpdevice(gls,"mcdigh",2,0)
linray(1)=1
linray(2)=1
mrkray(1)=1
mrkray(2)=1
call mplines (gls,2,LINRAY,MRKRAY)
siz(1)=150
siz(2)=180
call mplotchrs(gls,'*x',2,NULLINTRAY,siz)
call mpaxvals(gls,1,UNDEF,UNDEF,UNDEF,6)
call mptitle(gls,4,-1,-1,' ')
call mptitle(gls,4,-1,2,ll1)
call mptitle(gls,2,-1,-1,ll2)
call mptitle(gls,1,-1,-1,ll3)
call mpfile(gls,ln,1,0)
write(6,*) 'To view plot ',kn,' type ',kn,' and (return)'
read(5,*) k1
if (k1.eq.kn) then
  call mplot(gls,0,1,0)
else
  goto 778
endif
778 continue
call mpend(gls)
return
end
c*****c
subroutine plot2(int,xa,y,ll1,ll2,ll3,ln,k1)
include '/usr/include/libmp.f'
integer*4 gls(SIZEOFGCA)
integer*4 linray(1),mrkray(1),siz(1)
real xa(int),y(int)
character*30 ll1,ll2,ll3
character*7 ln
call mpinit(gls)
call mpgrids(gls,0,0)
call mpaxtype(gls,3,-1)
call mplotsrcy (gls,1,int,0,xa(1),"F",1,1,NULL,NULL)
call mplotsrcx (gls,1,int,0,y(1),"F",1,1,NULL,NULL)
call mpdevice(gls,"mcdigh",2,0)
linray(1)=1
mrkray(1)=1
call mplines (gls,1,LINRAY,MRKRAY)
siz(1)=200
call mplotchrs(gls,'*',1,NULLINTRAY,siz)

```



```

if(kl.eq.4) call mpaxvals(gls,1,UNDEF,UNDEF,UNDEF,6)
if(kl.eq.5) call mpaxvals(gls,2,UNDEF,1.0,UNDEF,6)
call mptitle(gls,4,-1,-1,' ')
call mptitle(gls,4,-1,2,ll1)
call mptitle(gls,2,-1,-1,ll2)
call mptitle(gls,1,-1,-1,ll3)
call mpfile(gls,ln,1,0)
write(6,*) 'To view plot ',kl,' type ',kl,' and (return)'
read(5,*) k2
if (k2.eq.kl) then
  call mplot(gls,0,1,0)
else
  goto 779
endif
779 continue
call mpend(gls)
return
end
c*****c

```

DATA FILE:

Klebanoff (TN 3178) Historical Data of Fluctuating Stream and Vertical Velocity Components

```

c*****c
33  20
0.  0.
.061 .0015
.075 .00188
.084 .00225
.087 .00275
.092 .00313
.103 .00413
.107 .005
.110 .00675
.112 .00838
.103 .0146
.0865 .0213
.0795 .040
.0748 .083
.071 .133
.0715 .143
.0643 .230
.0625 .258
.061 .295
.0605 .330
.055 .405
.0535 .430
.050 .493
.0508 .495
.0425 .585
.040 .6175
.0383 .655
.0369 .655
.0289 .785
.013 .89
.0065 1.0
.0035 1.15
.0015 1.33

```


0.	0.
.0325	.017
.033	.020
.034	.023
.036	.040
.039	.103
.0394	.23
.0384	.30
.0345	.39
.033	.49
.031	.506
.032	.527
.0226	.673
.024	.693
.0226	.723
.0186	.793
.0156	.84
.0078	1.003
.0034	1.17
.0020	1.33

c*****

T Thesis

C C1923 Camelio

c.1 Variation of wall shear
stress and Reynolds
stress over a flat plate
downstream of a boundary
layer manipulator.

Thesis

C1923 Camelio

c.1 Variation of wall shear
stress and Reynolds
stress over a flat plate
downstream of a boundary
layer manipulator.



thesC1923

Variation of wall shear stress and Reyno



3 2768 000 89151 9

DUDLEY KNOX LIBRARY